Technische Universiteit Delft

Characterization of a high pressure alkaline electrolyser

Product gas purity

B. Mulder

TU Delft

Characterization of a high pressure alkaline electrolyser

Product gas purity

by

B. Mulder

to obtain the degree of Master of Science
at the Delft University of Technology,
to be defended publicly on Friday July 9, 2021 at 3:00 PM.

"You may call me Moses, 'cause I like to split water."
Bart Mulder

Student number:	4174917	
Project duration:	May 27, 2020 – July 9, 2021	
Thesis committee:	Prof. dr. ir. W. De Jong,	TU Delft, supervisor
	Ir. J. Van Kranendonk,	Zero Emission Fuels, daily supervisor
	Prof. dr. ir. E.L.V. Goetheer,	TU Delft
	Dr. ir. J.W. Haverkort,	TU Delft

This thesis is confidential and cannot be made public until July 9, 2023.

TU Delft

Abstract

Zero Emission Fuels B.V. (ZEF) is developing a microplant, which ultimately provides a pathway to produce a hydrocarbon in a sustainable manner. This microplant consists of several subsystems. One of which is an alkaline water electrolyser, in which water is split into oxygen and hydrogen under specific operating conditions. As a mixture of the product gasses can be highly explosive, gas crossover in alkaline water electrolysis (AEC) systems is a point of concern in terms of safety. This explorative study aims to identify the main routes for crossover in AEC systems, as well as characterizing the ZEF AEC system. This characterization has been accomplished by studying the effect of process conditions and system geometry on gas crossover.

Based on a literature study, gas crossover is found to be the result of diffusion as well as convection. Both of these phenomena occur at the interconnects between the sides of the system, which is over the diaphragms and over the pressure equalization tube (PET) in case of the ZEF AEC system.

Gas measurements where conducted during over 194 hours of experiments. From this it was concluded that hydrogen crossover is the main point of concern in terms of safety. Operating pressure and temperature both very clearly affect hydrogen crossover. The effect of current density is also significant but obscured by the fact that temperature is an uncontrollable variable in the ZEF AEC system. From the steady-state data a window for safe operations has been framed.
Upon start-up of the system a spike in oxygen side H_2 concentration is consistently measured, which is a result of crossover by diffusion during system off-time. This spike in concentration also poses a threat in terms of safety.
Three different pressure equalization tubes have been tested to investigate the influence of interconnect geometry on gas crossover.

In order to identify the main route for hydrogen crossover a CSTR model of the oxygen side gas phase was developed, in which temperature and pressure effects were taken into account. The model showed that hydrogen crossover by diffusion could be held accountable for ~8% of the total amount of crossed-over hydrogen, which is in line with reports in literature for a mixed electrolyte cycle AEC system. The model also showed that crossover by solely diffusion through the PET is negligible compared to through the diaphragm.

From this, it was concluded that the ZEF AEC system behaves more like a system with mixed electrolyte cycles with respect to gas crossover levels. Recommendations are made in order to reduce hydrogen crossover, and enlarge the window for safe operation as a result.

B.Mulder
Delft, July 2021

Acknowledgements

The work presented in this thesis is the result of a lengthy academic career, a road which a lot of times hasn't been easy, but one of steady development and learning. This wouldn't have been possible without the help and support from some amazing people, from different corners of my life.

Firstly I would like to thank the ZEF company leaders **Jan van Kranendonk, Ulrich Starke, Hessel Jongebreur and Mrigank Sinha**. I owe the opportunity to do a thesis on such an interesting and relevant subject to you guys, and your positivity and enthusiasm during the project was greatly appreciated. I'd like to thank you for your trust in my abilities, as well as for always lending me your coffeecards, which proved paramount to this research. In all seriousness, thank you very much for giving me the opportunity to do my thesis at such an exciting company.
I'd also like to thank my team AEC teammates, and in particular **Kamal Ghotia, Tom Kleist and Bart Boons**. You were my mates during the though and during the high times, and you were always prepared to spar with me and work extra hard when there were hurdles to overcome.

I would also like to express my gratitude to my mentors within ZEF and within the TU Delft; **ir. Jan van Kranendonk and prof.dr.ir Wiebren de Jong**. Your guidance kept me out of most rabbit holes, and your insights always sparked interesting discussions and a clear direction for me to push the research towards. Your enthusiasm, ingenuity and wit were most inspirational, from which I've learned a great deal.

I would like to thank all of **my friends** for always hearing me out on my academic projects and hurdles, as well as providing positive distractions for me to relax and re-energise. You've been a source of encouragement as well as enjoyment for my entire academic career, and will continue to be for many years to come.

I'd like to thank my brother and sister **Stijn and Betsy Mulder**, for your love and continuous support. You provided a listening ear whenever I had been puzzling with a subject, and you are always enthusiastic about whatever it is we are talking about. I love you very much.

I would especially like to thank my twin brother, **Gijs Mulder**. We started this journey together and we finish it together. We struggled together and we have won together, and I wouldn't have done it with anyone but you. Having you by my side made this so much easier and a million times more enjoyable. We were always in the same boat, and we always kept our heads together. I wouldn't be where I am today without you. Thank you bro, I love you very much.

Last but definitely not least, I'd like to express my biggest gratitude to my parents, **Luc and Nelleke Mulder**. I dedicate this achievement to you, because without your love, amazing support and patience this would never have been possible. You always believe in us, which is the main reason why we are where we are today. Your patience meant you never ever made our academic carreer more stressful than it already was, for which I am also immensely grateful. Thank you, thank you, thank you and thank you again, I love you very very much.

Nomenclature

Abbreviations

AEC	Alkaline Electrolysis Cell
AEM	Anion Exchange Membrane
$CSTR$	Contineously Stirred Tank Reactor
DAC	Direct Air Capture
EU	European Union
FM	Fluid Machinery
HER	Hydrogen Evolution Reaction
KOH	Potassium Hydroxide
LEL	Lower Explosion Limit
MHD	Magneto-hydrodynamic
MSR	Methanol Synthesis Reactor
OER	Oxygen Evolution Reaction
PEM	Polomer Electrolye Membrane
PET	Pressure Equalization Tube
ppm	Parts per million
$PPSU$	polyphenylene Sulfone
PSD	Power Spectral Density
PSU	Polysulfone
PV	Photovoltaic
PVC	Polyvinyl Chloride
$Ra-Ni$	Raney Nickel
TU	Technical University
UEL	Upper Explosion Limit
vol	Volume
ZEF	Zero Emission Fuels

Subscripts

(aq)	aqueous state
(g)	gaseous state
(l)	liquid state

bub	bubble	
cs	concentration	
eff	effective	
$elec$	electrolyte	
rev	reversible	

Greek Symbols

α	Electron transfer coefficient	
Δ	Difference/Change in	
δ_{sep}	Separator thickness	nm
ϵ	Void fraction	
$\mathrm{E}_{H_2}^{Darcy}$	Hydrogen permeability	$mole/s^2/bar/cm^2$
η	Overpotential	V
η^{eff}	Efficiency	$\%$
κ	Specific conductance	S/cm
μ	Viscosity	$Pa \cdot s$
Φ	Volumetric flux	$ml/s/cm^2$
ϕ	Porosity factor	
Φ_x^{drag}	Electro-osmotic crossover flux of species x	$mol/cm^2/s$
Φ_x^{diff}	Rate of diffusion/diffusion flux of species x	$mol/cm^2/s$
ρ	Density	kg/m^3
σ	Electrical conductivity	S/m
τ	Tortuosity factor	
θ	Coverage ratio	

Roman Symbols

Δc_x	Concentration gradient of species x over diaphragm	mol/cm^3
ΔG	Standard Gibbs free energy of formation	J
ΔH	Standard enthalpy of formation/reaction	J
ΔP	Absolute pressure difference	bar
ΔS	Change in entropy	J/K
$\dot{V}_{H_2}$	Hydrogen volume production rate at unit volume electrolysis cell	m^3/s
A	Area	m^2
B	Magnetic field strength	T
b	Tafel slope	mV/dec
c_x	Concentration of dissolved species x in liquid electrolyte	mol/cm^3

C_*	Concentration of dissolved gas at electrode surface	mol/cm^3
C_0	Saturated concentration of dissolved gas at standard conditions	mol/cm^3
c_{elec}	Concentration of electrolyte within diaphragm	mol/cm^3
$C_{Setchenov}$	Setchenov constant	
$D_{eff,x}$	Effective diffusion coefficient of species x in diaphragm	cm^2/s
D_x	Normal diffusion coefficient of species x	cm^2/s
E	Energy	J
E_a	Activation energy	J
F	Faraday constant; approx 96485	C/mol
f	Frequency factor/frequency of collisions	
F^{an}	Feed anode gas phase volume flow	m^3/s
I	Current	A
i	Current density	mA/cm^2
i_0	Exchange current density	mA/cm^2
k	kinetic rate constant	s^{-1}
k^0	standard rate constant	s^{-1}
K_x^{diff}	diffusional permeability coefficient	
K^{perm}	permeability	cm^2
k_B	Boltzmann constant; approximately $1.380649 \cdot 10^{-23}$	J/K
M	Molarity	mol/L
M_w	Molecular weight	g/mol
n	Stoichiometric amount of moles of electrons required for electrolysis	
n_{drag}	Electro-osmotic drag coefficient	
p_x	Partial pressure of species x in the gas phase	Pa
R	Electrical resistance	Ω
r	Radius of spherical particle	m
R^{gas}	Gas constant, approximately 8.314	$J/K/mol$
R_ϵ	Overall electrolyte resistance when there are bubbles in the solution	Ω
R_e	Pure electrolyte resistance	Ω
S^{sup}	Supersaturation	
$S_{x,0}$	Solubility of gas species x in pure water	mg/L
$S_{x,s}$	Solubility of gas species x in electrolyte solution	mg/L
T	Temperature	K
t	time	s

t_{H_2}	time to produce 1 gram of hydrogen	s
U	Voltage/Potential	V
$U_{applied}$	Applied stack/cell voltage	V
U_{rev}	Open circuit voltage/equilibrium voltage/reversible cell voltage	V
U_{th}	Thermoneutral cell voltage/enthalpy voltage	V
V_{gas}^{an}	Volume anodic gas phase	m^3

Superscripts

0	in standard conditions
an	anode side
cat	cathode side

List of Figures

List of Tables

Contents

1 Introduction

1.1. Energy transition

Due to an increase in awareness of global warming the energy transition is in full motion [21][54]. This energy transition can generally be encapsulated by three elements regarding the energy sector, which influence the demand and supply of energy[43]:

- defossilization
- decentralization
- digitization

In a world where energy demand is on the rise, new regulations and goals regarding emissions call for changes in the supply of energy [54]. In 2019 the EU power sector saw a fall in CO_2 emissions of 120 Mt. This is a drop of 12% compared to 2018, and quite possibly the greatest drop there will ever be [54]. This is partly because hard coal power generation has dropped by 32% due to higher CO_2 prices, and partly because the amount of energy produced by renewables rose to a record of 35% of EU energy production. For the first time ever, wind and solar combined produced more power than coal. And this is a trend that will only keep on going, as the EU is striving to be the first greenhouse gas neutral continent by 2050.

This rise in renewable energy production and drop in CO_2 emissions is not a coincidence: renewable energy production has the potential to address all three of the elements mentioned before. But implementing renewable energy to power the grid comes with some difficulties. Most renewable energy sources are very dynamic in nature: wind turbines only produce power when there is wind, PV cells only produce power when there is significant amounts of sunlight etc. This presents a challenge, as a grid which purely relies on renewables would come with some risk [57]. So in order to be able to overcome these difficulties and have a stable and reliable grid, being able to store renewable energy is essential.

A technology which allows us to do just that is power-to-chemical conversion. Now although the discovery of power-to-chemicals dates back to the early nineteenth century, and commercial fuel cells becoming available as early as 1932, it has never been more relevant than it is today. Power-to-chemical technology could provide a solution in the pursuit of a sustainable world. It would allow us to enlarge renewable energy production even further, until far beyond the specific electricity need at a specific hour, storing the surplus energy in the form of a chemical. This chemical could then be used to either convert it back to electricity at times when the renewable sources are not sufficient, or used as a feed stock for the chemical industry, replacing harmful fossil fuels. Converting the energy into a chemical also opens up the possibility for the energy to be transferred from areas which are rich in renewable energy sources due to their geographical location, to more populated areas where energy demand is high, addressing decentralization of energy supply market.

1.2. ZEF

ZEF, short for Zero Emission Fuels, is a start-up company, founded by tech-entrepreneurs Jan van Kranendonk, Ulrich Starke and Hessel Jongebreur. Since 2017 they have been operating out of the TU Delft laboratory, and have access to the latest in energy technologies. They are working diligently towards becoming a big player in the power-to-chemical industry. After a thorough market analysis, and evaluating different options, the decision was made to develop a sustainable methanol production process. One of the advantages of producing methanol is that it is in liquid state at ambient conditions, which means transport becomes much less complicated compared to for instance hydrogen, another popular power-to-chemical product. And as methanol is widely used as feed-stock in the chemical industry, there is a well established market for the hydrocarbon [5].

ZEF operates following several core competencies:

- ZEF is characterized by a very flat organization, meaning there is virtually no gap between company leaders and development teams. This creates an environment where executive decisions can be made very quick, and can therefor immediately be implemented in the design process.

- ZEF has support from various industry (TNO, YESDelft!, Climate KIC) and academic experts (TU Delft, University of Twente), which forms a very broad support structure. This support also means there is access to physical resources, such as state-of-the-art laboratories and facilities.

- ZEF works with teams made of interns and thesis students, which cycle every 3 to 9 months respectively. Every team gets a sprint planning with individual goals to achieve, which means that the development cycles are very fast, picking up where the previous team has left. This means that every team gets to build prototypes, test hypotheses, achieve results and gain knowledge very quickly. This allows ZEF to adjust the course of their development very easily and as often as is required.

- ZEF has subdivided the entire system in subsystems, each with their own difficulties and challenges. Every team is split-up into smaller teams, which work on their assigned subsystem. These smaller teams are multidisciplinary, and are specifically put together so that they can learn from each other, and work as efficiently as possible to reach their sprint goals. Having to work on just a small part of the entire system means that it is easier for student to become familiar with the state-of-the-art of the specific technology.

1.3. ZEF microplant

ZEF is developing a microplant which will produce methanol by capturing water and carbon dioxide from the surrounding air, with power generated solely by PV cells. A schematic of the microplant can be observed in figure 1.1. The PV cells allow the microplant to be able to operate completely of the grid. This means it can be implemented in remote areas which are favorable for their respective ambient conditions. The microplant is modular and small scale, as a small size system is more suitable for dynamic operations, which is essential when using fluctuating energy sources like solar energy. Small scale means fast heating and cooling, and thus fast start-up and shutdown. A render of the microplant can be observed in figure 1.2a. Scale-up is achieved in numbers, rather than in creating a larger system. This way methanol farms consisting of multiple tens of thousands microplants can produce methanol in a sustainable way, completely automated and off the grid, storing the liquid methanol on site. Figure 1.2 gives an image as to what that would look like.

1.3.1. Subsystems

The ZEF methanol microplant can be divided into 6 subsystems, which can be observed in figure 1.1.

Solar Panels

This is the subsystem where all power required to operate the microplant is produced. There are three panels per microplant, each producing approximately 300 W of power by converting solar irradiation into electrical energy.

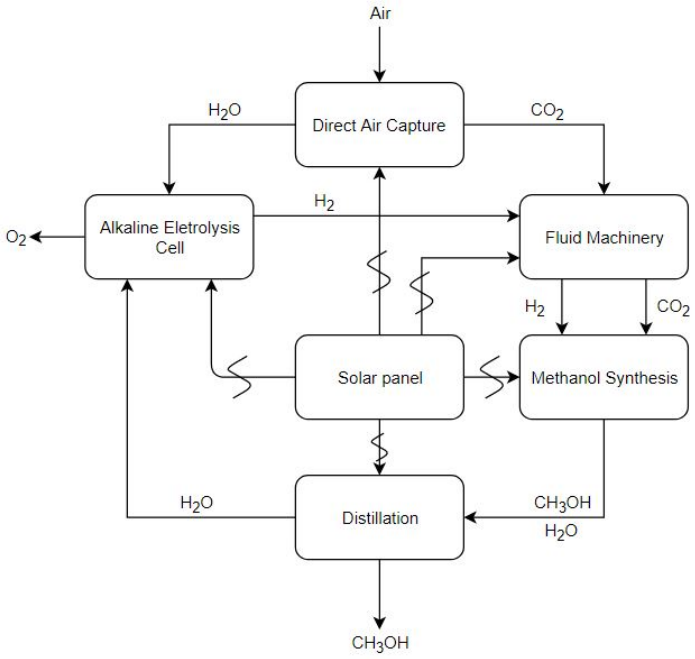

Figure 1.1: Schematic of ZEF methanol microplant

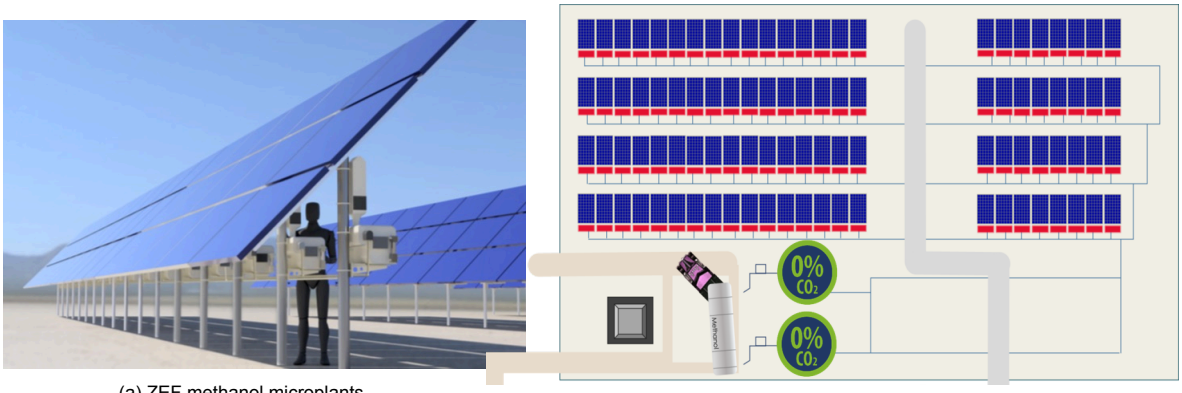

(a) ZEF methanol microplants

(b) Possible layout

Figure 1.2: Methanol microplant farm illustrations

Direct Air Capture - DAC
In the DAC subsystem water and carbon dioxide are captured from the air via an adsorption process. The adsorbed feed stock substances are separated via distillation, and send on to the subsequent subsystem.

Alkaline Electrolysis Cell - AEC
The captured water that comes from the DAC is split into oxygen and hydrogen in the AEC subsystem. The oxygen will ultimately be purged to the environment, as this is of no immediate use. Meanwhile the hydrogen is send to the next subsystem. The specifics of this subsystem will be described in great detail in chapter 2.

Fluid Machinery - FM
The captured carbon dioxide and produced hydrogen are being compressed to a pressure of 50 bar in the FM subsystem. This is the optimum pressure level for the Methanol Synthesis Reactor. Other components making up the FM subsystem are several pumps and valves, which are required for the system to operate.

Methanol Synthesis Reactor - MSR
In the MSR, methanol is produced by bringing together the produced hydrogen and captured carbon dioxide through a copper catalyst bed under specific conditions. The MSR is natural convection driven, and it's working principle of the reactor is based on the work of Brilman et al. [9]. It has been shown that such a reactor could theoretically run autothermal[8][71]. This means the heat that is being released in the synthesis reaction is sufficient to heat up the hydrogen carbon dioxide gas mixture before it enters the reaction area. Besides methanol, water is also formed in the MSR under the mole ratio of 1:1. It is important to note that in-going hydrogen gas has to be of 99.9% purity in order to minimize build up of unwanted species inside the system.

Distillation
After the MSR, the produced methanol and water mixture will be separated through distillation in the final subsystem, to achieve 99.8% pure methanol.

1.4. ZEF AEC subsystem: product gas purity

As a mixture of product gasses of the AEC subsystem, oxygen and hydrogen, can be highly explosive, knowledge on gas crossover and gas purity is paramount in terms of safety. The current ZEF AEC system makes use of a connected electrolyte cycling scheme in order to equalize the pressure of anodic and cathodic half cells. The disadvantage of a connected electrolyte cycling scheme according to literature is that it is accompanied with high amounts of gas crossover due to mixing of electrolyte from both sides of the system [70]. However, ZEF CEO Jan van Kranendonk hypothesizes that crossover in the pressure equalization tube only happens due to diffusion and not through convection, should the tube be of sufficient length. He states that only an oscillating flow is present in the tube when the pressure is equalized. He reckons that the level of crossover in the ZEF AEC system is therefor closer to that of an electrolyser system with separated electrolyte cycling schemes than to a totally mixed electrolyte cycling scheme system. The hypothesis is therefor the following:

- If the ZEF electrolyte cycling scheme with pressure equalization tube works as expected, then steady state experiments at an operating pressure of 20 bar will show that for a current density of $150\ mA/cm^2$ the oxygen side H_2 remains below $1.75\ vol\%$ [70].

1.5. Research questions

The primary objective of this thesis is:

Characterization of a high pressure alkaline electrolyser with respect to product gas purity.

In order to achieve this objective, the following research questions ought to be addressed:

- Which process parameters and design choices influence product gas crossover, and thus product gas purity?
- What is the effect of these parameters on gas purity during several particular modes of operation: start-up, standby and steady-state operation?
- What is the performance of the current ZEF electrolyte cycling scheme (with pressure equalization tube)?
- What is the safe window of operation during steady state in terms of crossover for the ZEF AEC system?

With the knowledge obtained from the research questions listed above, the final objective of this thesis is to make recommendations on how to improve hydrogen product gas purity of the ZEF high pressure alkaline electrolyser system.

1.6. Scope of this research

The challenge in this research is firstly to perform high pressure electrolysis reliably, with an alkaline electrolyser based on a design by ZEF, and secondly to implement gas purity sensing systems on both

the hydrogen and oxygen side of the electrolyser inside the confined space of the bunker set-up, to do reliable, close to real-time product gas analysis.

The scope of this research will be in the realms of the following.

- The main focus will be on gas crossover, and all parameters affecting this process.
- Gas analysis will therefor strictly be focused on anodic hydrogen content and cathodic oxygen content, as these are the primary species of gas present inside the system.
- One of the end products of this research is quantification of the effect of current density, operating temperature and operating pressure on gas crossover. With that being delivered, characterization of the electrolyser system will be regarded as being accomplished.

2

Theoretical background: Alkaline Electrolysis Cell

This chapter will provide an overview of the theory behind water electrolysis. This is done by first looking at what is actually happening inside the cell. After that, an overview of the state of the art regarding reaction thermodynamics, kinetics and product gas crossover will be given. And to finalize the chapter, work of previous ZEF teams will be evaluated.

2.1. Principles of water electrolysis

Water electrolysis is the principle of splitting water molecules (H_2O) into the chemical elements of which it consists, which are oxygen (O_2) and hydrogen (H_2). This is achieved by supplying an amount of energy in the form of electricity. If above a certain level, this energy makes it possible for the stable bonds between the atoms in the water molecule to break. This all takes place inside a cell, a schematic of which can be observed in figure 2.1. A single cell consists of two electrodes placed inside an ion conducting alkaline electrolyte, separated by an ion conducting diaphragm. A more detailed description of the individual components will follow.
Electrolyser systems often consist of multiple cells. These multiple cells together are referred to as the stack. Alkaline water electrolysis is currently the industry standard when it comes to water electrolysis, due to low investment cost and long lifetime [28].

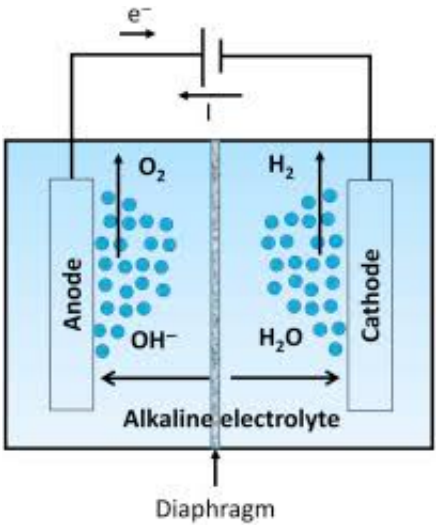

Figure 2.1: Schematic of an alkaline electrolysis cell (AEC). Adapted from Coutanceau et al. [12]

2.1.1. Components

Now that the basic cell layout of an alkaline water electrolysis system is clear, the individual components of the cell will shortly pass by. A more in depth explanation on how properties of the individual components affect reaction kinetics will follow in section 2.3.

Electrodes

As mentioned before, energy is required to perform electrolysis. It is through the electrodes that this energy is supplied, in the form of a potential difference. At the cathode an electron is supplied to the water molecules in the electrolyte solution, while at the anode an electron is taken from the hydroxide ions, also in the electrolyte solution. This transfer of electrons is what results in the reactions, which take place right at the surface of the electrodes. The electrode material properties and morphology therefor greatly influence the reaction kinetics [11]. An extensive explanation on the subject will follow in section 2.3.1.

Electrode materials should have high catalytic activity for both the hydrogen evolution reaction (HER) and the oxygen evolution reaction (OER), be very electrically conductive, and be corrosion resistant to increase lifetime. It is possible to have different materials for the anode and cathode. Alkaline water electrolysis evades the need for precious metals such as platinum for the electrodes, like is the case in polymer electrolyte water electrolysis (PEM). Many materials like iron, cobalt and chromium have been investigated for their electrocatalytic properties, but pure nickel has proven to be stable as an electrocatalyst for both HER and OER in alkaline electrolyte [11][59]. Nickel is the most active non-noble pure metal [51]. Dealloynized nickel alloys from alloys like nickel-zinc, nickel-aluminium, or nickel-silicon, known as Raney nickel (Ra-Ni), show a substantial performance increase over untreated pure Nickel as an effective electrocatalyst for the cathodic HER [49]. Raney nickel owes its increase in performance to its morphology and surface structure, as it is highly porous with a large internal surface area [42]. It is made by leaching out the zinc, aluminum or silicon from the alloys, for only the very active nickel to remain, containing also hydrogen in an adsorbed state, or as nickel hydride. This hydrogen must then be oxidized in order to obtain the activated Raney nickel material [11].

Diaphragm

The diaphragm is a micro porous material with an average pore size of less than 1 μm, used to separate the two compartments of each cell. The diaphragm enables OH^- ions to reach the anode side, while reducing intermixing of the product gasses inside an alkaline electrolysis system. This limiting of gas crossover enables relatively high purity product gas outlet compositions, as well as keeping the formed gasses from possibly reacting with each other and going back to their original state, forming water again. Aqueous electrolyte solution is able to penetrate the micro pores of the diaphragm, making the diaphragm ion conducting. This ionic conductivity is therefor a result of hydrophilic properties of the diaphragm material and structure, and must be maximized in order to minimize ohmic losses. The diaphragm must be non-conductive to electrons, as this would cause an electrical short circuit. The non-conductive nature of the diaphragm also allows the electrodes to be installed at close distance, minimizing hydroxide ion path length and reducing mass transport resistance.

Up until the change of the millennium, diaphragms used in conventional water electrolysers where made from asbestos [74]. The substance was already known to be carcinogenic, making it's future uncertain at the time. Another major drawback of the asbestos diaphragms is the lack of thermal stability, as they corrode in alkaline media at temperatures above $100°C$ [72]. This limited the operating temperature of the cell to $90°C$, hindering high efficiencies achievable at elevated temperatures. This all meant new diaphragm materials had to be examined. Asbestos has since been banned for use in multiple countries, and new diaphragm materials have found their way into water electrolyser systems.

These new diaphragm materials mainly consist of polymers, which have been treated to improve wettability. Zirfon is exactly that, and it has since become the contemporary industry standard. Zirfon is made by impregnating a mixture of a polymer and zirconium oxide (ZrO_2) into an open mesh polysulfone fabric. The particular polysulfone material used in Zirfon is polyphenylene sulfone (PPSU), which gives the diaphragm mechanical strength. The ZrO_2 acts as an hydrophilic filler which enhances the wettability of the polymer matrix structure, resulting in low ion migration resistance [36][72]. Zirfon has a relatively large poresize of $130\ nm$, aiding reduction in ionic resistance. Apart from the major benefit of Zirfon not being carcinogenic, experiments by Teledyne Brown Engineering showed it

also improved on two other relevant diaphragm characteristics compared to asbestos: its resistance to permeate gaseous hydrogen and its electrical resistance [74]. Zirfon is considered impermeable to gaseous hydrogen up to a pressure difference of 5.5 bar [74]. The electrical resistance is about 5% higher compared to asbestos [74]. Zirfon diaphragms also offer high chemical and thermal stability, with an average weight loss of 2% after 10.000 hours of operation in $30\ wt\%$ KOH solution at $120°C$, as measured by Vermeiren et al. [72]. Apart from Zirfon, other enhanced polymers have also been developed. The Moscow Power Engineering Institute has opted to use titanium dioxide (TiO_2), a less expensive and more available filler than ZrO_2 [36].

Another well tested separator technology is an anion exchange polymer membrane (AEM) [34]. The difference between anion exchange membranes and diaphragm materials like Zirfon is that instead of relying on micro pores permeable to aqueous electrolyte solution for its ion conductivity, the AEM inherits its ion conducting capabilities by the presence of cationic side groups fixed to the polymers. These cationic side groups are paired with anions (hydroxide ions), which become mobile when they are dissociated in water. As only water is required in forming these ionic channels through the membrane, this technology theoretically omits the need for aqueous electrolyte solution. It must be noted though that omitting electrolytes is accompanied with a performance drop due to conditions/properties outside the membrane in the remainder of the cell [34]. This technology has therefor not been adopted by the industry like Zirfon has, due to its inferior conductivity and stability [10][34].

One of the latest in separator technologies is an ion-solvating membrane [34]. Ion-solvating membranes also don't rely on micro pores like diaphragms do, but instead form an homogeneous ternary electrolyte system when drenched in electrolyte solution. This system consists of polymers, KOH and water, and conduct hydroxide ions solely by the uptake of the electrolyte solution. The advantage of this technology is that as the ion-solvating membrane structure is without micro pores, this separator can be much thinner compared to diaphragms. A membrane thickness of as little as $40\ \mu m$ could be implemented, compared to Zirfon diaphragm thickness of $500\ \mu m$. As a result the resistance over the membrane is lower, directly decreasing Ohmic losses. Kraglund et al. proved through experiments with an aqueous KOH solution doped poly(2,2′-(m-phenylene)-5,5′-bibenzimidazole) (m-PBI) membrane that significant performance gains could be achieved, operating at current densities comparable to PEM electrolyser systems [34]. However, the major impediment of the m-PBI membrane is the lack of chemical stability and mechanical robustness. During experiments, failure occurred due to membrane degradation, ultimately short circuiting the cell. For the $40\ \mu m$ thick m-PBI membrane this happened after approximately 130 hours of operation [34]. Doubling the membrane thickness resulted in roughly double the end-of-life time, but is of course accompanied with increased resistance over the membrane. For implementation of this technology to be feasible, new polymer materials have to be developed which are chemically stable ánd mechanically robust.

A schematic of the three mentioned separator technologies can be observed in figure 2.2. Hereinafter only the diaphragm separator technique will be discussed due to it being a developed technology and most widely used in the industry.

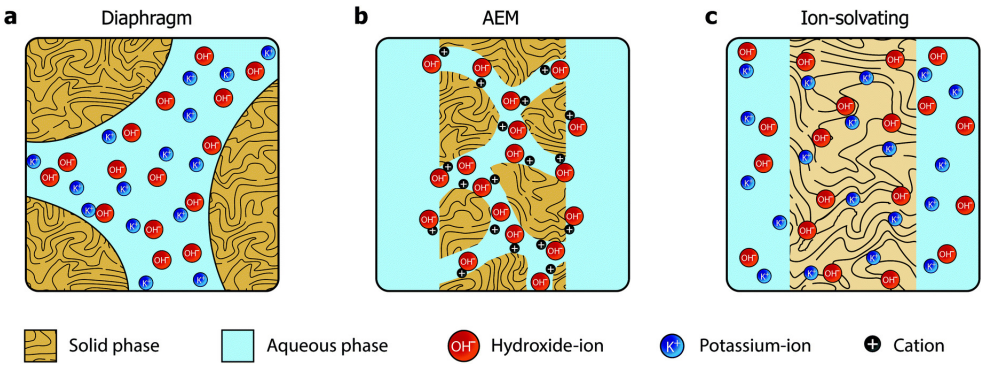

Figure 2.2: Schematic representation of different separator technologies: a; micro porous diaphragm like Zirfon, b; anion exchange membrane (AEM), c; ion-solvating membrane. Adapted from Kraglund et al. [34]

Electrolyte
In chemistry, an electrolyte is any salt or ionziable molecule that, when dissolved in a solution, will give that solution its ability to conduct electricity. This happens because the dissociated ions that are introduced when a salt is dissolved can move freely in the solution, allowing a charge to flow. In the field of electrolysers (and from here on in this report as well), electrolyte is the collective name for the alkaline liquid solution which is present inside the cells. This solution is in direct contact with the electrodes and diaphragm, and it is responsible for conduction of ions throughout the cell and through the diaphragm. Good conductance is therefor desired, as it helps ionic transfer inside the solution. Although electrolyte solutions using substances like sodium hydroxide (NaOH) and sulfuric acid (H_2SO_4) have been used, solutions using potassium hydroxide (KOH) have been widely adopted in commercial electrolysers, due to its superior ionic conductivity [77] [10] [75]. The concentration of the aqueous solution is also of great importance to its performance. It influences ionic conductance, and thus electrical resistance. Typically, concentrations of 20-30 $wt\%$ KOH is seen in the industry, as the ionic conductivity is optimal for typical operating temperatures ranging from $50°C$ to $90°C$ [77][10]. The electrolyte can also be utilized to detach product gas bubbles which form on the surface of the electrodes. This can be done by establishing a flow of electrolyte through the cell, which causes the bubbles to detach from the electrodes through forced convection.
Recent development has been focusing on adding ionic activators to the electrolyte solution [75]. The purpose of these additives is to enhance catalytic performance of both the electrolyte and electrodes. It does so by electrodepositing catalytic metal composites in situ on electrode surfaces, creating a larger surface area of catalytic material. Additives aimed at accelerating bubble detachment from electrodes by altering the wettability are also a point of interest [75].
Another field of research is focusing on replacing reagents like KOH and NaOH by electrically conductive organic compounds; ionic liquids [10]. As alkali conductive salts are very corrosive to the electrodes, the major advantage of ionic liquids is that they are chemically inert to metal electrodes, improving catalytic lifetime [75][10]. The drawbacks however are higher viscosities resulting in increased mass transport resistance, and lower current densities meaning lower feasible hydrogen production rates.

2.1.2. The reactions
When evaluating the alkaline electrolysis cell as a whole, the overall reaction scheme is the following:

$$2H_2O_{(l)} + \Delta E \rightarrow 2H_{2(g)} + O_{2(g)} \tag{2.1}$$

To achieve this overall reaction, multiple half reactions are taking place simultaneously at both electrode surfaces.

At the negatively charged cathode, water is first being split into hydrogen and hydroxide ions via a multi step process, which will be addressed in section 2.3.1. These cathodic steps together are referred to as the hydrogen evolution reaction (HER), and take place right on the surface of the cathode when water molecules receive an electron presented to them by the electrode. This multi step process is summarized by the following reaction scheme:

$$4H_2O_{(l)} + 4e^- \rightarrow 2H_{2(g)} + 4OH^-_{(aq)} \tag{2.2}$$

The hydroxide ions are able to reach the other side of the cell by conduction through electrolyte and diaphragm, where they get in contact with the positively charged anode. It is here that the hydroxide ions give away their extra electron, and form oxygen and water, also in a multi step process. The oxygen evolution reaction (OER) can be summarized by the following:

$$4OH^-_{(aq)} \rightarrow O_{2(g)} + 2H_2O_{(l)} + 4e^- \tag{2.3}$$

Reactions 2.2 and 2.3 together make up reaction 2.1.

2.1.3. Energy required
In order to be able to break the stable bonds which hold together the water molecules, an amount of energy is required. To quantify the energy required, the second law of thermodynamics is utilized:

$$\Delta H = \Delta G + T\Delta S \tag{2.4}$$

ΔH is the enthalpy of reaction, while ΔG is the standard Gibbs free energy of formation, in this case of water. ΔG can be seen as the minimum amount of electrical energy required to dissociate a mole of water. The minimum required voltage at which electrolysis could theoretically take place is referred to as the open circuit voltage, equilibrium voltage or reversible cell voltage U_{rev} [53], which is calculated for standard conditions, using equation 2.5 [78].

$$U_{rev} = \frac{\Delta G^0}{nF} = \frac{237.1\ kJ}{2 \cdot 96485\ C/mol} = 1.23\ V \tag{2.5}$$

n Is the stoichiometric amount of moles of electrons which are required for electrolysis, which for water has a value of 2. F is the Faraday constant, which represents the charge of a mole of electrons. U_{rev} can be seen as the amount of potential difference over both electrodes which theoretically allows for water to split into hydrogen and oxygen. It must be noted that U_{rev} is temperature and pressure dependent, and the value given in equation 2.5 is for 1 bar at 25°C. For 1 bar at 100°C, U_{rev} drops to a value of 1.17 V [28]. Raising the pressure will however raise U_{rev}: at 50 bar and $25°C$ and $75°C$ values for U_{rev} are 1.312 V and 1.283 V respectively [55].

When looking at equation 2.1, it can be observed that from 2 moles of liquid water 3 moles of gas are produced. This means there is an increase in entropy, which indicates that heat is consumed by the reaction: the overall reaction is endothermic. An additional amount of thermal energy therefor has to be supplied in order for the temperature to remain constant. This additional amount of energy can come from two sources: an external heat source, or through heat dissipated inside the cell produced with an extra amount of voltage. In adiabatic, standard conditions, the enthalpy of reaction ΔH^0 amounts to 285.8 kJ/mol [28], which means the amount of energy required to overcome the change in entropy is 48.7 kJ/mol. This it the required thermal energy, and it is the $T\Delta S$ part of equation 2.4. And because this is under adiabatic conditions, ΔH^0 is in this case purely attained by supplying electricity (so without external heat source). The potential that achieves this is called the thermoneutral cell voltage (or enthalpy voltage) U_{th}, which can be calculated using equation 2.6 [53][39].

$$U_{th} = \frac{\Delta H^0}{nF} = \frac{285.8\ kJ}{2 \cdot 96485\ C/mol} = 1.48\ V \tag{2.6}$$

This suggests that 3 thermal modes of operation could be identified [77]:

- Endothermal mode: $U_{rev} \leq U_{applied} < U_{th}$
  When the applied voltage is above or equal to the equilibrium voltage but below thermoneutral voltage, external heating must be applied for the temperature to remain constant.
- Autothermal mode: $U_{applied} = U_{th}$
  When the applied voltage is equal to the thermoneutral voltage, the heat that is being generated and dissipated inside the cell due to an extra overpotential is sufficient for the cell temperature to remain constant. In this case the internal heat dissipation exactly matches the required energy input.
- Exothermal mode: $U_{applied} > U_{th}$
  When the applied voltage is above the thermoneutral voltage, external cooling should be applied for the temperature to remain constant.

These three modes are graphically represented in figure 2.3, where U_{rev} and U_{th} are plotted against temperature [77]. What can be observed is that although the equilibrium voltage decreases significantly with increasing temperature, the thermoneutral voltage is much less dependent on temperature as it only increases marginally with increasing temperature.
Increasing the pressure also has an effect, as the proportion of electrical energy ΔG versus thermal energy $T\Delta S$, which together add up to form the enthalpy of reaction ΔH, shifts at elevated pressure [55]. Pressure has a negligible effect on ΔH for operating temperatures below $100°C$, but as mentioned before increasing the pressure increases the electrical energy required for reaction ΔG, while it decreases the thermal energy required to maintain a constant temperature $T\Delta S$. Intuitively this holds up, as at higher pressure it requires less thermal energy to maintain constant temperature in an endothermic reaction process.

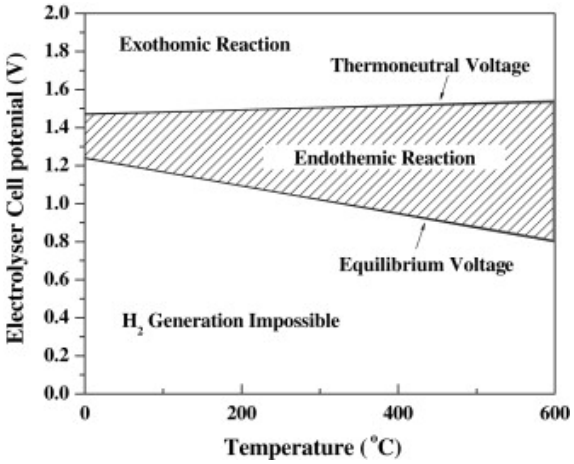

Figure 2.3: Graphical representation of thermal modes for AEC systems, at atmospheric pressure. Adapted from Zeng et al. [77]

The surplus in potential above the equilibrium voltage is often referred to as overpotential [75]. This overpotential originates from multiple sources, and is generally divided into three groups: activation -, reaction - and concentration overpotential. Overpotential is dependent on both temperature and pressure, as it will decrease with increasing temperature, as well as with increasing pressure [3][55]. It is possible to evaluate the relationship of overpotential η and current density i using the empirical Tafel equation, which will be addressed later in the chapter, as well as identifying where its temperature and pressure dependence originates from.

2.1.4. Efficiency

Energy efficiency is very often defined as the energy output divided by the energy input. Yet, in electrolysis there are multiple ways of expressing the efficiency, depending on how the system is assessed and compared [77][55].

When efficiency is analyzed looking at the potential difference over the electrodes versus the actual applied voltage, the electrolysis cell voltage efficiency is acquired, and it is defined according to equation 2.7.

$$\eta_{voltage}^{eff} = \frac{U_{anode} - U_{cathode}}{U_{applied}} \cdot 100\% \tag{2.7}$$

$\eta_{voltage}^{eff}$ represents the percentage of effective voltage to split water in the total applied voltage over the whole electrolysis system, and provides a good approximation of the efficiency of the electrolysis cell [77]. This does however require a third electrode, known as the reference electrode, to enable measurement of the anode and cathode individual potentials. As there is no reference electrode in the ZEF AEC system, it won't be possible to calculate $\eta_{voltage}^{eff}$.

It is however possible to calculate two other efficiencies, based on the energy changes of the water electrolysis system [77].
Since we have identified U_{rev} to be the minimum voltage required to overcome the Gibbs free energy change, upon which electrolysis of water first takes place. It's possible to define an efficiency based on this potential, and it goes by the name of Faradaic efficiency:

$$\eta_{Faradaic}^{eff} = \frac{\Delta G}{\Delta G + losses} \cdot 100\% = \frac{U_{rev}}{U_{applied}} \cdot 100\% \tag{2.8}$$

If now the heat required for the reaction is taken into account as well, not only the change in Gibbs free energy has to be taken into account, but the entire enthalpy change of water decomposition reaction.

This is referred to as the thermal efficiency. Equation 2.8 becomes:

$$\eta_{thermal}^{eff} = \frac{\Delta H}{\Delta G + losses} \cdot 100\% = \frac{U_{th}}{U_{applied}} \cdot 100\% \tag{2.9}$$

For standard conditions, the Faradaic and thermal efficiencies are:

$$\eta_{Faradaic}^{eff,0} = \frac{1.23\,V}{U_{applied}} \cdot 100\% \tag{2.10}$$

$$\eta_{thermal}^{eff,0} = \frac{1.48\,V}{U_{applied}} \cdot 100\% \tag{2.11}$$

The Faradaic efficiency is a measure of cell efficiency purely from the equilibrium voltage point of view, while for the thermal efficiency it is taken into account that heat is required for the reaction, which as been said can be supplied by an extra overpotential. Should the system be operational in endothermal mode, that is $U_{rev} \leq U_{applied} < U_{th}$, it can be observed from equation 2.9 that $\eta_{thermal}^{eff}$ may exceed 100%, as heat required for the reaction is supplied not via an extra overpotential, but instead absorbed from it's surroundings. When the cell operates at the thermoneutral voltage, the thermal efficiency will be 100%, as no heat will be absorbed from or released to the environment [77]. In practice the Faradaic efficiency is always lower than 100%, as there are always losses present in the system.
It can be observed that increasing the overpotential $U_{applied}$ directly decreases the cell efficiency. In practice, having an overpotential is inevitable due to activation losses, ohmic losses and mass transport losses. A more detailed explanation on why and where these losses occur will be given in section 2.2.

Another way of expressing the efficiency of the electrolysis system is to consider the hydrogen production rate against the total electrical energy applied to the system[77]. The hydrogen production rate efficiency can be calculated using equation 2.12.

$$\eta_{H_2 productionrate}^{eff} = \frac{r_{H_2 productionrate}}{\Delta E} = \frac{\dot{V}_{H_2}}{U_{applied} \cdot I_{cell} \cdot t} \cdot 100\% \tag{2.12}$$

$$\eta_{H_2 productionrate}^{eff} = \frac{E_{usable}}{\Delta E} = \frac{283.8\,kJ}{U_{applied} \cdot I_{cell} \cdot t_{H_2}} \cdot 100\% \tag{2.13}$$

The hydrogen production is evaluated according to the energy carried by the produced hydrogen (high heating value of hydrogen, which is 283.8 kJ). $\dot{V}_{H_2}$ is the hydrogen volume production rate at unit volume electrolysis cell, while i_{cell} is the cell current, t is the time in seconds, while t_{H_2} stands for the time it takes to produce 1 gram of hydrogen. Equations 2.12 and 2.13 basically give the hydrogen production rate per unit electrical energy input, which opens the opportunity to directly compare the hydrogen production capacity of different kinds of electrolysis cells [77].

A final way of expressing the energy efficiency is by subtracting all energy losses from the total energy input [77].

$$\eta_{energy}^{eff} = \frac{E_{input} - E_{losses}}{E_{input}} \cdot 100\% \tag{2.14}$$

Losses are caused by resistances inside the system. Quantification and explanation on these resistances will follow in section 2.2.

From above, it can be seen that there are broadly two ways to improve energy efficiency [77]. The first is by altering the thermodynamics of the cell to reduce the energy required for splitting water into hydrogen and oxygen. Alteration of operating temperature or pressure could for instance be done to influence reaction kinetics. The second is by reducing the internal energy losses to improve the energy efficiency of the system. This can be accomplished by minimizing the resistances inside the cell.

2.2. Resistances in the system

Just like any other system, it is possible to represent the electrolyser system with an electrical circuit. This provides a better understanding of the resistances inside the cell. This insight is of great importance, as resistances in an electrolyser system are the predominant factor in energy losses. As mentioned before, lowering these resistances will therefor directly improve the energy efficiency.

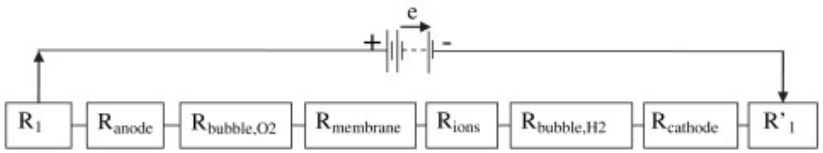

Figure 2.4: Electrical circuit analogy of alkaline electrolysis cell. Adapted from Zeng et al. [77]

Figure 2.5 provides a graphical interpretation of the resistances inside an electrolyser cell. These resistances can be seen as barriers, which have to be overcome by supplying a sufficient amount of electrical energy. It is only then that the electrochemical reaction process can occur [77].

2.2.1. Ohmic resistance

The Ohmic resistance encapsulates all resistances caused by the electric connections and pathways inside the system (known as the electrical resistances), as well as the mass transport resistances.
The electrical resistances are caused by the wiring and electrical connections to the electrodes. In the electrical circuit analogy provided in figure 2.5 they are represented by R_1 and $R_1^{'}$. The electrical resistance can be calculated by the physics equation 2.15, or by Ohm's law in equation 2.16 [46].

$$R = \frac{L}{\sigma A} \tag{2.15}$$

$$R = \frac{U}{I} \tag{2.16}$$

The mass transport resistances are caused by a variety of events occurring inside the cell such as gas bubble formation, as well as by properties of the electrolyte and diaphragm. Inside the electrolyte mass transport resistance is determined by the ion conductivity of the electrolyte, as well as by distance between electrodes. This resistance is represented by R_{ions} in figure 2.5, and it is decreased by either adding conductive salts like KOH or NaOH [75], or by placing electrodes closer together. Adding more alkaline salts does however come with its drawbacks, as they are very corrosive. It therefor has an effect on what materials can be used, and consequently on lifetime of electrodes, diaphragm and cell itself.
The diaphragm/membrane is another physical resistance providing barrier inside the system. The resistance due to the membrane ion conduction is noted as $R_{membrane}$ in figure 2.5 [75].

The bubble effect

As mentioned above, bubbles play a significant role in the ohmic resistance inside an electrolyser cell [27]. They provide a physical resistance due to coverage of the electrodes ánd due to dispersion of bubbles in electrolyte. These two phenomena together are know as the bubble effect, and are regarded as the preeminent cause of high energy consumption in water electrolysis [75]. The bubble layer next to the electrodes can consequently be divided into two layers: the layer with bubbles covering the electrode and the layer with bubbles rising in electrolyte [75].
In the first layer, part of the electrode is being blocked from the electrolyte, prohibiting this area to perform the HER and OER reactions. These resistances are represented by $R_{bubble,O2}$ and $R_{bubble,H2}$ in figure 2.5.
In the second layer, the gas bubble fraction inside the electrolyte, known as void fraction, has a substantial effect on the electrolyte conductivity. The dispersed bubbles take away some of the volume which can be used to transport hydroxide ions from cathode to anode, which means increased resistance. It is reported in literature that the resistance due to void fraction is less significant in a zero-gap cell configuration, as in such configuration distance between electrodes is minimized [48]. The effects are

however debatable, as bubbles could become trapped in cavities between diaphragm and electrode, which would result in increased resistance. More on zero-gap cell configuration in section 2.5.1
Different techniques could be implemented to reduce the resistances caused by the bubble effect. Forced bubble detachment is an active field of research at the moment, as there is much to be gained in this area. The implementation of external fields like an high gravity field, magnetic field (magneto-hydrodynamic convection), ultrasound field and/or a velocity field could possibly lower resistance due to bubble effect, and with that increase cell performance [70]. The effects of implementing an external magnetic field have been examined by multiple researchers [75][45][44]. The Lorenz force induced by the applied magnetic field results in magneto-hydrodynamic (MHD) convection, which is able to force bubbles off the electrodes. The benefits of this are substantial, as it results in a decrease in resistance caused by the first bubble layer and a decrease in overpotentials. Apart from improving bubble detachment, MHD convection lowers the void fraction as well due to its additional pumping effect, further reducing the resistance due to bubbles in the second layer in the bulk of the electrolyte, decreasing ohmic losses of the system even more [75][44]. An example of a velocity field would be forced electrolyte flow inside the system, which might be able to force gas bubbles to move due to convection, clearing electrode surface area [77]. It must be noted that increased electrolyte circulation, whether it's due to forced electrolyte flow or MHD convection, does have an influence on product gas crossover, as will be explained in section 2.3.4 [70].

The ohmic resistance causes heat generation inside the system. This heat generation can be quantified by Joule's law [46]. Ohmic losses account for all lost energy due to ohmic resistance [77].

2.2.2. Electrochemical reaction resistances

The electrochemical reaction resistance comes from the fact that an overpotential, known as reaction overpotential, is required to overcome the activation energies in the formation of hydrogen and oxygen from water, as mentioned in 2.1.3. These barriers determine the kinetics of the electrochemical reactions, and directly cause for an increase in overall cell potential [7] [77]. The reaction resistances are greatly influenced by the activities on the surface of the electrodes, and are represented by R_{anode} and $R_{cathode}$ in figure 2.5.

2.2.3. Total resistance

The ohmic resistance and electrochemical resistance combined form the total resistance of the cell.

$$R_{total} = R_1 + R_{anode} + R_{bubble,O2} + R_{membrane} + R_{ions} + R_{bubble,H2} + R_{cathode} + R_1' \tag{2.17}$$

Since the energy losses inside the system are a direct consequence of the resistances inside the system, they can be represented in a similar manner [77].

$$E_{loss} = \sum E_{loss,i} = E_{loss,circuit} + E_{loss,anode} + E_{loss,O_2 bubble} + E_{loss,ion} + E_{loss,membrane} + E_{loss,anode} + E_{loss,H_2 bubble} \tag{2.18}$$

It is also possible to write the applied cell voltage in terms of the resistance:

$$U_{applied} = E_{anode} - E_{cathode} + i \cdot \sum R = U_{rev} + \eta_{anode} + \eta_{cathode} + i \cdot \sum R \tag{2.19}$$

E_{anode} and $E_{cathode}$ are anode potential for OER and cathode potential for HER respectively, i is the current density, $\sum R$ is the total ohmic resistance and η_{anode} and $\eta_{cathode}$ are the anode and cathode reaction overpotentials. $i * \sum R$ can be seen as the ohmic voltage drop, and must be minimized to minimize the applied cell voltage. This will directly increase efficiency, as does lowering U_{rev} or η_x. Development of AEC cell technology therefor focuses on these areas.

2.3. Reaction- and system kinetics

In this chapter insight in the kinetics of an AEC system is provided.

2.3.1. Electrode kinetics

As the reactions take place at the surface of the electrodes, insight on reaction mechanisms and affecting parameters is instrumental. Qualification of the parameters affecting the kinetics of these reactions will now be addressed, and if possible quantification as well.

It is possible to describe simple electrochemical redox reactions using the Butler-Volmer equation, equation 2.20, with α as electron transfer coefficient (also known as symmetry factor)[65]. What can be observed is that for certain overpotentials, either the first or the second exponential becomes dominant. For $\eta > 0.1\ V$ the first exponential becomes negligibly small compared to the second, which means the anodic reaction, i.e. oxidation reaction becomes dominant. While for $\eta < -0.1\ V$ the second exponential becomes negligibly small compared to the first, which means the cathodic reaction i.e. reduction reaction becomes dominant. As a consequence, for relatively large overpotentials $|\eta| > 0.1V$, the Butler-Volmer equation can be simplified to the emperical Tafel equation, equation 2.21, which is an approximation of the Butler-Volmer equation [7].
Tafel analysis leads to two important physical parameters: the Tafel slope b and the exchange current density i_0, which enable prediction of rate of electrode surface reactions [65]. The Butler-Volmer equation and Tafel equation make it possible to evaluate the relationship of overpotential η and current density i.

$$i = i_0(e^{-\alpha \frac{F\eta}{R^{gas}T}} - e^{(1-\alpha)\frac{F\eta}{R^{gas}T}}) \tag{2.20}$$

$$\eta = a + b \cdot log i \tag{2.21}$$

a And b are both Tafel constants, where a represents the overpotential at $i = 1000\, mA/cm^2$. a Is influenced by intrinsic properties and surface morphology of electrode material [75]. By rewriting equation 2.20 into equation 2.21 form, a can be made explicit: equation 2.22 [65].

$$a = \frac{R^{gas}T}{\alpha F} ln(i_0) \tag{2.22}$$

As mentioned before, electrode materials and morphology greatly influence the reaction overpotential, and therefor reaction kinetics. When looking at values for Tafel constant a, pure metals for cathode material supporting the HER can be divided into three classes [75], which can be observed in table 2.1. It must be noted that with treatment of these metals with respect to surface structure and morphology significant performance gains can be observed, as we'll see later on. Table 2.1 does however provide insight in catalytic properties of solely pure metals compared to each other.

High η	Cd, Tl, Hg, Pb, Zn, Sn etc.
Middle η	Fe, Co, Ni, Cu, Au, Ag, W etc.
Low η	Pt, Pd

Table 2.1: Pure metals divided into classes according to their respective overpotentials supporting HER

The slope of the Tafel plot, known as the Tafel slope b, indicates the rate at which overpotential increases when increasing the current density. It provides insight in the reaction mechanisms taking place at the surface of the electrodes, and what are the rate determining steps.

Cathode - HER
At the cathode, water is being reduced according to three steps, with M as electrode surface empty site [65]:

$$\text{(Volmer step)} \qquad H_2O + e^- + M \rightleftharpoons \mathrm{M}\text{---}\mathrm{H} + OH^- \tag{2.23}$$

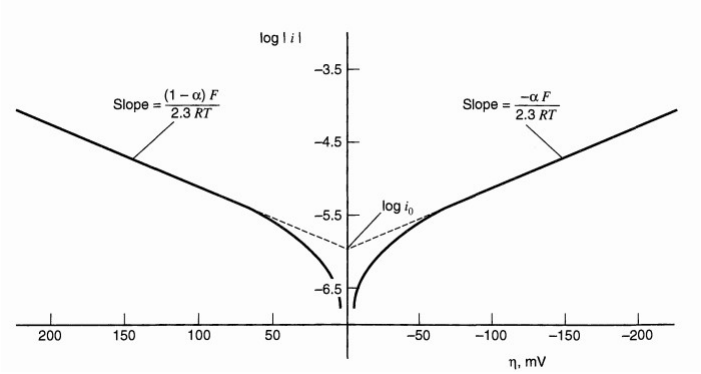

Figure 2.5: Example: Tafel plots for anodic (left) and cathodic (right) branches of the current-overpotential curve, depicted for an electrolysis reaction with $\alpha = 0.5$, $T = 298\ K$ and $i_0 = 10^{-6}\ A/cm^2$. Adapted from Bard et al. [7]

$$\text{(Tafel step)} \qquad 2\,\mathrm{M}\text{——}\mathrm{H} \rightleftharpoons H_2 + 2M \tag{2.24}$$

$$\text{(Heyrovsky step)} \qquad \mathrm{M}\text{——}\mathrm{H} + H_2O + e^- \rightleftharpoons H_2 + OH^- + M \tag{2.25}$$

For each of the steps the forward reaction rates can be determined. If then the overall reaction rate is considered, the rate determining step can be identified. The forward reaction rates of each step can be determined with [65]:

$$\text{(Volmer step forward reaction rate)} \qquad r_{A.1} = k_{A.1} a_{H_2O} (1 - \theta_{H_2}) \tag{2.26}$$

$$\text{(Tafel step foward reaction rate)} \qquad r_{A.2} = k^0_{A.2} \theta^2_{H_2} \tag{2.27}$$

$$\text{(Heyrovsky step foward reaction rate)} \qquad r_{A.3} = k_{A.3} a_{H_2O} \theta_{H_2} \tag{2.28}$$

In these equations, r_j is the reaction rate and k_j is the kinetic rate constant for equation j, while a_{H_2O} is the water ion activity and θ_{H_2} the surface coverage ratio by hydrogen.

When the rate determining step is identified, it is possible to derive an equation for the electric current flowing, which is rate determining step specific. These derivations can be found in detail in appendix A.1.

Anode - OER

On the anode surface, oxygen evolution reaction OER happens according to a 5 step process, assuming a single-site reaction mechanism [65]:

$$\text{(Step 1)} \qquad M + OH^- \rightleftharpoons MOH + e^- \tag{2.29}$$

$$\text{(Step 2)} \qquad MOH + OH^- \rightleftharpoons MO + H_2O + e^- \tag{2.30}$$

$$\text{(Step 3)} \qquad MO + OH^- \rightleftharpoons MOOH + e^- \tag{2.31}$$

$$\text{(Step 4)} \qquad MOOH + OH^- \rightleftharpoons MOO^- + H_2O \tag{2.32}$$

$$\text{(Step 5)} \qquad MOO^- \rightleftharpoons M + O_2 + e^- \tag{2.33}$$

As for the cathodic steps, its also possible to determine the reaction rates of the five steps at the anode, with that identify the anodic rate determining step and derive an expression for the electric current for that particular step. This is done in detail in appendix A.2.

All electrochemical reactions can thus be evaluated according to the reaction kinetics. This is possible by evaluating the Tafel slope, although it's intercept with the vertical axis might not always be equal to the exchange current i_0. The reason for this is that in practice the interface is not always in equilibrium with the surrounding solution, which is assumed in the Butler-Volmer equation [65].

The electrocatalytic activity of the electrodes is not only influenced by the applied potential, but also by temperature [65]. This in turn affects the Tafel slope. Shinagawa et al. recons this change in Tafel slope is due to the temperature dependence of the reaction rate constant, which follows the Arrhenius equation 2.34 [65].

$$k = f e^{\frac{-E_A}{R^{gas}T}} \tag{2.34}$$

In the Arrhenius equation f is the frequency factor (frequency of collisions), which is reaction specific. E_A is the activation energy, R the gasconstant and T the temperature. Although f is temperature dependent, its dependency is marginal compared to that of the second term $e^{\frac{-E_A}{R^{gas}T}}$. What can be observed is that with increasing temperature the reaction rate increases as well, which in term means an increase in Tafel slope [65]. But, as can be observed in equations A.7, A.13, A.23 and A.24, the kinetic rate constant can also be expressed in terms of the transfer coefficient α [7]. As a consequence, the Tafel slope is also transfer coefficient dependent [65].

Theoretically, the cell current density i can be determined using equation 2.35, where I is current intensify and A is the geometrical surface area of electrode [75]. Real current density will however differ from this due to various phenomena.

$$i = \frac{I}{A} \tag{2.35}$$

The effective electrode area A_{eff} as result of the aforementioned phenomena also plays an important role on reaction kinetics. It is related to morphology and surface roughness, which is determined by electrode preparation [25]. The previously mentioned bubble effect influences the effective electrode area as well. Bubbles containing product gas accumulate on the electrode surface, acting as an electric shield [75]. As the effective active area is reduced, the current distribution on the electrode surface is disturbed, causing an increase in current density, according to equation 2.36 [75], with θ_{bub} as the bubble coverage ratio. When looking at equation 2.37, this increase in current density leads to greater overpotentials as $0 < \theta_{bub} < 1$, which increases cell voltage and lowers efficiency.

$$i_{\theta bub} = \frac{I}{A_{eff}} = \frac{I}{A(1-\theta_{bub})} \tag{2.36}$$

$$\eta_{\theta bub} = a + b \cdot log i_{\theta bub} = a + b \cdot log \frac{I}{A(1-\theta_{bub})} = \eta + b \cdot log \frac{1}{1-\theta_{bub}} \tag{2.37}$$

Studies have shown that with increasing current density and temperature, bubble coverage goes up, as can be observed in figure 2.6 [75]. Krenz reported an increase factor in bubble coverage ratio of around 1.5, when temperature was increased from $25°C$ to $50°C$ [35].

Polarization curves provide a mean to compare the catalytic performance of electrodes. It must however be noted these curves can differ significantly from one researcher to another due to differences in cell design and operating conditions, which greatly influence the polarization curves as well [11]. This makes it more difficult to compare results between researchers. Figure 2.7a and 2.8a show HER and OER polarization curves for different electrode materials. The catalytic properties of Raney nickel

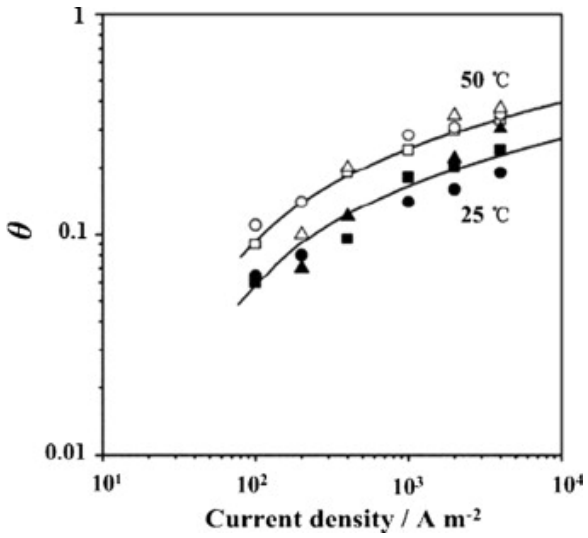

Figure 2.6: Bubble coverage ratio θ as function of current density. Adapted from Wang et al. [75]

for the hydrogen evolution reaction are easily observable, as it outperforms other cathode electrode materials significantly [11].

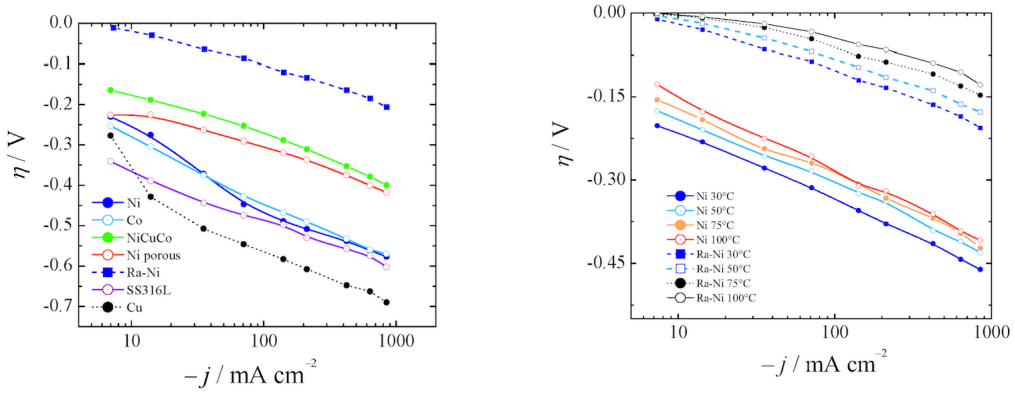

(a) Polarization curves for several electrode materials, for HER at 30 °C

(b) Comparison of aged Ni and Ra–Ni between 30 and 100 °C

Figure 2.7: Polarization curves for different electrode materials for the hydrogen evolution reaction HER, adapted from Colli et al. [11]

For the OER at the anode porous nickel does not yield the same catalytic properties as for the HER, as can be seen in figure 2.8a. Porous nickel actually results in slightly higher overpotentials for OER compared to regular nickel. This is attributed to the lack of ability of the larger O_2 bubbles to penetrate into the pores, and make use of the extra surface area [4]. It is however a sacrifice worth making, as performance gains on the cathode side outweigh the losses on the anode side.

What can be observed in figures 2.7b, 2.8b and 2.9 though is that for both HER and OER elevated temperatures result in a decrease of reaction overpotential. This drop in overpotential causes reaction rates to go up when temperature is increased, and also explains the increase in bubble coverage as previously observed in figure 2.6. Elevated temperatures also affect electrolyte properties, as will be explained in section 2.3.2.

As can be observed is that figures 2.7/2.8 and figure 2.9 are slightly different in shape. The main difference between their voltammetric analysis is that Colli et al. performed voltammetry on anode and cathode separately, while Ju et al. performed voltammetry on the cell as a whole [11][28]. The advantage of separate anode and cathode voltammetry is that it provides more insight in individual re-

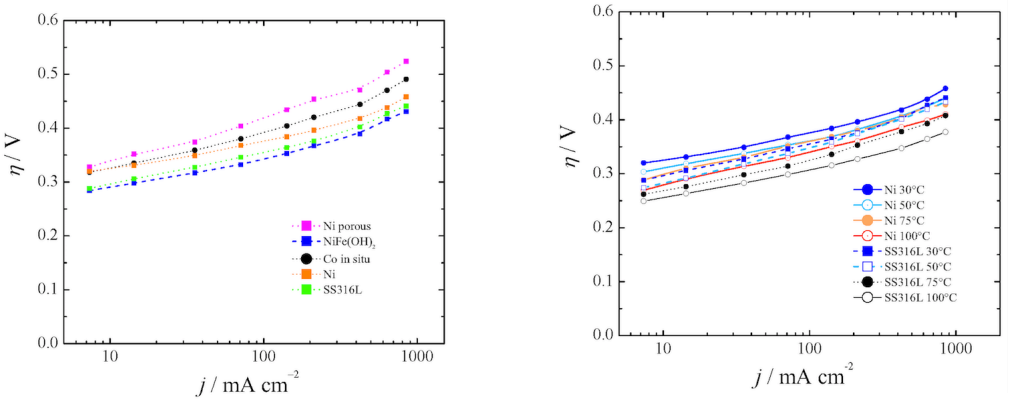

(a) Polarization curves for several electrode materials, for OER at 30 °C

(b) Comparison of Ni and stainless steel SAE 316L between 30 and 100 °C

Figure 2.8: Polarization curves for different electrode materials for the oxygen evolution reaction OER, adapted from Colli et al. [11]

actions, opening up the opportunity to determine the rate limiting steps at either electrode as explained in section 2.3.1. This does however require a third electrode, the reference electrode, as mentioned previously. In voltammetry on the overall cell, like in figure 2.9, the overpotential is calculated by subtracting the equilibrium voltage from the measured overall cell voltage at a certain temperature and current density. This calculated overpotential primarily comes from the activation of both cathodic HER and anodic OER, equation 2.38, but distinguishing their individual contributions is not possible via this route. The same applies for the Tafel slope, as it is the superposition of individual HER and OER Tafel slopes, equation 2.39 [28].

$$\eta_{overall} = \eta_{HER} + \eta_{OER} \tag{2.38}$$

$$b_{overall} = b_{HER} + b_{OER} \tag{2.39}$$

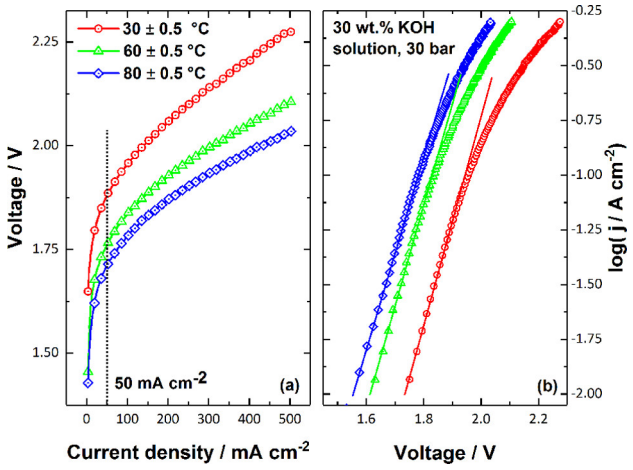

Figure 2.9: Voltammetric curves on the left and respective Tafel plots on the right for 30°C, 60°C and 80°C at cell pressure of 30 bar. Adapted from Ju et al. [28]

2.3.2. Electrolyte kinetics

As mentioned previously, **conductance** of electrolyte has substantial impact on the cell efficiency. This is the reason why electrolyte solutions are being utilized instead of pure water for water electrolysis, even though decreasing water activity as a result of increasing electrolyte concentration causes an increase in overpotential to split water. This increase was found to be about $10\,mV$ at room temperature

when electrolyte concentration was increased from $0\ wt\%$ to $30\ wt\%$ KOH. This is however a sacrifice worth making, as Colli et al. found that equilibrium potentials for both HER and OER dropped with $70 - 90\ mV$ due to decreased resistance [11]. The drop in overall equilibrium cell voltage is their individual equilibrium potential drop combined. And as conductivity directly influences the cell resistance, it's easy to see why KOH electrolyte solutions are preferred over NaOH solutions in the industry, as it's conductivity is up by a factor of 1.5 at respective optimum concentration levels (figure 2.10).

As can be observed in figures 2.10 and 2.11, an optimum electrolyte concentration exists for both KOH and NaOH solutions. The drop in conductivity at superoptimal electrolyte concentrations could be attributed to a reduction in ionic mobility due to increased viscosity [47].
In literature typically two concentration units are being used: molarity M and weight percentage $wt\%$. Equation 2.40 can be utilized to convert one into the other, with the aqueous electrolyte solution density $\rho_{electrolyte}$ in kg/m^3 and the molecular weight of the electrolyte additive M_w in g/mol [22]. The optimum KOH electrolyte concentration of $30\ wt\%$ corresponds to a molarity of $6.851\ M$ [28][24].

$$M = \frac{wt\% \cdot \rho_{electrolyte}}{100 \cdot M_w} \tag{2.40}$$

What can also be seen in figures 2.10 and 2.11 is that conductance of the electrolyte increases at elevated temperature, directly decreasing resistance. Once again viscosity effects play a significant role. Ju et al. found that with a temperature increase from $30°C$ to $80°C$ the ionic resistivity dropped from $1.393\ \Omega cm$ to $0.675\ \Omega cm$ for a $32\ wt\%$ KOH solution [28]. And as the diaphragm is saturated with electrolyte, here too a drop in resistivity is measured. Vermeiren et al. reports a drop in ionic resistivity from $4\ \Omega cm$ to $2\ \Omega cm$ for the same $32\ wt\%$ KOH solution over a $0.5\ mm$ thick Zirfon diaphragm, further lowering the cell resistance and affiliating IR-drop [72]. Ju et al. therefor reckons this is the primary factor in lower cell voltages at elevated temperatures [28].

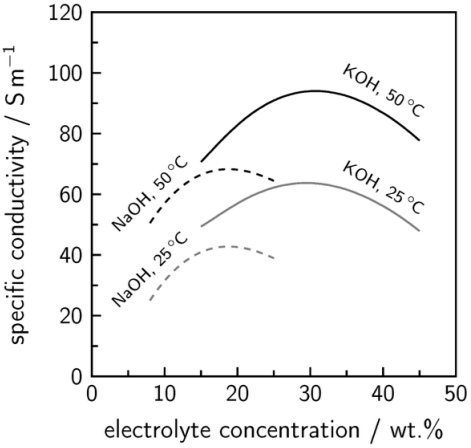

Figure 2.10: Specific conductivity of KOH and NaOH solution electrolytes at different concentrations, adapted from Brauns et al. [10]

In order to quantify the specific conductance of electrolyte solutions, Gilliam et al. developed an empirical relationship between molarity M in mol/L, temperature T in Kelvin and specific conductance κ in S/cm using a non-linear regression analysis program. Over 300 data points were used from multiple sources, to obtain equation 2.41 [22][32][64][18][15].

$$\kappa = -2.041M - 2.8 \cdot 10^{-3}(M^2) + 5.332 \cdot 10^{-3}(M \cdot T) + 207.2\left(\frac{M}{T}\right) + 1.043 \cdot 10^{-3}(M^3) - 3 \cdot 10^{-7}(M^2 \cdot T^2) \tag{2.41}$$

The Gilliam equation matches data from experiments quite well, as can be observed in figure 2.11. For temperatures ranging from $0 - 100°C$ and concentrations ranging from 0-12 M the correlation coefficient was found to be 0.998 [22]. What can be observed is that not only the specific conductance is dependent on temperature, but the optimum electrolyte concentration slightly as well, with optimum

concentration marginally increasing at elevated temperature. This could be attributed to a slight increase of KOH solubility at elevated temperatures.

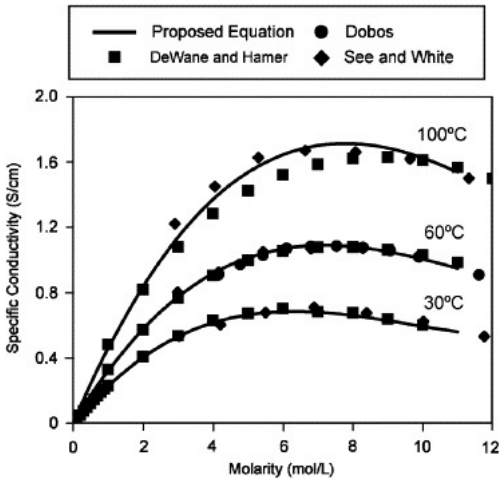

Figure 2.11: Specific conductivity of KOH solution electrolyte at different temperatures as function of concentration, adapted from Gilliam et al. [22]

Hamann et al. found that KOH electrolyte solution conductivity is also dependent on pressure [23]. They measured an increase in conductivity of 29% when pressure was increased from atmospheric to a shock wave pressure of 7500 bar. Although this increase in conductivity for this pressure increase is significant, for the pressure range of the AEC system (1-50 bar) it's safe to assume the conductivity as independent on pressure [40].

The equilibrium potentials for both anode and cathode are dependent on **electrolyte pH**. Pletcher et al. found that as both electrode reactions involve 1 H^+ or e^-, they will shift at the same rate of $-59.6\ mV/pH$ at $298\ K$ [49]. As both equilibrium potentials shift by the same amount, the difference between the two, the equilibrium cell voltage, is not dependent on electrolyte pH.

It's convenient to know how process conditions influence the gas **solubility** in the electrolyte, as dissolved product gasses bring forth several problems. In general, increasing electrolyte concentration means gas solubility becomes lower, due to a phenomenon called salting-out [10][24][66][76]. In literature several theories are presented which would explain this salting-out behaviour [56]. These theories are based on electrostatic, internal pressure and hydration effects. Calculations based on the latter theory produce qualitatively and quantitatively accurate predictions, and is based on the assumption that some of the water molecules become attached to the electrolyte ions as hydration, and as a result these water molecules lose their role of solvent. This means as more electrolyte is solved in water, there are less water molecules remaining for other substances to dissolve in, decreasing gas solubility. Haug et al. utilized the Setchenov relation 2.42 which is based on this theory to predict O_2 and H_2 solubility for varying electrolyte concentrations, with $S_{x,0}$ and $S_{x,s}$ as gas species x solubility in pure water and electrolyte solution respectively and M the molarity of the electrolyte solution. $C_{Setchenov}$ is the Setchenov constant, which is specific to dissolved gas and electrolyte substance and slightly dependent on temperature [24][62]. The result of Haug's work can be observed in figure 2.12, where modeled values follow measured values quite well [24]. The salting-out behaviour is easily observable as gas solubility drops significantly with increasing KOH concentration. NaOH electrolyte solutions exhibit this behaviour even more than KOH electrolyte solutions [10]. However, higher concentration electrolyte solution does come with drawbacks such as increased corrosivity. It must also be noted that this salting-out behaviour is temperature dependent, as its effect decreases at elevated temperature [66].

$$log(\frac{S_{x,0}}{S_{x,s}}) = C_{Setchenov} \cdot M \tag{2.42}$$

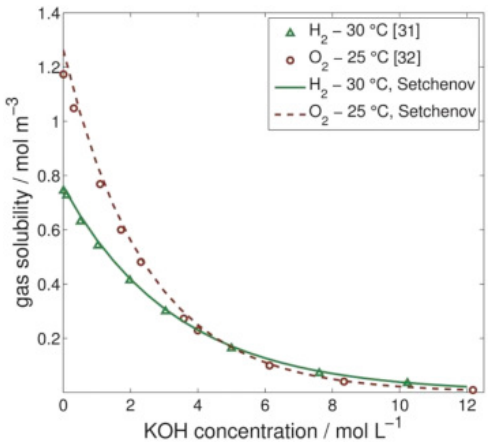

Figure 2.12: O_2 and H_2 solubility versus KOH electrolyte solution concentration at atmospheric pressure, adapted from Haug et al. [24]

Operating pressure has a major effect on the amount of gas dissolved. Higher pressure means higher amounts of dissolved gas, as governed by Henry's law equations 2.47 and 2.48 [76]. This effect is magnified due to a decrease in mean gas bubble diameter as a result of this higher pressure. This makes gas separation more difficult, aiding to other unwanted effects such as product gas crossover which will be explained shortly [70].

Operating temperature also influences gas solubility. When temperature of a solution of solvent and dissolved gas is increased, the kinetic energy of the both solvent and solute increases as well. This generally means the molecules of the dissolved gaseous species have more energy to free themselves from the attraction to the solvent molecules, enabling more molecules to return to the gas phase. As a result typically gas solubility becomes lower at elevated temperatures [76]. However, research has shown that although this holds for low electrolyte concentration, at concentrations higher than $10\ wt\%$ KOH H_2 solubility actually increases, as can be seen in figure 2.13a [58]. Here the H_2 solubility was deduced by rearrangement of Fick's law, dividing H_2 diffusivity obtained from experiments by the H_2 diffusion coefficient at certain temperatures and electrolyte concentrations. Literature reports several possible explanations for the phenomena, and it holds true when gas solubility is very low, below a mole fraction of ~10^{-4}, and especially when its critical temperature is low as well [52][33]. It is actually the salting-out behaviour which lowers solubility towards this region, which causes the shift from negative to positive temperature coefficient of solubility.
For the oxygen solubility a similar trend can be observed, although this shift from negative to positive temperature coefficient of O_2 solubility occurs at KOH concentrations above $8\ M$, as can be seen in figure 2.13b [14]. At $30\ wt\%$ KOH solution (which equals $6.851\ M$) it can observed that raising the temperature from $25°C$ to $60°C$ will marginally lower the O_2 solubility in the electrolyte. The difference in behaviour could be attributed to the difference in critical temperature of hydrogen and oxygen, which means there is a difference in partial molar entropy change of H_2 compared to O_2 when temperature is increased [50].
For comparison sake, it can be seen in figures 2.13a and 2.13b that for $30\ wt\%$ KOH solution at $25°C$ the $S_{H_2} \approx 0.8 S_{O_2}$, while at $60°C$ this has shifted due to aforementioned phenomena to $S_{H_2} \approx 1.5 S_{O_2}$.

Electrolyte **dynamic viscosity** is, like in other fluids, dependent on temperature, pressure and electrolyte concentration. Increasing electrolyte concentration will increase viscosity, while increasing temperature will decrease viscosity [67][38]. For the ZEF AEC temperature range the dynamic viscosity of $30 wt\%$ KOH solution is substantially affected, as a drop by a factor of 2 is reported when temperature is increased from $20°C$ to $69°C$ at a pressure of 1 bar [38]. Viscosity's dependency on pressure however only becomes substantial at very high pressures, above 1000 bar [76]. For the pressure range of the

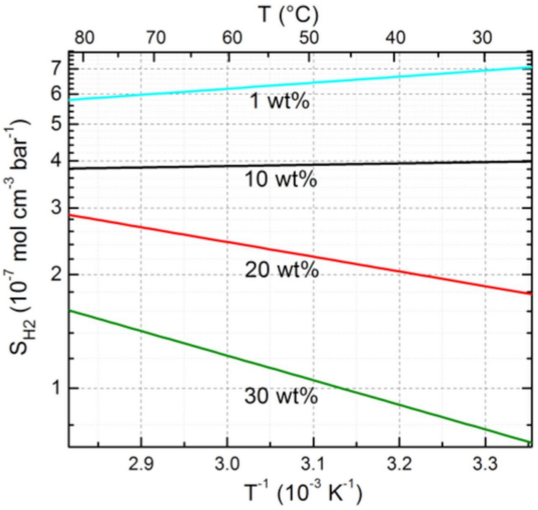

(a) H_2 solubility versus temperature for several electrolyte solution KOH concentrations, adapted from Schalenbach et al. [58]

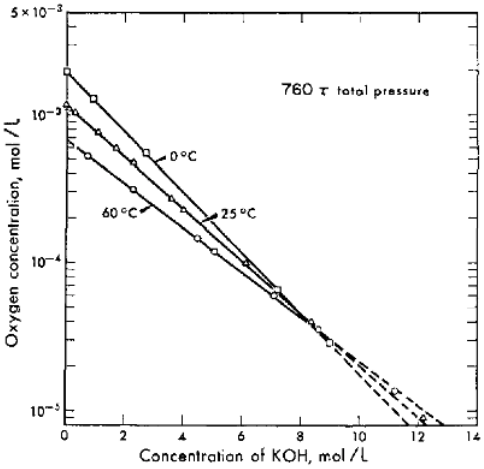

(b) O_2 concentration versus electrolyte solution KOH concentration at $0°C$, $25°C$ and $60°C$, adapted from Davis et al. [14]

Figure 2.13: Graphs to illustrate solubility's dependency on temperature and electrolyte concentration

AEC system of 1-50 bar it is therefor assumed the electrolyte viscosity to be independent on pressure.

When **bubbles** detach from the electrodes' surfaces, they are no longer part of the first layer of bubbles attached to the surface, but enter a second layer of bubbles floating through the electrolyte up to the product gas collecting area, causing convection (pumping effect) [27][45]. The bubbles rise through the electrolyte solution due to their relatively low density. As can be observed in figure 2.14, this second bubble layer becomes increasingly thick higher up the electrode. This is because of the resulting concentration gradient of gas in electrolyte as more and more bubbles are formed and become detached, moving the bubbles in y-direction [75]. In order to quantify the effects of the bubble layer on electrolyte resistance and subsequent parameters, the void fraction (volume fraction) ϵ introduced in section 2.2.1 is utilized. As product gas bubbles' ion conductivity is negligible compared to electrolyte ion conductivity, void fraction, describing the amount of dispersed bubbles in the electrolyte, affects the overall ion conductivity of the electrolyte as well. Factors influencing the void fraction are pressure, current density, bubble layer thickness, bubble size etc. [75]. Estimation of the void fraction and the effects it has on resistivity can be done with the Bruggeman equation, equation 2.43 [27].

$$\frac{R_\epsilon}{R_e} = (1-\epsilon)^{-\frac{3}{2}} \tag{2.43}$$

R_ϵ Represents the overall electrolyte resistance when there are bubbles in the solution i.e. the effective resistance, whereas R_e represents the pure electrolyte resistance, without bubbles. In practice it is quite challenging to measure the difference in Ohmic resistance between upper part of the electrodes, where bubble dispersion is more substantial, and lower, less affected, part of the electrodes due to the rapid movement of the bubbles [75]. Janssen et al. therefor simulated the real life situation by substituting gas bubbles by glass beads, and found that the Bruggeman equation gives a decent fit to measured values of resistivity [27]. For $0.200 < \epsilon < 0.605$ the error between calculated Bruggeman equation resistivity and measured values is in the order of 10% and for $\epsilon < 0.200$ the error is even smaller, which means the Bruggeman equation describes the resistivity of both the first and second bubble layer quite well [27]. As mentioned before, void fraction can be influenced by many different parameters. Matsushima et al. managed to lower void fraction by implementing an external magnetic field which causes magnetohydrodynamic convection [45]. The resulting drop in relative resistivity can be observed in figure 2.15 for varying magnetic field strengths and current densities.

2.3.3. Diaphragm kinetics

As mentioned previously, good ionic conductivity of diaphragm results in lower ohmic losses in the system. In order to test the ionic resistance of the Zirfon diaphragm, Vermeiren et al. measured cell

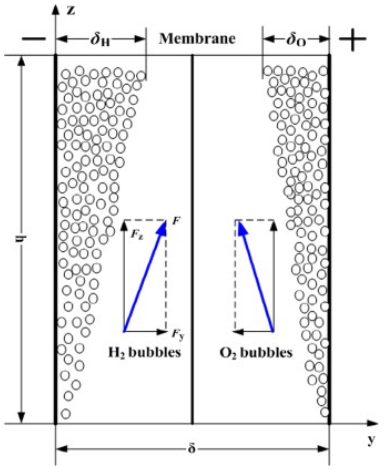

Figure 2.14: Bubble layer on electrode in electrolyte (non zero-gap). Adapted from Wang et al. [75]

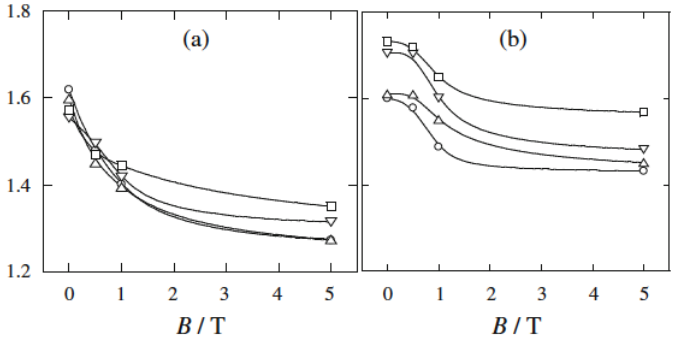

Figure 2.15: Relative resistivity $\frac{R_\epsilon}{R_e}$ versus magnetic field strength B in $[T]$ for cathodic half-cell (a) and anodic half-cell (b) for a current density of $100\ mA/cm^2$(circles), $300\ mA/cm^2$(triangles), $600\ mA/cm^2$(inverted triangles), $1000\ mA/cm^2$(squares). Adapted from Matsushima et al. [75]

resistance with and without a Zirfon diaphragm using a conductivity meter [72]. The ionic resistance is then the difference between the two measured values. The results can be observed in table 2.2.
As mentioned previously, Zirfon diaphragms consist of a polysulfone fabric impregnated with zirconium dioxide (ZrO_2). The final product contains $85\ wt\%\ ZrO_2$ and $15\ wt\%$ polysulfone [73].

In order to quantify the rate of diffusion through the membrane, Fick's law can be adopted. This will be explained in detail in section 2.3.4.

Properties	**Mean value**
Density	$1.4\ g/cm^3$
Tensile strength (dry)	$2.1\ MPa$
Tensile strength (KOH)	$2.1\ MPa$
Elongation (dry)	23%
Elongation (KOH)	32%
Porosity	60%
Thickness	$0.5\ mm$
Bubble pressure	$0.4\ MPa$
Ionic resistance ($30°C$)	$0.2\ \Omega cm^2$
Ionic resistance ($80°C$)	$0.1\ \Omega cm^2$

Table 2.2: Zirfon diaphragm characteristics, adapted from Vermeiren et al. [73]

2.3.4. Gas crossover - Product gas quality

Because of the explosive nature of a mixture of the product gasses formed in this process, gas crossover is a point of ongoing research. From a safety point of view, knowledge and understanding of crossover to either side is paramount. In terms of hydrogen crossover to the anodic half-cell a concentration of only 4 mol% hydrogen in the oxygen product flow is the lower explosion limit (LEL), whereas for oxygen crossover to the cathodic half-cell a concentration of 4.8 mol% oxygen in the hydrogen product flow is the upper explosion limit (UEL) at atmospheric conditions [60]. Increasing the temperature to $80°C$ will lower both these values by 0.2 mol%, while increasing pressure to 50 bar raises them again by 1.5 mol% and 0.5 mol% respectively, yielding an LEL of 5.3% and UEL of 5.1%.

As the ZEF AEC system will ultimately operate dynamically, the UEL and LEL will be evaluated at respective conditions. Reaching 50% of either LEL or UEL is considered the technical safety limit, at which shutdown of electrolyser system should be executed [10][61][70][63]. Literature does state that oxygen crossover is secondary to hydrogen crossover in terms of absolute amount, due to inherent hydrogen characteristics such as solubility and molecule size [63][61]. Yet, apart from the obvious importance of safety, knowledge on oxygen crossover to the cathodic half-cell is also of interest for other reasons. If the product gasses are to be used in subsequent processes, certain quality standards should be met to omit the need for purification. This is why oxygen crossover will not be neglected in this research, despite it posing less of a safety hazard than hydrogen crossover.

There are multiple ways gas crossover can occur inside an AEC system: it can happen either by diffusion, or it can happen by convection [70].

Diffusion

Diffusion of product gasses can occur through either the solid or through the liquid phase of what separates the cells, although in literature diffusion through the solid phase of the Zirfon diaphragm is assumed to be negligible compared to diffusion through liquid phase [70]. And as the diaphragm is assumed to be impermeable for gas bubbles up until a pressure difference of 5.5 bar, only species dissolved in the electrolyte solution are considered for diffusion across the diaphragm [58][74]. As diffusion through pores of a diaphragm is quite similar to diffusion in tubes, it can be described by the same equations if suitable parameters characterizing the pores inside the diaphragm are implemented [20]. Quantification could therefor be done by applying Fick's law of diffusion, equations 2.44 and 2.45 [70]. D_{eff,O_2} and D_{eff,H_2} are the effective diffusion coefficients of oxygen and hydrogen in the diaphragm. Δc_{O_2} and Δc_{H_2} are the concentration gradients of the dissolved species across the diaphragm, while δ_{sep} represents the thickness of the diaphragm. It is important to note that only at standard conditions the mean free path of both product gasses is comparable in terms of scale to the pore size of the diaphragm, which would mean Knudsen diffusion is taking place at those conditions. Yet, when the pressure is raised to 2 bar, they differ by roughly a factor of 2, up to a factor of 50 at 50 bar operating pressure. Since the operating pressure of the AEC will be in the range of 50 bar, only diffusion outside the Knudsen region will be discussed.

$$\Phi_{O_2}^{diff} = D_{eff,O_2} \frac{\Delta c_{O_2}}{\delta_{sep}} \tag{2.44}$$

$$\Phi_{H_2}^{diff} = D_{eff,H_2} \frac{\Delta c_{H_2}}{\delta_{sep}} \tag{2.45}$$

The effective diffusion coefficients can be approximated by correcting the normal diffusion coefficients of the dissolved species in electrolyte solution with characteristics of the pores. It is done by multiplying the normal diffusion coefficient D_x by a constant of proportionality, which is a characteristic of the internal geometry of the porous diaphragm, as can be seen in equation 2.46 [20][70]. The constant of proportionality being $\frac{\phi}{\tau}$, where ϕ and τ are the porosity - and tortuosity factor respectively. What can also be seen in equation 2.46 is that porosity, and thus pore size, has a strong effect on product gas diffusion towards the other side of the diaphragm [42]. It is reported that hydrogen diffusion coefficient in KOH solution is about three times higher than the oxygen diffusion coefficient, which could partially explain why it is likely more hydrogen will crossover through diffusion compared to oxygen [63][70]. Still, as mentioned before for the purpose of this research diffusion of oxygen will not be neglected.

It is reported that the diffusion coefficients dependency on pressure is negligible in liquids, while its dependency on temperature is significant [58]. The effect of temperature on the diffusion coefficient for dissolved gasses can be approximated by the Stokes-Eistein equation, and it has been reported that H_2 diffusion coefficient in $30\ wt\%$ KOH solution increases roughly logarithmic with temperature. An increase by a factor of over 3 is reported when temperature is increased from $25°C$ to $80°C$, from ~$1.6 \cdot 10^{-5}\ cm^2/s$ to ~$6 \cdot 10^{-5}\ cm^2/s$ [69]. It must be noted that O_2 diffusion coefficient is equally dependent on temperature. Yet, as mentioned previously the H_2 diffusion coefficient is significantly higher in absolute terms; $D_{H_2} \approx 3D_{O_2}$.

$$D_{eff,x} = D_x \frac{\phi}{\tau} \tag{2.46}$$

For the calculation of the concentration of dissolved species in electrolyte, Henry's law can be utilised. As can be seen in equations 2.47 and 2.48, Henry's law states that the amount of dissolved gas in the liquid electrolyte solution is proportional to its partial pressure in the gas phase on that side of the cell [70]. The solubility of species x in electrolyte solution is represented by $S_{x,s}$, while p_x denotes the partial pressure in the gas phase.

$$c_{O_2} = S_{O_2,s} p_{O_2}^{an} \tag{2.47}$$

$$c_{H_2} = S_{H_2,s} p_{H_2}^{cat} \tag{2.48}$$

If we assume that anodic hydrogen partial pressure and cathodic oxygen partial pressure are negligible, and that the product gasses are saturated with water vapour, then product gas partial pressures can be calculated using equations 2.49 and 2.50 [70]. p^{an} and p^{cat} represent total anodic and total cathodic pressure respectively. Balej provides an equation for the equilibrium partial pressure of water vapour over aqueous KOH electrolyte solution as function of molality and temperature [6]. This equation is valid for the ranges 0-60 wt% KOH solution and $0°C$ to $300°C$ and can be used to obtain $p_{H_2O}^{an}$ and $p_{H_2O}^{cat}$ [70].

$$p_{O_2}^{an} = p^{an} - p_{H_2O}^{an} \tag{2.49}$$

$$p_{H_2}^{cat} = p^{cat} - p_{H_2O}^{cat} \tag{2.50}$$

It is now possible derive the diffusional oxygen and hydrogen flux across the diaphragm, by implementing equations 2.47 and 2.48 into equations 2.44 and 2.45 respectively, to obtain equations 2.51 and 2.52 [70]. A typical material property for diaphragms is the diffusional permeability coefficient K_x^{diff} for species x, which is the product of Fick's effective diffusion coefficient D_x^{eff} and the solubility coefficient S_x [70]. Lower concentrations of KOH aqueous solution means values for diffusion and solubility coefficients increase towards values of pure water, thus increasing the permeability coefficient K_x. This means product gas crossover through diffusion becomes more relevant with lower electrolyte concentrations [70]. Other process conditions influence these parameters as well. Ju et al. [28] found that when the cell temperature is increased, oxygen crossover rises slightly. This could be attributed to the fact that although oxygen solubility in electrolyte solution slightly decreases at higher temperatures, the oxygen diffusion coefficient goes up, resulting in a net rise of diffusional oxygen permeation.

$$\Phi_{O_2}^{diff} = D_{O_2}^{eff} S_{O_2} \frac{p_{O_2}^{an}}{\delta_{sep}} = K_{O_2}^{diff} \frac{p_{O_2}^{an}}{\delta_{sep}} \tag{2.51}$$

$$\Phi_{H_2}^{diff} = D_{H_2}^{eff} S_{H_2} \frac{p_{H_2}^{cat}}{\delta_{sep}} = K_{H_2}^{diff} \frac{p_{H_2}^{cat}}{\delta_{sep}} \tag{2.52}$$

Convection

Crossover due to convection also happens as a result of dissolved product gas in electrolyte solution, and it can be subdivided into three mechanisms [70]:

Differential pressure over the diaphragm

Although differential pressures for AEC systems are typically not very large, it is still possible that convection crossover occurs through a differential pressure over both sides of the diaphragm. And as AEC systems use porous diaphragms as half-cell separators, it is in theory more prone to convective permeation compared to Nafion separators in PEM electrolysers for instance, which is why in this research it won't be neglected and quantification will follow. Low hydraulic permeability, as well as minimal pressure difference over the diaphragm are therefor desired as dissolved product gas could be carried towards the other side due to a pressure driven water or electrolyte flow [70].

Electro-osmotic drag through the diaphragm

As there is an electric field present inside the cell, the charge carriers, being hydroxide ions, move from cathode to anode. This movement of ions imposes a force on the electroneutral electrolyte solution, possibly dragging the solution with dissolved product gass through the diaphragm towards the anode side. This crossover mechanism might therefor stimulate hydrogen crossover, and reduce oxygen crossover [70]. This drag force is known as electro-osmotic drag, and it presents a pathway of convective crossover. There are very few reports in literature on quantification of this crossover mechanism. However, Li et al. found that for an alkaline direct ethanol fuel cell the diffusion of water from anode to cathode side due to a concentration gradient outweighs the backward water flux by electro-osmotic drag [41]. This might also be the case for an AEC electrolyser, yet further research is required to confirm this presumption. Trinke et al. provides equation 2.53 for a rough estimation of the electro-osmotic crossover flux of hydrogen, in which c_{elec} is the concentration of the electrolyte within the diaphragm and n_{drag} is the electro-osmotic drag coefficient [70]. This drag coefficient is the ratio between flux of dragged electrolyte molecules to that of the charge carriers.

$$\Phi_{H_2}^{drag} = \frac{S_{H_2} p_{H_2}^{cat}}{c_{elec}} \frac{n_{drag} i}{F} \tag{2.53}$$

Electrolyte mixing

As can be observed in reaction schemes 2.2 and 2.3 water is consumed at the cathode, and produced at the anode. As this is happening in an aqueous solution, an electrolyte concentration difference arises over anodic and cathodic half-cells. In order to even-out this concentration difference, it is typical for AEC systems to mix anodic and cathodic electrolyte cycles before re-entering the cells. Although this solution omits the need for more complicated electrolyte concentration control systems, it does present a major pathway for crossover, as the electrolyte is saturated with dissolved product gasses [70]. Dissolved hydrogen and oxygen are therefor continuously flowing into the cells, lowering gas purities. Trinke et al. reckons this is the main source of crossover, responsible for roughly 90% of crossover in mixed electrolyte AEC systems, as can be observed in figure 2.18[70].

As mentioned before, both crossover through convection and through diffusion happens due to dissolved gas in electrolyte. The solubility of which therefor has a major effect on gas purity [10]. The effects of process conditions on solubility have been mentioned before. To summarize:

- Higher pressure means more dissolved product gas. As a consequence a larger concentration gradient across the diaphragm is present meaning more crossover through diffusion and convection over diaphragm, as well as more dissolved gas in electrolyte solution streams when electrolyte cycles mix. The effect of this could mean a substantial rise in gas crossover, as can be seen in figure 2.16 [10][70].
- Higher electrolyte concentrations have the opposite effect, as product gas solubility drops due to salting-out behaviour. This leads to lower gas crossover by convection, as well as by diffusion [24].

- Higher operating temperatures mean diffusion coefficients go up, and with that crossover by diffusion for both gas species. In the case of hydrogen, solubility in $30\ wt\%$ KOH solution also increases at elevated temperature, while viscosity of the electrolyte drops. Both of these factors could possibly result in more crossover by convection.

The reduction of bubble size, and thus reduction in gas-liquid interface at higher pressures also add to crossover as mentioned before. The combined effect of this and higher amounts of dissolved gas at higher pressure is measured by Ju et al. [28]. Table 2.3 shows measured values for hydrogen purity at different pressures and temperatures. Less hydrogen purity indicating more cathodic oxygen content, and thus more oxygen crossover. Trinke et al. reports an increase of similar proportions. For a separated electrolyte cycle system they measured an anodic hydrogen content increase from $0.018\ vol\%$ to $0.130\ vol\%$ at a current density of $700\ mA/cm^2$ when the pressure was raised from 1 to 20 bar [70]. For a mixed electrolyte cycle system this increase was even greater, as anodic hydrogen content rose from $0.178\ vol\%$ to $2.564\ vol\%$, also at a current density of $700\ mA/cm^2$.

As mentioned before, despite a slightly decreased oxygen solubility at elevated temperature in $30\ wt\%$ KOH solution, Ju et al. measured an increase of oxygen crossover can be observed in table 2.3, which is very likely due to the increase of diffusion coefficient [28].

Pressure/temperature	30°C	40°C	60°C	80°C
1 bar	99.88 ± 0.03	99.69 ± 0.10	99.63 ± 0.12	99.60 ± 0.13
10 bar	99.31 ± 0.03	98.96 ± 0.19	98.87 ± 0.25	98.85 ± 0.27
20 bar	98.60 ± 0.11	98.13 ± 0.12	98.06 ± 0.06	98.04 ± 0.04

Table 2.3: Hydrogen purities in %, measured with constant current density of $502\ mA/cm^2$. Obtained by Ju et al.[28]

Supersaturation

What will aid to crossover for both convectional and diffusional mass transport modes, is that there is formation of supersaturated zones of dissolved gas species occurring in the vicinity of the electrodes [70]. It is assumed that produced gasses are formed in dissolved state before gas bubbles form at active nucleation sites on the electrode surfaces [19]. These nucleation sites will only become active if the local concentration of dissolved gas exceeds the equilibrium concentration by a sufficient amount. This means the electrolyte becomes supersaturated at the surface of the electrodes, exceeding values attained by applying Henry's law, equations 2.47 and 2.48 [70]. The presence of these supersaturated zones has been proven through various methods by multiple researchers [44] [30]. Trinke et al. found this to be the second largest source of hydrogen crossover through the separator, as illustrated in figure 2.18. This holds in particular for specific cell configurations where there is very little to no space in between electrodes and diaphragms, such as a zero-gap configuration [70]. A detailed explanation on such a configuration will be given in section 2.5.1. Daniil et al. simulated the effect of the supersaturated zones, and found that an increase in supersaturation by a factor of 10 leads to an increase of almost 1% anodic hydrogen concentration and 0.1% cathodic oxygen concentration [13].
In order to estimate the electrode surface concentration of dissolved gasses C^*, the Nernst equation, equation 2.54 can be utilized [44]. C^0 represents the saturated concentration of the respective dissolved gas at standard conditions, while η_{cs} represents the concentration overpotential. If we now define supersaturation, or super solubility, S^{sup} as the ratio of surface concentration and saturated concentration, equation 2.54 can be rewritten to equation 2.55 to give the supersaturation.

$$C^* = C^0 e^{-(\frac{2F}{R^{gas}T})\cdot\eta_{cs}} \tag{2.54}$$

$$S^{sup} = \frac{C^*}{C^0} = e^{-(\frac{2F}{R^{gas}T})\cdot\eta_{cs}} \tag{2.55}$$

Effect of current density on crossover

Knowledge on the effect of current density on crossover is also very important, as this is a parameter which could be set at a desired predetermined level to serve specific needs of the particular AEC system. Although the effect of current density is system specific, literature concurs that below a current density of around $400\ mA/cm^2$, lowering of current density actually increases gas impurity significantly

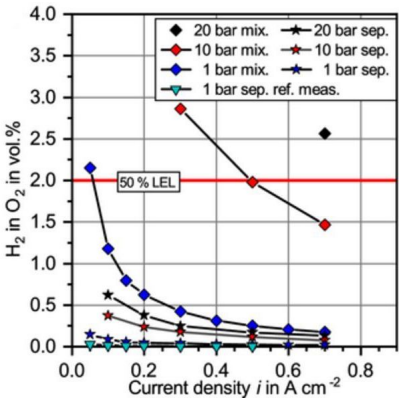

Figure 2.16: Anodic hydrogen content of AEC at $60°C$ and $30\ wt\%$ KOH aqueous solution, as function of current density. Adapted from Trinke et al. [70]

[70][61]. This can clearly be seen in figures 2.16 and 2.19. Ju et al. found similar results when simulating a shut-down/restart procedure, when hydrogen purity dropped significantly indicating crossover went up when current density was decreased, as can be seen in figure 2.17 (the delay in drop in purity is due to delay in gas measurement system utilized by Ju et al.) [28]. At first glance this looks like an increase in oxygen crossover at lower current densities. Yet, is is believed the flux of crossover gas actually stays relatively constant with varying current densities [10]. What is actually happening is that at lower current densities the oxygen and hydrogen evolution rates are low as well (low gas production), meaning the fraction of impurities is larger than at higher current densities [10][70]. This effect becomes increasingly relevant the lower is the current density. Apart from oxygen and hydrogen evolution rates being low at low current densities, literature also states that at low current density nearly all amount of product gasses is produced in dissolved form, meaning a smaller gas liquid interface, substantiating the problem [70].
The effect of increasing the current density from a value of $400\ mA/cm^2$ is less clear, and it is here that its dependence on system geometry becomes more apparent. Trinke et al. measured a slight though continues decline in gas impurity, as can be seen in figure 2.16 [70], while other researchers measured a slight increase in gas impurity, as can be seen in figure 2.19 [10][61]. What can be concluded from this though, is that current density is very likely to have a substantial effect on gas purities, especially below a current density of $400\ mA/cm^2$.

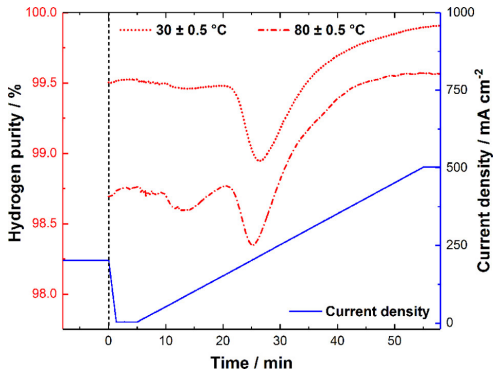

Figure 2.17: Measured hydrogen purity during shut-down/restart experiment at $30°C$ and $80°C$ cell temperatures. Adapted from Ju et al. [28]

Dominant crossover mechanism across diaphragm

As can be seen in figure 2.18, research by Trinke et al. shows that electrolyte mixing plays a substantial role in crossover [70]. Besides electrolyte mixing, supersaturated and saturated diffusion are mentioned as the remaining main contributors to H_2 crossover. It must be noted that in this case the pressure difference between both sides of the cell is assumed to be equal to zero. System config-

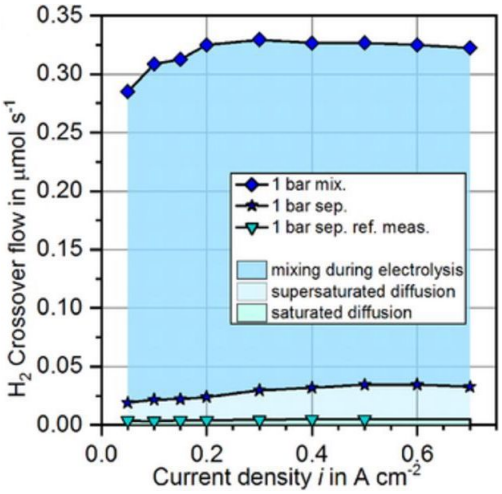

Figure 2.18: Hydrogen crossover mechanisms AEC. Adapted from Trinke et al. [70]

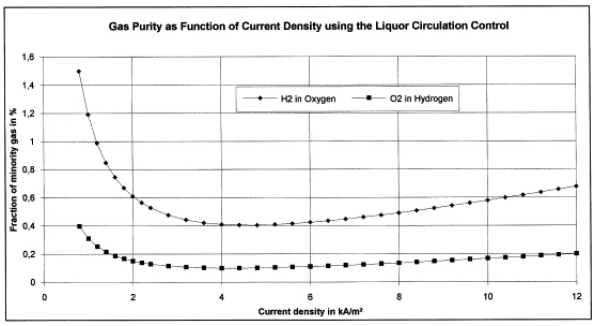

Figure 2.19: Product gas crossover as function of current density, with electrolyte circulation control. Adapted from Schug et al. [61]

urations without electrolyte mixing, which are inherently more susceptible to differences in half-cell pressure, are however conceivable. It is therefor interesting to see to what extend a pressure difference would affect crossover across the diaphragm, as this would be the main route for crossover in such system configurations.

Schalenbach et al. have quantified the effect of pressure difference by first multiplying Darcy's law for volumetric flux Φ_{elec} of fluid across a separator, equation 2.56, with Henry's law, equation 2.48, to obtain the amount of H_2 flowing through the diaphragm as a result of a pressure difference, $\Phi_{H_2}^{Darcy}$ in equation 2.57 [58]. μ Represents the dynamic viscosity of the electrolyte, while ΔP denotes the absolute differential pressure. The permeability K^{perm} was experimentally obtained by Schalenbach for a Zirfon diaphragm, for several electrolyte concentrations up until a pressure difference of 0.5 bar [58]. For $30\ wt\%$ KOH solution the mean permeability over a temperature range of $30°C$ to $80°C$ is $K^{perm} \approx 0.075\ cm^2$ [58].

$$\Phi_{elec} = -\frac{K^{perm}}{\mu}\frac{\Delta P}{\delta_{sep}} \tag{2.56}$$

$$\Phi_{H_2}^{Darcy} = \Phi_{elec} c_{H_2} = -S_{H_2,s} p_{H_2}^{cat} \frac{K^{perm}}{\mu}\frac{\Delta P}{\delta_{sep}} = -\mathrm{E}_{H_2}^{Darcy}\frac{\Delta P}{\delta_{sep}} \tag{2.57}$$

If we insert Henry's law into Fick's law of diffusion equation 2.45, it is possible to write the diffusional flux of H_2 as a function of the differential H_2 partial pressure, equation 2.58. If we assume the anodic H_2 concentration to be negligible compared to the cathodic hydrogen concentration, we can substitute $\Delta p_{H_2} \approx p_{H_2}^{cat}$. The H_2 diffusivity $\epsilon_{H_2}^{Fick}$ is obtained by multiplying the diffusion coefficient with the solubility, as presented in equation 2.59 [58].

$$\Phi_{H_2}^{diff} = -\epsilon_{H_2}^{Fick}\frac{\Delta p_{H_2}}{\delta_{sep}} \approx -\epsilon_{H_2}^{Fick}\frac{p_{H_2}^{cat}}{\delta_{sep}} \tag{2.58}$$

$$\epsilon_{H_2}^{Fick} = D_{H_2}S_{H2,s} \tag{2.59}$$

In order to put this into perspective the ratio of H_2 permeability to H_2 diffusivity across the diaphragm, and with that the ratio of H_2 fluxes will now be deduced, equations 2.60 and 2.61. As both permeability and diffusivity are dependent on solubility, their ratio is not.

$$\frac{\mathrm{E}_{H_2}^{Darcy}}{\epsilon_{H_2}^{Fick}} = \frac{K^{perm}}{\mu D_{H_2}}p_{H_2}^{cat} \tag{2.60}$$

$$\frac{\Phi_{H_2}^{Darcy}}{\Phi_{H_2}^{diff}} = \frac{K^{perm}}{\mu D_{H_2}}\Delta P \tag{2.61}$$

We now implement the Stokes-Einstein equation 2.62, which relates the diffusion coefficient to the temperature and viscosity to obtain equation 2.63, with k_B Is the Boltzmann constant and r as the radius of the spherical particle diffusing through the medium.

$$\mu D_{H_2} = \frac{k_B T}{6\pi r} \tag{2.62}$$

$$\frac{\Phi_{H_2}^{Darcy}}{\Phi_{H_2}^{diff}} = \frac{6\pi r K^{perm}}{k_B T}\Delta P \tag{2.63}$$

Even though the first term is dependent on temperature, it's influence is only marginal over the AEC temperature range of $20°C$ to $80°C$, as is the dependency on electrolyte composition. For a $30\ wt\%$ KOH solution, and an operating temperature of $80°C$, the fraction of crossover through permeation compared to diffusion can be approximated by equation 2.64 [58].

$$\frac{\Phi_{H_2}^{Darcy}}{\Phi_{H_2}^{diff}} \approx \frac{\Delta P}{0.01} \tag{2.64}$$

It can be observed that a pressure difference over the diaphragm of 0.10 bar would result in approximately 10 times as much hydrogen crossover due to electrolyte permeation than through diffusion. This shows just how important pressure control is in AEC systems.

Mitigation techniques

It is clear to see that in order for high pressure/high temperature systems to operate safely, measures have to be taken to reduce crossover, or reduce hydrogen content in the anodic half-cell [70]. In literature multiple methods are suggested aiming at either reducing the risk due to crossover, or at actually reducing crossover itself. The latter methods are preferred as adding technology to reduce risk due to crossover doesn't actually reduce crossover itself and therefor does not particularly aid to hydrogen production rate efficiency. Besides this, it also further complicates an already relatively complicated system. Therefor, only crossover reduction methods will be discussed.

As operating at low current densities has quite a substantial effect on gas crossover, opting to run the system at certain predetermined load provides a cost effective way keep crossover at acceptable levels. This does however require research in order to find the optimum current density, as it is influenced by system specific characteristics such as cell geometry. Current density versus crossover plots such as figure 2.19 provide a clear overview, revealing this sweet spot in current density with respect to crossover [61]. Of course there could be multiple factors influencing the selection of the optimal current density, such as desired production rate, efficiency etc, which have to be taken into account. Partial system operation provides a solution in preventing continuous operation at sub-optimal current densities [10]. Dividing the overall system in several smaller sections, i.e. more smaller cells instead of one larger surface area cell, enables operation at a desired current density, without the maximal load

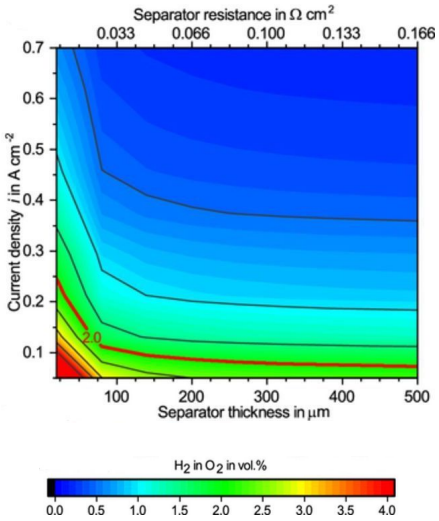

Figure 2.20: Hydrogen crossover: diaphragm thickness versus current density. Adapted from Trinke et al. [70]

limitation of a single cell small surface area system.

While the focus in recent publications for gas crossover in PEM electrolysers is mostly on the influence of current density, for AEC systems the focus tends to be more towards the influence of diaphragm material and process conditions [70].

It is easily conceivable that with increased diaphragm thickness comes less crossover, as can be seen in figure 2.20 [70]. There are however some drawbacks to this solution. As figure 2.20 also shows, with increased diaphragm thickness comes an increase in the diaphragm resistance, resulting in greater ohmic resistance and in turn a decrease in performance of the system. Besides this, as crossover through the diaphragm is secondary to other sources of crossover, the gains by implementing a thicker diaphragm are not substantial. Therefor, this solution is not often considered in literature. On the other hand, as typical Zirfon diaphragms have a thickness of $500\,\mu m$, there is room for improvement when it comes to lowering the diaphragm resistance. Lowering the diaphragm thickness till a thickness of $200\,\mu m$ will have close to no effect on crossover through the diaphragm itself as can be seen in figure 2.20, even though ohmic losses would then be lower. This would however require complex pressure control to ensure the pressure difference does not jeopardize the mechanical stability of the diaphragm [70].
Literature is quite conclusive when it comes to advanced diaphragm materials. As the diffusional flux is already relatively low due to low solubility of hydrogen and oxygen in highly concentrated electrolyte, there is little research going on in this area with respect to reducing crossover [70]. The continues pursuit of lower diaphragm resistance is however an incentive to investigate new diaphragm materials.

As explained previously pressure differences, over the diaphragm could not only jeopardize mechanical stability of the diaphragm but also contribute significantly to crossover. Advanced pressure regulation is an option, but these systems can get complicated rather quickly and consequences can be severe in case of failure. There are simple and low cost solutions conceivable to address the minimization of the pressure difference, like a pressure equalization tube adopted by ZEF. This does however mean that both sides of the system are connected which introduces another route for crossover, perhaps not to dissimilar from when electrolyte cycles are mixed. A more detailed description of such system configuration will follow.

Matsushima et al. showed that applying an external magnetic field influences supersaturation at the electrode surfaces [44]. What can be seen in figure 2.21a is that when no external field is applied, the supersaturation increases roughly linear. Yet when under the influence of an induced magnetic field supersaturation lowers by a significant amount for current densities larger than $10\ mA/cm^2$. This decrease in supersaturation is a result of the extra magnetohydrodynamic (MHD) convection, flushing

out the supersaturation layer on the electrode surface.

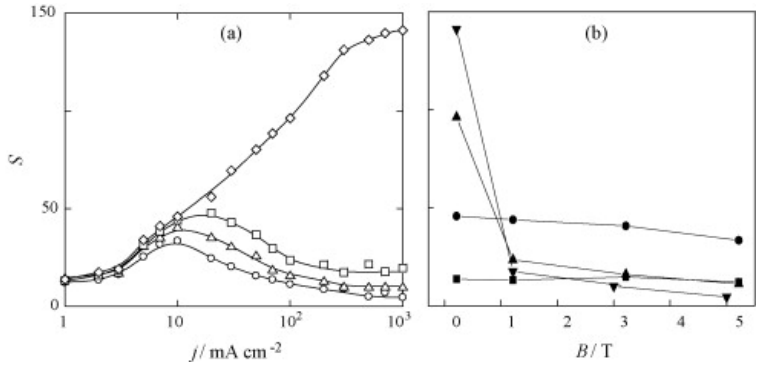

Figure 2.21: Supersaturation S of dissolved hydrogen gas on AEC cathode surface at 60°C and 30 wt% KOH aqueous solution, (a) as function of current density and (b) as function of magnetic field strength. In (a), magnetic field strength B: diamonds; 0 T, squares; 1 T, triangles; 3 T, circles; 5 T and in (b), current density i: black squares; $1\ mA/cm^2$, black dots; $10\ mA/cm^2$, black triangles; $100\ mA/cm^2$, black inverted triangles; $1000\ mA/cm^2$. Adapted from Matsushima et al. [44]

Other external fields, such as ultrasound and high gravity, aimed at lowering energy consumption by reducing bubble coverage on the electrode are also believed to reduce supersaturated zones, and thus reducing crossover [70]. Further research is however required to quantify these effects.

As electrolyte mixing is considered responsible for the larger part of all crossed over gas, it is here that substantial gains can be achieved. Several solutions are proposed in literature [24][61].
One of the solutions is complete separation of electrolyte cycles, which will eliminate the possibility for gas crossover via this route[70]. If the main source of crossover in alkaline electrolysis is indeed electrolyte mixing, it is reasonable to assume that concentration gradients across the diaphragm, as in equations 2.44 and 2.45 can be simplified to 2.65 and 2.66 when electrolyte cycles are separated. This is because the concentration of crossed over species becomes negligible compared to concentrations at designated side [70].

$$\Delta c_{O_2} \approx c_{O_2}^{an} - \cancelto{0}{c_{O_2}^{cat}} \tag{2.65}$$

$$\Delta c_{H_2} \approx c_{H_2}^{cat} - \cancelto{0}{c_{H_2}^{an}} \tag{2.66}$$

Although separating electrolyte cycles will aid product purity substantially as Trinke et al. showed in figures 2.16 and 2.18, an electrolyte concentration difference will develop with time over the two half-cells. As mentioned before, ionic conductivity of electrolyte is strongly influenced by electrolyte concentration. Consequently, this will eventually lead to higher ionic resistances and thus lower efficiency [70].
To omit the need for an electrolyte concentration control system, several solutions presented in literature yield dynamic/advanced electrolyte mixing/cycling schemes. What is desired in this case, is an electrolyte scheme which separates cycles when gas impurity is relatively high, i.e. when the safety limit is exceeded, and enables mixing again when impurities are at an acceptable level[10]. What is elegant to this solution is that when the safety limit is most likely at risk, operation is at low current densities as fraction of crossed over gas compared to product gas is larger. At this point production itself is comparably low. This means the electrolyte concentration difference mentioned before is not as fast to develop as when electrolyte cycles are separated at higher current densities. The point upon which switching between mixed and separate cycles is AEC system specific, and could either be investigated beforehand, or close to real-time with continuous gas measurements. This means either predictive control or feedback control is possible.
Brauns et al. investigated the effect of periodic switching between mixed and separated cycles. This method is less complicated/advanced, yet they measured a decrease of the average anodic hydrogen content of $0.258\ vol\%$ at a current density of $1000\ mA/cm^2$[24]. This procedure will of course lead to oscillating crossed over gas concentrations, but Haug et al. found that changing the frequency of

opening and closing of separation valve only influences the amplitude of the oscillations, while the average measured value remained to the same [24].
Schug et al. among other researchers opted to reduce crossover due to electrolyte mixing by reducing electrolyte flow as much as possible, i.e. reducing the electrolyte recirculation rate [61][70]. The limit to this reduction in flow is presented by another electrolyte flow duty; the transportation of heat. When ohmic losses due to heat generation reached a certain maximum, the flow would be enlarged again. The result of Schug's work can be observed in figure 2.19, where impurities are within safety limit for the entire tested current density range of $100 - 1200\ mA/cm^2$. It must be noted that this solution is only possible when there is forced electrolyte flow, i.e. irrelevant for convective flow systems, and that with less flow bubble coverage of the electrodes might go up, which in turn means an increase of cell voltage and thus a decrease in efficiency [70]. The optimum electrolyte recirculation rate is therefor dependent on many factors apart from crossover such as cell geometry, electrode surface roughness etc.

2.4. Renewable energy source

Implementation of renewable energy sources in AEC systems is the key in enabling sustainable hydrogen production, and because of that imperative for sustainable hydrocarbon production via the ZEF process. Renewable energy sources such as solar, wind, hydro etc. do however come with their energy source specific challenges. Hereinafter, the scope of renewable energy sources will be narrowed down to solar and wind, as these are present basically all around the world, and are most likely to be used for the purpose intended.

In alkaline water electrolysis advanced power supply control is essential. Brauns et al. reports that periphery of power input signal affects performance and efficiency of the system [10]. It is therefor desired to have a clean power input signal periphery, with minimal ripples. The effects are amplified with decreasing ripple frequency [17]. Speckmann et all. showed that there is a relation between periphery and product gas quality as well, as he found that current ripples cause an increase in oxygen crossover [68]. This poses a challenge for implementation of renewable energy sources, as they are fluctuating by nature.
An advanced rectifier system is therefor imperative, in order to smoothen out the power input signal. With fluctuating sources like wind and solar, the AEC system will have to operate dynamically. For this purpose, transistor based rectifier systems are superior to thyristor based structures, as they enable operation at low load, minimizing full restarts of the system [68].

With the use of renewable energy sources there isn't the luxury of setting the load to an optimal value. The load is now a result of the specific conditions during the day. It's because of this that a flexible, multiple stack/cell system, as mentioned previously, is desired, in order for the system to keep operating within the safety window. The burden of flexibility lies completely on the electrolysers shoulders, as the renewable energy harvesting device should always operate at full potential in order to make the most of the available renewable energy source, whether its wind or solar. What is required is a system that can adjust when there is low energy/power available, shutting down compartments of the multiple stack/multiple cell system, ensuring sufficient levels of current density in the operational cells, accompanied with acceptable product gas purity [10][26][16]. This solution broadens the time frame the system is able to run during the day. This could either be achieved with feedback control, or with predictive control [29].

2.5. Previous work - ZEF

In this section ZEF's efforts in designing an AEC system capable of achieving 35 grams of hydrogen production per 8 hours of operation at 99.9 % purity with 80 % efficiency will be evaluated. These desired specifications are a result of the specific requirements for the subsequent ZEF systems.

2.5.1. Current ZEF cell/stack design

Temperature

In the ZEF AEC system, as there is no controllable heating or cooling system implemented, temperature is an uncontrolled variable. It will however be monitored and logged at 4 places in the system:

- on flash tanks on both sides of the system
- on top of the stack
- on electrolyte flow coming out of the stack, mounted on the ”riser” tubes

The inability to control the temperature introduces some limitations in the system. This will however be taken into account when analyzing experimental data.

3

Experimental set-up and methodology

Now that it is clear which process parameters and design choices influence product gas crossover, in this chapter an experiment plan will be explicated aimed at answering the remaining research questions proposed in section 1.5. This will be followed by an overview on the design and fabrication of the experimental set-up.

3.1. Experimental methodology

The experiment plan is divided in three sections, according to their respective objectives. As mentioned previously, even though temperature is not a controlled variable in the ZEF system it will be monitored and logged during all experiments, and taken into consideration during analysis.

3.1.1. Safe window of operation during steady state

In pursuit of finding the window which allows safe operation of the system, it is helpful to visualize beforehand what this window is expected to look like. According to literature, more crossover occurs at higher pressures. The effect of this is taken into account in our prediction, as can be observed in figure 3.1. What can also be observed is that below a specific current density, the fraction of crossed over gas will be such that no safe operation is possible at any pressure level. This too is observable in figure 3.1. It's important to note, figure 3.1 is merely a prediction on the expected shape of the safety window. The actual shape and data points will follow from the experiments.

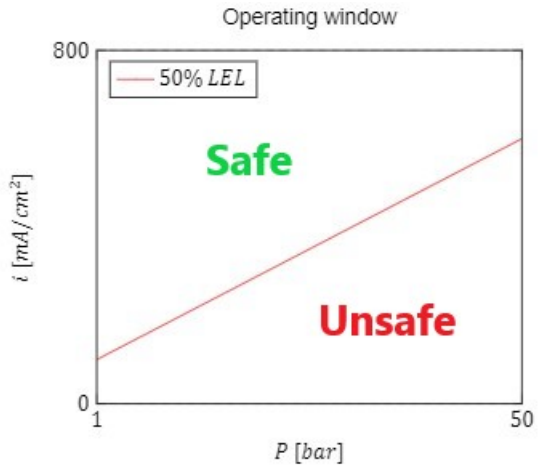

Figure 3.1: Operating window prediction. The window for safe operation is above the red line.

In order to define the safe operating window, experiments at several current density and pressure levels will be conducted.

Experimenting will commence at an operating pressure of 50 bar, as this is the desired ZEF operating pressure. As the current density will be in the range of $0 - 800\ mA/cm^2$, the first experiment will be held at the midpoint of this current density range: $400\ mA/cm^2$. If gas measurements at these parameters indicate safe operation, the follow up test will be at the midpoint between current current density and bottom of the range, so $200\ mA/cm^2$. If this then turns out to be outside the safe operating window, the next test will be held at midpoint of previous two current densities: $300\ mA/cm^2$. This will be done at least 6 times, as this will provide a $1/64$ times original range window where the boundary between safe and unsafe operation must lie. After these 6 times, 2 more experiments around this point will be done to improve uncertainty, and enable to predict measurement noise.

For the next run of experiments at an operating pressure of 40 bar, the current density will range between the acquired boundary at 50 bar and 0, as the boundary at 40 bar is expected to lie below this value. This is done as the final $1/64$ times original range window will be even smaller than in the previous experiment runs.

The method presented will be executed for operating pressures of 30, 20 and 15 bar. The duration of the experiments will vary for different current densities, as gas evolution rates are lower for lower current densities according to the Faraday's law. Calculations indicate experiment duration ranges from 2 to 8 hours of operation. For each experiment the system will run until gas measurements indicate both production gas buffers are completely flushed with gas composition flowing out of the stack.

The production of labor of these experiments will be a quantified operating window for safe operations for the current ZEF AEC system, as well as insight into whether or not a standby mode is required during downtime of the system. And if so, it will bring forth knowledge on what should be the current density in this standby mode.

3.1.2. Effect of crossover during particular modes of operation: start-up, standby and steady-state

As the system will be powered by solar power, the AEC system will most probably start-up and shutdown (at least) once a day, and remain in standby mode for most of the time. Knowledge on gas crossover during these modes of operation is therefor imperative for safe operation of the AEC system. During shutdown of the system evolution of evolving species will cease. Yet, crossover due to diffusion continues to take place the entire time the system is down. As a result, as time goes on the concentration of crossed-over gas increases on the foreign side. This means the concentration gradient over diaphragm will slowly decreases, slowing down the flux of crossover species, but only when sufficient gas has diffused through the separator. The consequence of this phenomena is that upon restart of the system a spike in crossed-over gas concentration is expected in the buffers, as saturated electrolyte starts flowing from stack to the flash tanks. The models of Schwarze and Daniil both predict fractionally more crossover at lower current densities, and thus these spikes as well [63][13]. Gas measurements will be taken during start-up and in standby modes, to give insight in crossover during these modes of operation, as well as in the validity of the models.

3.1.3. Effect of pressure equalization tube on crossover

As ZEF CEO Jan van Kranendonk hypothesizes that crossover in the pressure equalization tube (PET) only happens due to diffusion and not through convection, it would interesting to see how variations of this pressure equalization tube affect crossover levels in the system. In an endeavor to quantify the effect of the PET on crossover, a series of experiments will be conducted under equal operating conditions, apart from varying the geometry of the pressure equalization tube.

3.2. Experimental set-up

3.2.1. Gas purity measurement system

In order to be able say anything about gas crossover/purity, a gas measurement system has to be implemented in the alkaline electrolyser system. What complicates the system installation, is that the AEC system is mounted inside a bunker. This bunker acts as a safety barrier, and provides a safe working environment. It opens the opportunity to conduct experiments, as product gasses, which are produced under high pressure, can be highly explosive when mixed. This does however come with its challenges as space inside the bunker is limited. This, along with several other factors make up the system requirements.

Gas purity measurement system requirements
The sensor system has to meet the following requirements:

- The cathode-side sensor must be able to measure traces of oxygen in the range of 0-$1\ vol\%$, or 0-$10^4\ ppm$.
- The anode-side sensor must be able to measure traces of hydrogen in the range of 0-100% of LEL, or 0 to $4 \cdot 10^4\ ppm$.
- Both sensors should measure with a resolution of $100\ ppm$ or better, to ensure differences in crossover can be detected at the slightest change of current densities, especially important for low current densities.
- The systems must be able to do measurements on incoming gas samples with a pressure of up to 50 bar.
- The proportions of both systems must be such that they fit inside the existing bunker set-up.

Sourcing
After a thorough search, sensors from a company called Evikon proved to be the best option. They are relatively low-cost, and small in size compared to others. Specifics on these sensors can be seen in table 3.1, while complete data sheets can be found in appendix A.3.

Target gas	Product code	Type of sensor	Detection range	Measuring resolution	Accuracy	Response time	Operating pressure	Temperature range
H_2	E2618-H2-E-RP33-3-24VDC	Electrochemical cell sensor	0-100% LEL, 0-40000 ppm	0.1% LEL, 40 ppm	±2% LEL, ±800 ppm	<10 seconds	0.9-1.1 bar	-30 C - +50 C
O_2	E2618-O2-L-RP33-3-24VDC	Optical sensor	0-25%	0.01 vol%, 100 ppm	-	<30 seconds	0.9-1.1 bar	-30 C - +60 C

Table 3.1: Evikon sensor specifications.

As can be seen from table 3.1, the sensors meet most of the requirements, apart from the operating pressure. The sensors can't be exposed to pressures above 1.1 bar, and as a consequence cannot be placed directly in the outgoing product gas flow. To mitigate this problem, gas samples will first be led through a needle valve, which acts as a throttle valve. The needle valves enable regulation of mass flow when solenoid valves connecting gas measurement system to AEC system are opened. The sensors will then be placed in separate sensor housings equipped with additional pressure relief valves.

Figure 3.2 shows one of the sensor probes with transmitter unit. What's imperative about the electrochemical cell anodic hydrogen content sensor is that it is not affected by a pure oxygen environment. Evikon does specify that the sensor must be placed in a dry environment, and come with moisture filters on the probes from the factory for extra protection.

Figure 3.2: Evikon sensor probe with sensor transmitter

Sensor system design
In order to be able to provide gas samples to the Evikon sensors under the right conditions, the process flow diagram in figure 3.3 is utilized to properly design the system.

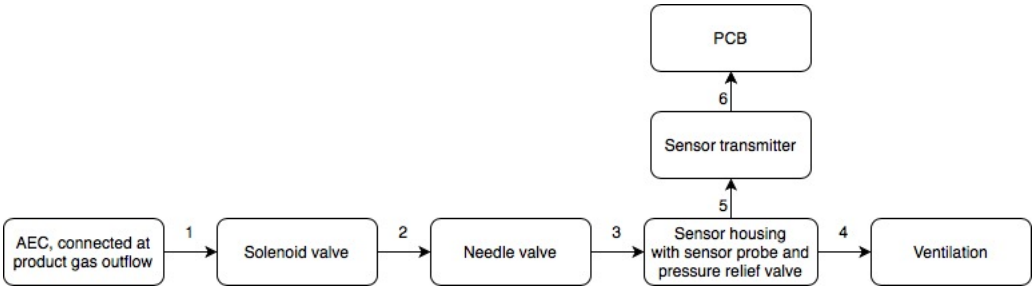

Figure 3.3: Gas measurement system process flow diagram. Lines 1-4: gas flows, lines 5-6: electrical signals

For the pressure relief valves of the sensor housing, multiple options have been evaluated. Eventually it was opted to go for umbrella valves from a company called Minivalve International B.V., as they are very simple in design, cost-effective, easy to install and open at any pressures above 1 bar. A schematic of such an umbrella valve can be observed in figure 3.4. For technical drawing including valve seat details see appendix A.4.

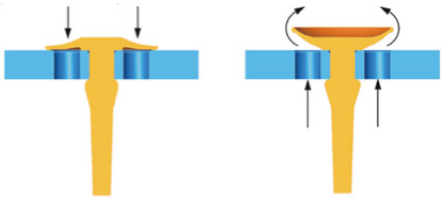

Figure 3.4: Schematic of umbrella valve, by Minivalve International B.V.

In order to make it clear where the gas measurement systems will be implemented in the bunker AEC set-up, the process flow diagrams of both measurement systems are added to the bunker set-up process flow diagram. This can be observed in figure 3.5.

Figure 3.5: Bunker set-up process flow diagram, including gas measurement system.

What figure 3.5 doesn't show however, is that the entire set-up has to fit through the top opening of the bunker, all within a diameter of 30 cm.
For this reason, the sensor housings have been designed to take up minimal space within the bunker, and will be fitted vertically to minimize their footprint. Another benefit of the small size sensor housings is that gas sample volume is minimized, which means flushing and refreshing of gas samples in the housings is dealt with relatively fast. An exploded view of the sensor housing can be observed in figure 3.6a.
From right to left, the individual parts are:

- The sensor probe, included in the image for sense of scale.
- Gas sensor house top part. It is here that the sensor probe rests in, and where the gas samples enter via Swagelok flexitube through the top hole, just above the probe. It is specifically designed this way, such that the incoming flow can not directly exert pressure on the sensor surface.
- Umbrella valve seating disc. This part has been designed with seating specifications supplied by Minivalve International B.V. The reason for this disc to be separate is to enable access to the sensor from inside the housing.
- Sensor housing fume hood. This part is the final stage of the sensor housing, catching the gas as it flows through the umbrella valve. It then directs the gas towards the bunker ventilation, as they are connected by Swagelok flexitubes.

The housings cylindrical design ensures a close fit around the sensor probes, and enables fabrication by lathe machine. The housings will be fabricated from polyvinyl chloride (PVC).

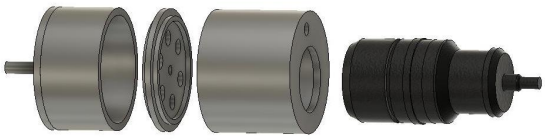

(a) Sensor housing including sensor probe - exploded view

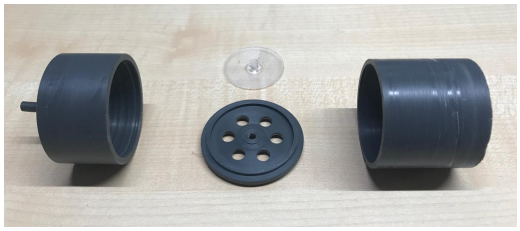

(b) PVC sensor housing including umbrella valve

Figure 3.7 shows a component overview of the gas measurement system. The gas measurement system components are identical for the hydrogen and oxygen side of the system, apart from their respective sensors.

Figure 3.7: Gas measurement system component overview

Control scheme alteration
As more gas measurement data could lead to more knowledge on crossover, it is desired to purge as little product gas as possible through the general purge valves, and run most if not all product gas through the gas measurement system. The control scheme is therefor altered to actuate the gas measurement valves when previously the purge valves would have been actuated, allowing for near continuous gas measurement. The hydrogen side gas measurement valve, GMV2 in figure 3.8, will therefor be actuated by pressure control, and the oxygen side gas measurement valve, GMV1 in figure 3.8, will be actuated by level control. The purge valves PV1 and PV2 are however not obsolete, as they still provide a safety mechanism. They make it possible to reduce the pressure much faster than purging solely through the gas measurement system would, should this be required. Hydrogen side purge valve PV2 is still actuated by control, but now only when the pressure exceeds control pressure by 0.5 bar.

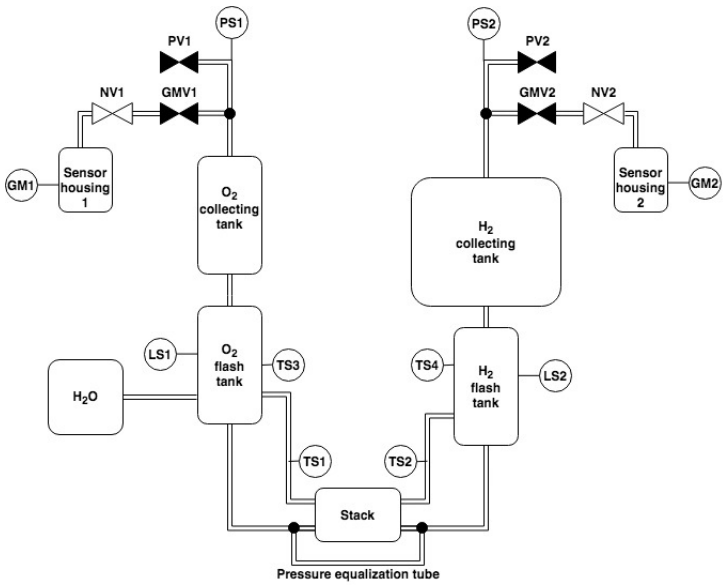

Figure 3.8: Schematic of ZEF AEC system with gas measurement system

Pressure equalization tube configurations
As mentioned in section 2.3.4, electrolyte mixing plays a substantial role in gas crossover. In the ZEF AEC system electrolyte cycles are not deliberately mixed before reentering the cells. Yet, mixing of electrolyte might still occur, as the sides of the system are connected via the pressure equalization tube as illustrated in figure 3.8.

When the valves are closed, due to the geometry of the system there is a net flow of (possibly saturated) electrolyte towards the hydrogen side, aiding O_2 crossover.
During valve opening electrolyte flows towards the side at which gas is released from the system. Valve opening duration, tuning of needle valves and operating temperature and pressure all influence how much volume of gas is released per opening. If this volume of gas is the same or larger order of magnitude as the volume of liquid in the pressure equalization tube, electrolyte saturated with product gas is able to reach the other side of the system, possibly increasing crossover significantly.

The current pressure equalization tube is a $6\ mm$ outside diameter Swagelok tube ($4\ mm$ inside diameter) of approximately $20\ cm$ in length, yielding an inside volume of $2.5\ cm^3$. From hereon, the configuration with this pressure equalization tube will be referred to as configuration A.
To investigate the contribution of the current pressure equalization tube, two more configurations will be tested:

- Configuration B: a $12\ mm$ outside diameter Swagelok tube ($10\ mm$ inside diameter), $80\ cm$ in length, yielding an inside volume of $62.8\,cm^3$: 25 times larger than the current pressure equalization tube. This tube is depicted in figure 3.9a.

- Configuration C: a $35\ mm$ inside diameter tri-clamp tube, approximately $24\ cm$ in length, yielding an inside volume of $230.9\ cm^3$: 3.7 times larger than configuration B, and over 90 times larger than configuration A pressure equalization tubes. This tube is depicted in figure 3.9b.

Configurations B and C will ensure flow due to valve opening is purely oscillatory, and will prohibit flushing the entire volume of the pressure equalization tube with electrolyte from one side of the system during valve opening.

(a) Configuration B: $62.8\ cm^3$ inside volume

(b) Configuration C: $230.9\ cm^3$ inside volume

Figure 3.9: Pressure equalization tubes

4

Results & Discussion

In this chapter the results of this research will be presented. Firstly, characterization of the ZEF electrolyser system and the gas measurement system will be done, after which the product gas crossover results will be presented and discussed, including a comparison between simulation and real life.

4.1. Characterization of systems

4.1.1. ZEF electrolyser

In this section characterization of the ZEF electrolyser will be done with respect to efficiency, electrolyte levels and temperature and pressure response.

Efficiency

The ZEF control scheme, as explained in section 2.5.1, directly influences the latter three character traits, and therefor indirectly the efficiency as well.

Table 4.1 provides an overview of the Faradaic efficiency of the ZEF AEC system for different current densities. The equilibrium potential used to calculate the Faradaic efficiencies has been calculated with equation 4.1 with T in Kelvin, under the assumption it depends linearly on temperature for the AEC temperature range. This assumption is reasonable according to literature, as the Gibbs free energy of formation depends linearly on temperature, figure 2.3 [77]. Equation 4.1 has been acquired based on U_{rev} values reported in literature [55].

$$U_{rev} = -5.8 \cdot 10^{-4} T + 1.48484 \tag{4.1}$$

As the equilibrium potential is dependent on temperature and pressure, and temperature being an uncontrollable variable dependent on current density, representing efficiency primarily as Faradaic

Current density [mA/cm²]	Temperature steady-state with cooling [$^{\circ}C$]	$\eta^{eff}_{Faradaic}$ with cooling	Temperature steady-state without cooling [$^{\circ}C$]	$\eta^{eff}_{Faradaic}$ without cooling
100	37	64.5%* (66.3%)	58	65.0%** (66.9%)
150	46	64.6%	73	63.6%** (65.4%)
200	56	62.3%	-	-
250	64	61.0%	-	-
300	73	62.4%	-	-
350	77	61.7%	-	-

Table 4.1: Faradaic efficiency of non-zero-gap stack, with and without cooling, at steady-state. All experiments where conducted at an operating pressure of 50 bar, with sandblasted nickel electrodes except for *: without sandblasted electrode and **: at 30 bar operating pressure (and also without sandblasted electrode). Value between parentheses is the corrected value for the gain in efficiency due to sandblasting, based on the data.

Current density [mA/cm²]	Temperature steady-state with cooling [$^{\circ}C$]	$\eta^{eff}_{thermal}$ with cooling	Temperature steady-state without cooling [$^{\circ}C$]	$\eta^{eff}_{thermal}$ without cooling
100	37	73.1%* (75.2%)	58	74.5%** (74.8%)
150	46	73.5%	73	73.3%** (74.1%)
200	56	71.5%	-	-
250	64	70.1%	-	-
300	73	72.2%	-	-
350	77	71.1%	-	-

Table 4.2: Thermal efficiency of non-zero-gap stack, with and without cooling, at steady-state. All experiments where conducted at an operating pressure of 50 bar with sandblasted nickel electrodes except for *: without sandblasted electrode and **: at 30 bar operating pressure. Value between parentheses is the corrected value based on the data.

efficiency provides a somewhat obstructed view on the influence of for instance current density on efficiency. As can be seen in figure 2.3, the thermoneutral voltage dependency on temperature is negligible, as is its dependency on pressure for the ZEF temperature and pressure range [55]. Representing the efficiency with the thermal efficiency could therefor be helpful in showing the effect of current density, as well as the effect of temperature with respect to cell resistance on the efficiency of the system. Table 4.2 provides an overview of the thermal efficiency of the system for the measured current densities, with the thermoneutral voltage taken at $1.48\,V$.

What can be observed from tables 4.1 and 4.2 is that from 100 to $250\,mA/cm^2$, the effect of increasing current density, and with that the applied voltage, decreases efficiency as mentioned in section 2.1.4. Yet, as temperature is dependent on the current flowing through the cell, at a current density of $300\ mA/cm^2$ temperature seems to have risen sufficiently for its benefits to become dominant. The decrease in overpotentials for both HER and OER combined with an increase in electrolyte conductivity overcome the effect of increased bubble coverage at higher temp, as well as an increase in void fraction due to higher production. When looking at Ohm's law, equation 2.16, if temperature would remain constant increasing the current density would be accompanied by an increase in ohmic resistance due to increased production resulting in an increase in void fraction, which means the applied voltage would go up even more. Yet, if temperature is not constant, like in the ZEF AEC system, as the current density is increased the temperature increases, lowering the cell resistance due to the increase in electrolyte conductivity as well as lower reaction overpotentials. The net result could lead to a lower applied voltage, which is seemingly the case at a current density of $300\ mA/cm^2$. Cell temperature, and with that temperature control, therefor play a key role in maximizing efficiency.

Kleist et al. showed that increasing pressure decreases void fraction, which theoretically leads to a decrease in resistance of the electrolyte [31]. From experiments it is concluded that this only holds when production is sufficiently high. For low current densities, the opposite effect was observed at elevated pressure: for current densities of 100 and $150\ mA/cm^2$ the thermal efficiency at steady-state decreased by 2.7% and 2.0% respectively when the pressure was increased from 20 to 50 bar (at equal steady-state temperature). Yet, at a current density of $200\,mA/cm^2$ increasing the pressure from 30 to 50 bar meant thermal efficiency was increased by 1.5%. And even though the conductance of anions through a solvent is dependent on pressure, its dependency is assumed negligible in the measured pressure range, ruling this out as a possible explanation [37]. It could be that at low gas production, the decrease in bubble size due to increased pressure lowers the buoyancy force on the bubbles as their density is comparably high. As the flow in the ZEF AEC system is natural convectively driven, this decrease in buoyancy could decrease bubble detachment, and with that increase coverage of the electrode surfaces resulting in increased resistance. This is however a hypotheses, and further research is required to mark this as the cause for the observed behaviour.

As mentioned in section 2.1.1 surface morphology of the electrodes has a major effect on reaction kinetics. Rougher surfaces have a larger effective electrode surface area, with more active sites for bubble nucleation. The ZEF stack uses nickel bipolar plates as electrodes, which yield a smooth and shiny surface when they were supplied. For comparison sake, half of the experiments were conducted

with the smooth surfaced nickel electrodes, while for the remainder of the experiments the surface was roughened up by blasting them with sand for approximately 5 seconds. The difference in surface finish is clearly visible in figure 4.1. An untreated cell disc is visible on the left, while a sandblasted example is visible on the right.

Figure 4.1: Untreated cell disc on the left, cell disc with sandblasted nickel bipolar plate/electrode on the right

An increase in performance was observed in line with literature, as predicted in section 2.3.1. The sandblasted electrodes decreased cell potential by $0.06\,V$ at equal current density, operating pressure and temperature, which meant an increase in thermal efficiency of 2%. This is about 50% the performance gain presented by Colli et al. when porous nickel was compared to plain nickel electrodes, figures 2.7 and 2.8 [11]. This seems reasonable, as sandblasted nickel is still far from porous.

What is interesting to note is that for low current densities increasing the temperature did not directly lead to an increase in thermal efficiency. In fact, at $100\,mA/cm^2$ a decrease of 0.4% was deduced from the data. Although it's hard to tell with certainty, it could be that when gas production is low the effect of temperature on lowering reaction overpotentials, causing increased bubble coverage is more substantial than its effect on electrolyte conductivity. Low gas production is in fact accompanied with less strong convection driven flow of electrolyte, as this is directly proportional to the amount of bubbles in the system. This could have a strong influence on bubble detachment, which in turn has an influence on bubble resistance. Combine this with Wang et al. observations of increased bubble coverage at elevated temperatures, to yield this as a plausible explanation for the observed behaviour [75].

Figure 4.2 shows development of the thermal efficiency during an experiment. If we compare with figure 4.5, we see that the initial sharp rise in system temperature is followed by the thermal efficiency. It does appear that thermal efficiency reaches within range of its final value a little sooner compared to system temperature, as steady-state value is reached long before steady-state temperature is reached at the red dashed line. This could indicate that the relative gain in efficiency for the temperature rise between 20-$55°C$ is more substantial than for the 55-$65°C$. Measurement noise does however make it difficult to deduce exact dependency of thermal efficiency on temperature.

Pressure
As the stack contains 16 cells, pressure builds up quickly compared to previous ZEF electrolysers. At ambient starting conditions and a current density of $300\ mA/cm^2$ an operating pressure of 50 bar is reached in approximately 680 seconds, as can be observed in figure 4.3. When the system remained under pressure, control pressure is consistently reached in under 60 seconds. From this moment on, pressure is maintained by actuation of both the hydrogen side gas measurement system by pressure control, and the oxygen side gas measurement system by level control. The drop in pressure upon

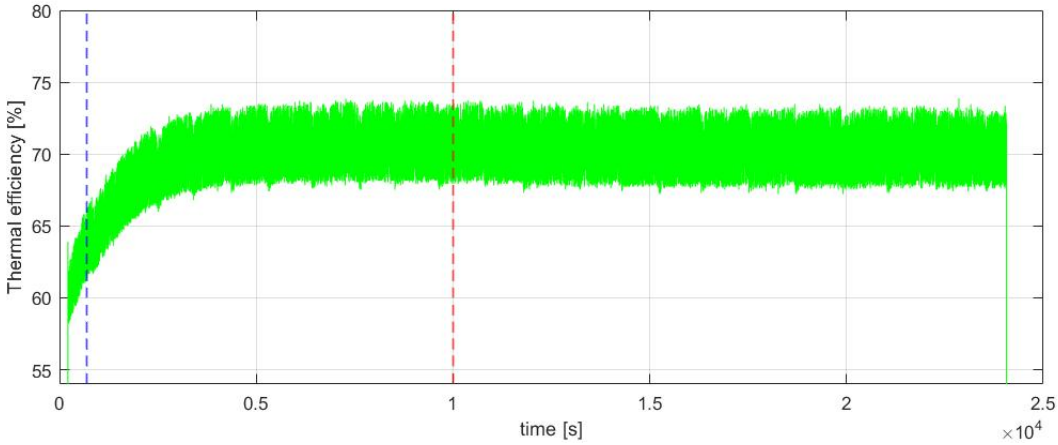

Figure 4.2: Thermal efficiency vs time - current density: $300\ mA/cm^2$ operating pressure: 50 bar. Dashed lines indicate: control pressure reached (blue), 95% steady-state temperature reached (red)

opening of the gas measurement valve is what causes the ”widening” of the pressure line, which is highlighted in figure 4.3. The magnitude of this drop in pressure is dependent on throttle device tuning. This will be elaborated later on among other pressure character traits related to actuation of the valves.

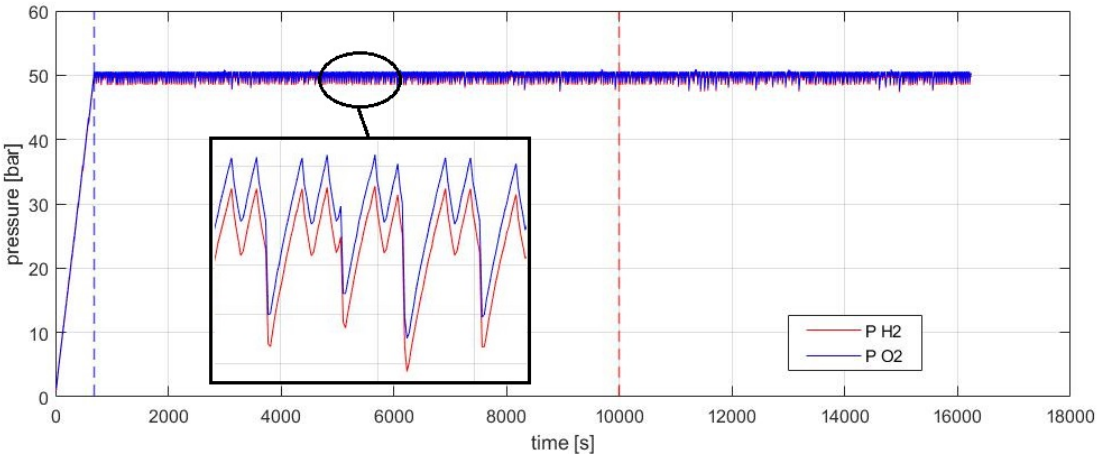

Figure 4.3: Pressure vs time - current density: $300\ mA/cm^2$ operating pressure: 50 bar. The highlighted section shows pressure drop upon actuation of hydrogen side gas measurement system by pressure control is smaller than pressure drop upon actuation of oxygen side gas measurement system by level control. Dashed lines indicate: control pressure reached (blue), 95% steady-state temperature reached (red)

Temperature

In the early stages of testing it became apparent that the lack of cooling in the system hindered testing at current densities greater than $200\ mA/cm^2$. At this current density electrolyte temperature flowing out of the stack rose to $80°C$, before reaching steady state. Although the cell material PSU has a glass temperature of $187°C$, the temperature limit imposed by ZEF of the electrolyte flowing out of the stack had been set at $80°C$, as temperatures inside the stack will be slightly higher than measured at the outflows [2]. In order to enlarge the experimental space, two 12V cross flow fans, depicted in figure 4.4, were installed in the bunker setup to create an airflow and increase cooling by forced convection. It must be noted that these fans were not controllable in the current system, which means temperature remains an uncontrollable variable. It does however raise the limit in terms of current density to $350\ mA/cm^2$.

Figure 4.4: 12V cross flow fans installed in bunker setup.

Figure 4.5 shows a typical temperature gradient over the course a single experiment, which would last approximately 7 hours.

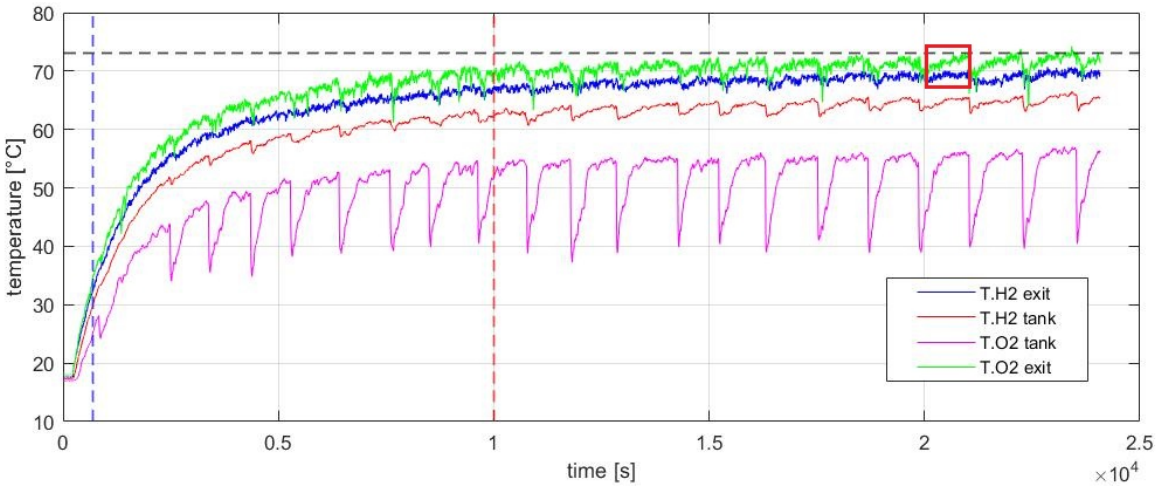

Figure 4.5: Temperature vs time - current density: $300\ mA/cm^2$ operating pressure: 50 bar. Dashed lines indicate: control pressure reached (blue), 95% steady-state temperature reached (red), steady-state temperature (black). Red rectangle is highlighted in figure 4.6

What can be seen in figure 4.5 is that temperature behaves as an upward exponential decay, until at steady state the amount of heat generated by Joule heating is equal to cooling by primarily convection. It can be observed that the rise time (10% to 90%) is approximately 5600 seconds, and that temperature reaches 95% of the equilibrium temperature in approximately $1 \cdot 10^4$ seconds at $300\ mA/cm^2$, but this is of course current density specific. For comparison sake, for a current density of $100\ mA/cm^2$ the equilibrium temperature was reached in $1.4 \cdot 10^4$ seconds.
What can be observed is that the electrolyte/product gas mixture cools down quite significantly when flowing from stack to the flash tanks, as flash tank temperatures on both sides of the system (pink and red lines) are significantly lower than stack out electrolyte temperatures (green and blue lines). There is also a difference in temperature between both flash tanks, which is explainable by the placement of the temperature sensors themselves. The hydrogen side flash tank temperature sensor is placed between the fan and the tank itself. The tape used to mount the sensor acts as an insulating shield

for the convective flow, which limits cooling and thus the hydrogen side flash tank remains at a higher temperature. The temperature sensor on the oxygen side flash tank was mounted opposite to the fan, so in this case the bare flash tank was exposed to the flow of wind coming from the fan.
As water is replenished in the oxygen side flash tank, this temperature is most responsive to this procedure. The downward spikes in pink in figure 4.5 show very clearly when water at ambient temperature was added to the system.

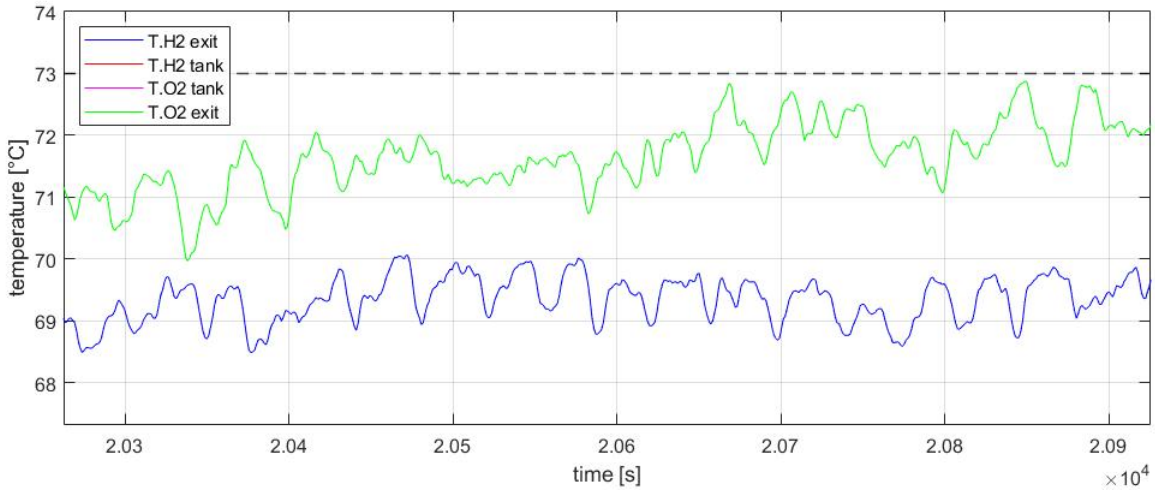

Figure 4.6: Red rectangle in figure 4.5 highlighted: stack out electrolyte temperatures. Fluctuations are believed to be the result of flow stagnation - current density: $300\ mA/cm^2$ operating pressure: 50 bar

Flow stagnation
The red rectangle in figure 4.5 is highlighted in figure 4.6, where it can be observed that there is a significant amount of ”noise” in the temperature of the electrolyte flowing from the stack. These fluctuations are believed to be a result of flow stagnation, a phenomena which was observed and filmed by Kleist et al. [31]. Bubbles clump together to form a larger bubble in front of the exit channels, upon which surface tension prohibits it from exiting the cells and stagnating the flow in the riser tubes. As a result, temperature in the riser tubes drops as forced convection on the outside cools them down.
When comparing figures 4.6 and 4.7 it can be observed that flow stagnation happens less at higher current density, as increased production is able to increase buoyancy force of the trapped bubble faster, ”forcing” it out of the cell in shorter amount of time. Due to similar reasons, this phenomena was more frequently observed on the oxygen side of the system. As can be observed in figure 4.7 the oxygen side experienced flow stagnation of longer duration compared to the hydrogen side, which could again be attributed to the difference in gas production rate compared to the hydrogen side. The duration of flow stagnation on the oxygen side was of such length, that it could also be observed as fluctuations in the oxygen side flash tank temperature.
What is interesting to mention is that flow stagnation really seems to become substantial from the moment control pressure is reached, i.e. when the hydrogen side gas measurement/purge valve is first actuated.

4.1.2. Gas measurement system

The gas measurement system yielded the following characteristics:

- As the gas measurement sensors are specified to operate at atmospheric pressure, the flows that leave the system are throttled with needle valves before they enter the sensor housings, as explained in section 3.2.1. These throttling devices (needle valves) have been tuned manually when the system was pressure tested with N_2. The hydrogen side throttling device is more finely tuned than the oxygen side, as H_2 flows relatively easy and fast compared to O_2 as it is a smaller and lighter molecule. With the current tuning, the hydrogen side gas measurement valve opens

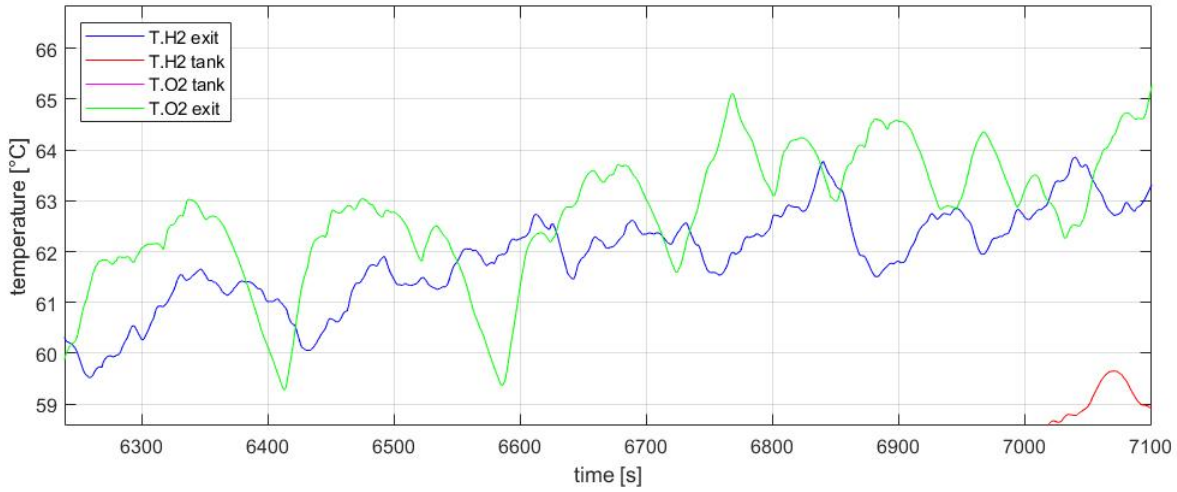

Figure 4.7: Stack out electrolyte temperatures for lower current density compared to figure 4.6. It can be observed that stagnation period is longer, and thus fluctuations which are believed to be the result of flow stagnation are of larger magnitude. It can also clearly be seen that temperature fluctuations O_2 side electrolyte stack out temperature are larger compared to H_2 side, indicating flow to be stagnating for longer periods on the O_2 side - current density: $150\ mA/cm^2$ operating pressure: 50 bar

for $5000\ ms$, while the oxygen side gas measurement valve opens for $1300\ ms$ each time they are actuated.

- The nature of the control scheme means that hydrogen side gas measurement starts when control pressure is reached. This introduces complications which will be explained later on.

- Oxygen side gas measurement is actuated by level control, which in practice means this side always performs gas measurement before hydrogen side measurement commences.

- The gas sensors produce values in real time. Yet, the gas measurement system valves are only open for a set duration of time each time they are actuated by control. This discrepancy comes with several consequences. For one, concentration course graphs of the system for the duration of a single experiment, like figures 4.15 and 4.16, provide knowledge on the course of gas concentration during that experiment, as well as on the order of magnitude. For the exact values of gas composition other factors have to be taken into account.

- When the system is off during nighttime the gases in the sensor housings are striving for equilibrium with their surroundings. During long off time this equilibrium is in fact reached, such that the composition of the contents of the sensor housing resemble that of the ambient air. This means that when the system is started-up and gas measurements system valves are first being actuated, the housings will have to be flushed of their contents, with gas coming from the system. It's only when they are completely flushed that readings become somewhat accurate.

- During operation when the valves are closed, the gases in the sensor housing are still striving for equilibrium with their surroundings. This means that when the oxygen side gas measurement valve is closed, the crossed-over hydrogen which we're trying to measure diffuses out of the sensor housing as the hydrogen concentration of surrounding air is lower (practically zero). This "escaping" of H_2 gas lowers the concentration of H_2 in the sensor housing. This means that in order to get the exact magnitude of concentration of crossed-over gas the housing must not only be flushed completely, values must be taken from right before the gas measurement valve shuts again. The data in the graph must therefor also be interpreted in the following manner. For the crossed-over H_2 concentration, the values that closest resemble the actual concentration flowing from the system is all of the top peaks of the graph in figure 4.16, as these are the values recorded right before closing of the valve.

For the crossed-over O_2, the opposite is the case. On this side most of the contents in the gas phase is H_2, which diffuses out of the sensor housing relatively quickly compared to O_2, raising the fraction of O_2 in the hydrogen side sensor housing. Again, this means the value coming from the sensor right before the valve shuts is most accurate. But on the hydrogen side of the system these are not the top peaks as they were on the oxygen side, but the bottom peaks in the graph, figure 4.15.

It must be noted that another explanation for this ”noise” could be a leaking sensor housing. Yet, care was taken into properly sealing the housing, and as the umbrella valve mentioned in section 3.2.1 prevents pressure in sensor housing from raising more than 0.1 bar above 1 atm, leaking of sensor housing contents is assumed negligible.

- One of the goals of this research is to determine steady-state values for gas crossover coming from the stack, yet gas measurement is performed on the gas phase of the buffer tanks; not directly on gas flowing from the stack. This means that when equilibrium temperature is reached, and the the stack is operating steady-state including steady-state crossover, it takes some additional time before the entire system of flash tanks and buffer tanks is flushed with this steady-state gas composition flowing from the stack. This can be observed in the data as measured crossover increases a little further even after the control pressure and equilibrium temperature have been reached, before it stabilizes at its steady-state value.

Pressure difference over the diaphragm
With control operating the gas measurement system solenoid valves as illustrated in section 3.2.1, the majority of valve openings happen out of phase. This means most of the time only one valve is open, with possible pressure differences ΔP over both sides of the system as a result. Pressure differences could contribute significantly to crossover by electrolyte permeation, as explained in section 2.3.4. In an endeavor to quantify this effect the pressure response of the system during actuation of the valves has been logged, with a sampling frequency of $36.36\ Hz$. The result of which is presented in figures 4.8 and 4.9.

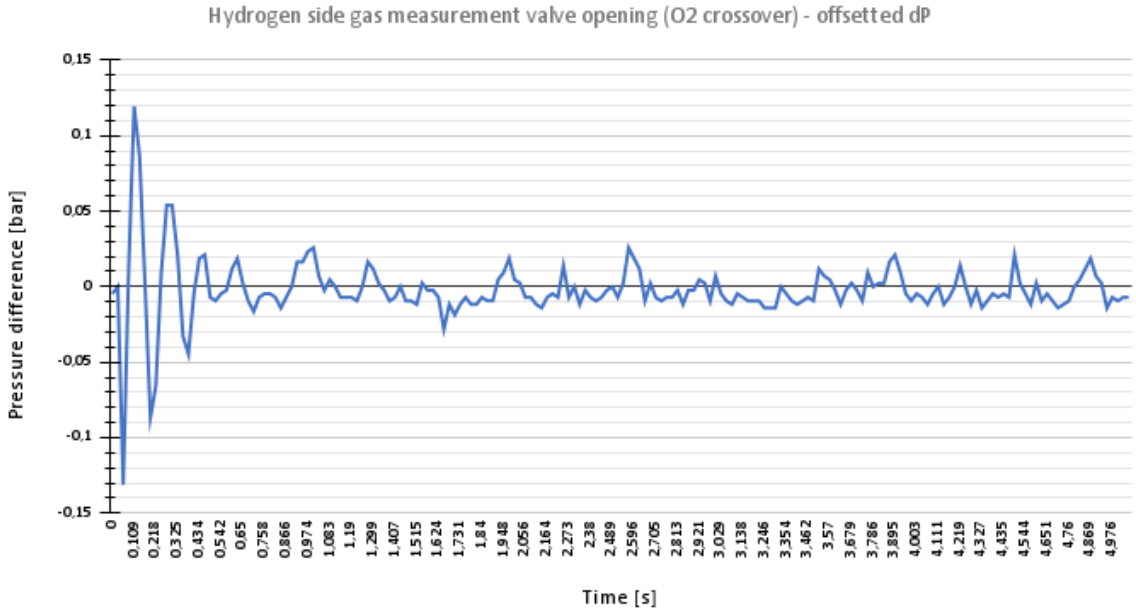

Figure 4.8: Pressure response upon opening of the hydrogen side gas measurement valve. Valve opening duration: $5000\ ms$. ΔP is defined as $P_{H_2side} - P_{O_2side}$, and graph has been adjusted to cancel out the offset between sensors.

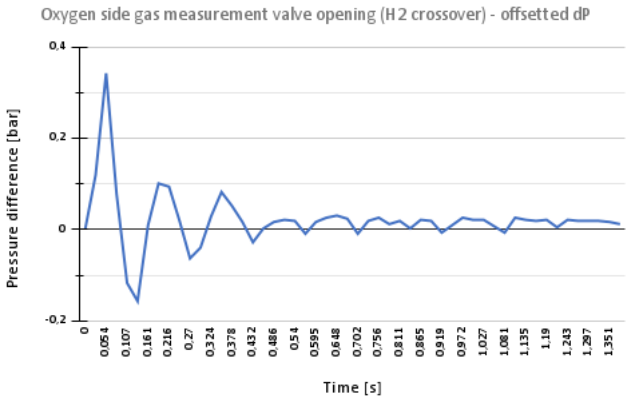

Figure 4.9: Pressure response upon opening of the oxygen side gas measurement valve actuation. Valve opening duration: $1300\ ms$. ΔP is defined as $P_{H_2side} - P_{O_2side}$, and graph has been adjusted to cancel out the offset between sensors.

Figure 4.10 is the pressure response when the system is at ambient conditions, revealing sensor noise. The noise in pressure difference due to sensor noise is of 0.005 bar order of magnitude, with occasional spikes to 0.01 bar. Another goal of the ambient test was to determine the offset between the pressure sensors on both sides of the system. The offset at ambient was obtained by determining the average

ΔP over the full duration of the hydrogen side gas measurement valve actuation.
Offsetting the pressure data from the test at 50 bar with the offset acquired from the ambient test produced a surprising result. It would suggest that when the oxygen side gas measurement valve is actuated, the pressure on that side of the system would exceed the pressure on the hydrogen side for most of the time while the valve is open. This is in fact not possible, as the oxygen side gas measurement valve is actuated by level control, meaning in terms of control its purpose is to raise the level on the oxygen side. This would not happen if the pressure on the oxygen side exceeds the pressure on the hydrogen side. This tells us that the sensor offset is not constant, and could be dependent on pressure, temperature, time or another conceivable variable. This observation introduces difficulties when it comes to identifying the dominant source for crossover.
In order to produce figures 4.8 and 4.9, the data has been corrected with the offset determined at the final data point before the valves where actuated. This produces credible results, but the exact value of the offset during these tests remains unknown.

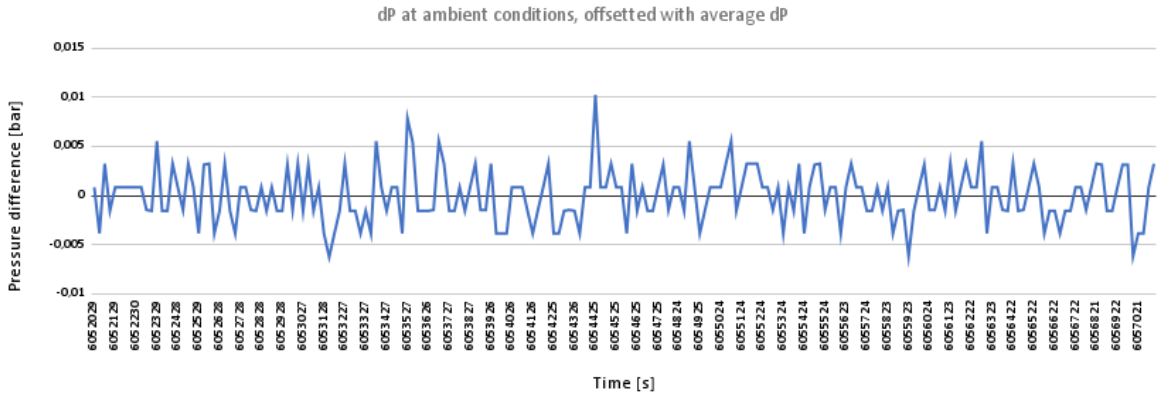

Figure 4.10: Pressure response at ambient pressure: fluctuations are the result of measurement noise of either pressure sensor. Noise in pressure difference fluctuates with an amplitude of ~0.005 bar, with occasional spike to 0.01 bar.

What can be observed in figure 4.8 is that when the hydrogen side gas measurement valve is opened the following sequence of events occurs:

1. As the valve is opened, hydrogen side pressure drops compared to oxygen side, leading to a growing negative ΔP as defined in figure 4.8 caption.
2. When the differential pressure is large enough to overcome the flow resistances inside the system, electrolyte starts to be forced towards the hydrogen side, albeit with a slight delay due to electrolyte inertia.
3. Electrolyte continues to be forced towards hydrogen side, up until the pressure on both sides of the system is equalized. This happens in under 0.05 seconds.
4. As the body of fluid that's being brought into motion now has kinetic energy, it will continue to flow towards hydrogen side even after the pressure is equalized due to its inertia. This causes the pressure on the hydrogen side to rise and on the oxygen side to drop, even when the hydrogen side gas measurement valve is still open. This happens until forces due to the growing differential pressure towards the oxygen side overcome the kinetic energy of the electrolyte.
5. At this point, the differential pressure towards the oxygen side is at its peak, forcing the electrolyte back the other way. Step 3 and 4 now repeat, only towards the other side of the system.
6. After approximately $450\ ms$ the oscillations have been dampened to where the amplitude is $<$ 0.025 bar, upon which noise in pressure measurement makes it increasingly difficult to recognize further response in pressure differences. In this section, as the hydrogen side valve is still open, there will be a slight pressure difference towards the hydrogen side. This pressure difference is however very low, estimated below 0.02 bar, as there is now a more constant flow of electrolyte

towards the hydrogen side, with equally constant velocity. This flow of electrolyte is able to match the pressure response on the hydrogen side, causing the pressure on both side of the system to drop equally fast, resulting in a very low difference in pressure. At this point it is assumed there is mainly flow through the pressure equalization tube and negligible flow through the diaphragm, as pressure difference over the diaphragm is very low.

The same behaviour is observed when the oxygen side gas measurement valve is actuated, only in reverse direction. A keen eye will have seen that the peaks in differential pressure are higher in this case, as can be observed in figure 4.9. This can be explained by the difference in tuning of the throttling devices (needle valves) of the gas measurement system, as explained before. The hydrogen side throttling device is more finely tuned than the oxygen side, to compensate for the difference in flow speed of H_2 compared to O_2. This data however shows that this effect might have been overcompensated, as system pressure drops 0.588 bar during $5000\ ms$ of hydrogen side gas measurement valve opening, compared to 1.059 bar during $1300\ ms$ of oxygen side gas measurement opening (at 50 bar and $45°C$ operating temperature). The difference in pressure drop upon actuation of the valves is also clearly visible in the highlighted section of figure 4.3. This does however indicate that increased throttling of the flow reduces the magnitude of the peak of the differential pressure, which could possibly reduce electrolyte permeation and electrolyte mixing, and with that their contribution to gas crossover.

The net effect of this is an oscillating flow of electrolyte upon actuation of the gas measurement system, which is damped by friction in the tubes/diaphragm, as well as by the escaping gas. It is an underdamped oscillation, as the flow oscillates with decreasing amplitude, until it reaches a zone where the amplitude is in the order of magnitude of the noise in pressure measurement. What can be observed is that this is reached in approximately $500\ ms$, long before the valve is shut again. This shows that the pressure is equalized relatively quickly. It also shows that the assumption of hydrogen in gaseous state not being able to permeate through the diaphragm is valid, as we are still far away from the 5.5 bar limit in pressure difference mentioned in literature [74].

In an endeavor to filter out noise from the obtained data and gain knowledge on the dominant frequencies, a Fourier transform has been performed on the data using matlab. The results of this can be observed in figures 4.11, 4.12 and 4.13.

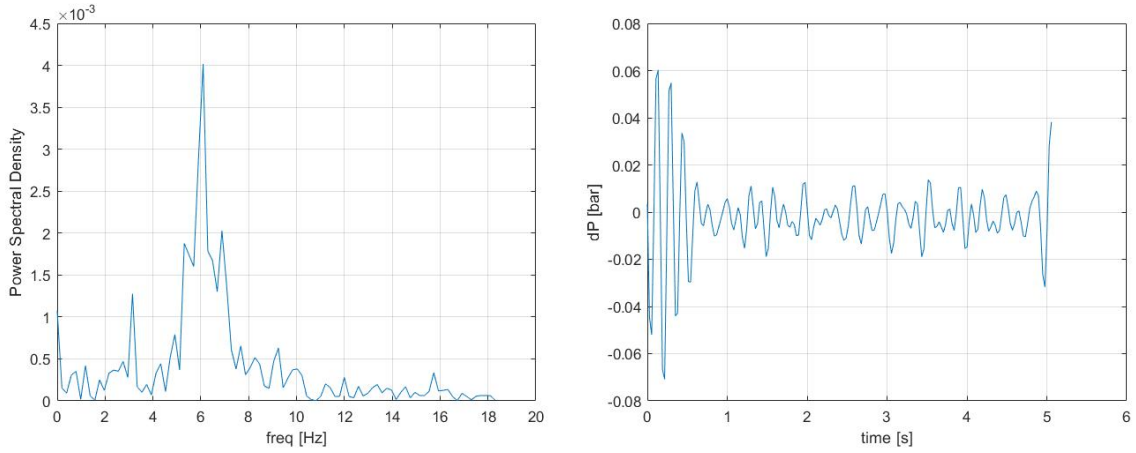

(a) Power spectral density plot - hydrogen side gas measurement

(b) Filtered signal - hydrogen side gas measurement

Figure 4.11: Fourier transform: hydrogen side gas measurement. Valve opening duration: $5000\ ms$.

As the sampling frequency is $1/0.0275 = 36.36 Hz$, the range of frequencies which is viable for analysis is from 0 to the Nyquist frequency of $18.18\ Hz$. In this spectrum the power spectral density plots for both signals show some interesting results:

- In the hydrogen side gas measurement valve actuation, the signal is strongest at a frequency of 3, 5, 6 and $7\ Hz$, showing peaks in the PSD plots.

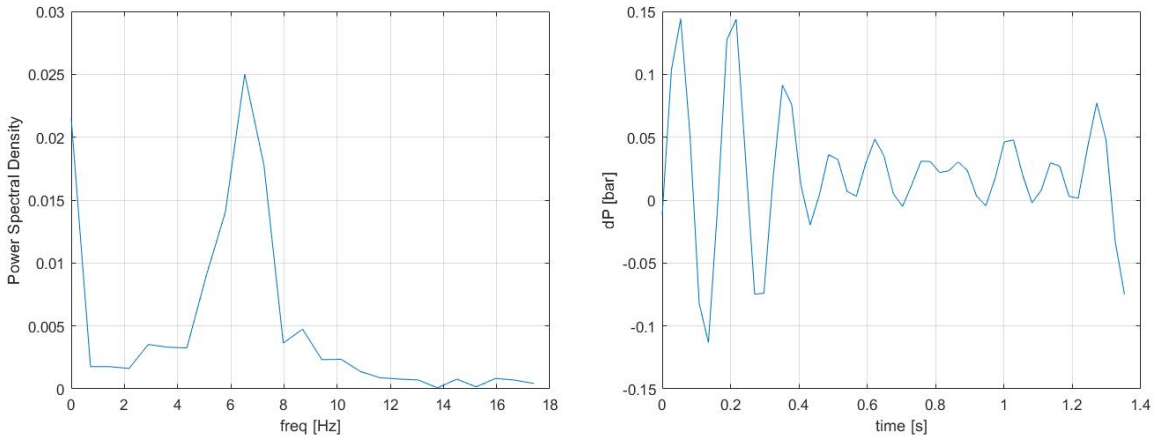

(a) Power spectral density plot - oxygen side gas measurement

(b) Filtered signal - oxygen side gas measurement

Figure 4.12: Fourier transform: oxygen side gas measurement valve actuation. Valve opening duration: $1300\ ms$.

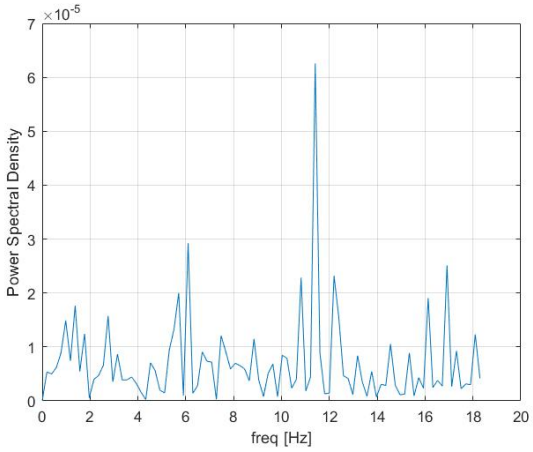

Figure 4.13: Power spectrum density plot - hydrogen side gas measurement valve actuated at ambient conditions

- During oxygen side gas measurement valve actuation there is also a clear peak at just over $6\ Hz$. This seems to be the first eigenfrequentie of the electrolyte, and it can be observed as the frequency of the damped oscillation in figures 4.8 and 4.9.
- Interestingly this peak at just over $6\ Hz$ was also recorded in the ambient test, as it's visible in its PSD plot figure 4.13, even after the system had been exposed to ambient conditions for over 30 minutes.
- The other noticeable peak from the PSD plot of the ambient figure 4.13 is at around $11.5\ Hz$, which is close to a multitude of the $6\ Hz$ peak.
- After applying a high pass filter on the hydrogen side data of $> 6.5 \cdot 10^{-4}$ and on the oxygen side data of $> 6.5 \cdot 10^{-3}$ to cut power to all but the dominant frequencies, figures 4.11b and 4.12b are obtained.
- It can be observed that the differential pressure in the period after the oscillation has dampened but before the valve is closed for the hydrogen side gas measurement is still fluctuating, but seems to fluctuate around 0.005 bar towards the hydrogen side with a maximum amplitude of 0.015 bar. While in the oxygen side valve actuation during this period this fluctuation is of slightly larger amplitude, 0.05 bar, and also fluctuating around a slightly higher value of 0.025 bar towards the oxygen side. The mean values are of course only valid under the assumption that the offset is somewhat correct, but the difference in amplitude is not affected by this uncertainty. This again

shows that increased throttling seemingly lowers the peak and average pressure difference during valve actuation.

- The filtered data reveals that due to inertia of the electrolyte it very shortly continues to flow towards the side of the system where gas measurement has just taken place right after the valve has closed, creating a spike in ΔP which was not visible in figures 4.8 and 4.9.

4.2. Results and Discussion

In this section the results in terms of gas purity/crossover acquired during over 194 hours of experiments will be presented. Analysis of the results and possible explanations for the observed phenomena will be put up for discussion.

4.2.1. O_2 crossover - hydrogen side gas measurement

The acquired data for the steady-state (unless stated otherwise) hydrogen side O_2 concentration is presented in table 4.3. As the value for the upper explosion limit is dependent on pressure and temperature these are presented as well. Operating temperature in most of the experiment is actually lower than 80°C at which the UEL was taken, which means UEL values during actual experiments will in most cases be slightly higher than stated in table 4.3. Since several experiments were conducted before cooling was installed, the steady-state temperatures at which the values were obtained are noted. The following can be observed:

Effect of operating pressure - O_2 crossover

There is a noticeable dependency on operating pressure. The amount of dissolved O_2 in electrolyte solution on the oxygen side is directly proportional to its partial pressure in the oxygen side gas phase according to Henry's law equation 2.47, which is in term proportional to the absolute pressure if we assume that the mole fraction of O_2 in the oxygen side gas phase is independent on operating pressure. This assumption is reasonable, as can be observed in table 4.4. This increase in dissolved O_2 adds to crossover through both diffusion and convection, which would lead one to believe that an increase in pressure would be accompanied by an increase in cathodic O_2 concentration by about the same factor. This one:one relation is however not observed in these experiments. Yet, this one:one dependency on pressure was also not reported in literature. In fact, the measured fractional increase in hydrogen side O_2 concentration upon doubling of operating pressure is actually quite comparable to what is mentioned in literature [28]. Hydrogen side O_2 concentration increased by a factor of 1.4 and 1.7 when operating pressure was increased from 20 to 40 bar at $100\ mA/cm^2$ and $150\ mA/cm^2$ respectively, which is comparable to results obtained by Ju et al. presented in table 2.3.

Effect of operating temperature - O_2 crossover

As several experiments have been conducted before and after cooling was installed, there is a possibility to compare cathodic O_2 concentration at different operating temperature for the same current density and operating pressure. Literature states that a temperature rise in this range will slightly decrease O_2 solubility, while the diffusion coefficient rises by a factor of ~1.5 [58][69]. These effects have counteracting consequences on O_2 crossover. Yet, as electrolyte viscosity is also dependent on temperature, an increase in O_2 crossover is expected. The data on this is however not that conclusive. At 20 bar and $150\ mA/cm^2$ a slight increase in cathodic O_2 concentration was observed when the temperature was increased from $45°C$ to $72°C$. Yet, at the same current density in the 30 bar experiments, a decrease in cathodic O_2 concentration was observed for a similar temperature increase. The accuracy of the measurement could prohibit revealing the true temperature dependence of O_2 crossover, as measurement "noise" due to outward diffusion of H_2 could be in the same order of magnitude as temperature effects.

Effect of current density - O_2 crossover

When looking at differences in cathodic O_2 concentration values for for different current densities the same can be said with respect to measurement accuracy. At constant temperature one would expect crossover to be less at higher current density, as gas production is higher and absolute crossover through diffusion would stay the same, which would result in a drop in cathodic O_2 concentration. Yet, in the ZEF system temperature is an uncontrolled variable. This means higher current density is accompanied with higher operating temperatures, which is assumed to increase crossover through both diffusion and convection. The net effect is that here as well it is difficult to quantify the effect of current density on O_2 crossover. The inconsistency in effect is observed when comparing 30 bar 100-$200\ mA/cm^2$ experiments, and 50 bar 150-$300\ mA/cm^2$ steady-state experiments, as contradicting behaviour is observed.

Safety

Up until now it has proven difficult to be conclusive on the effect of process parameters on O_2 crossover, apart from the effect of operating pressure. It is however possible to be conclusive in terms of safety:

Current density:					
400 mA/cm²					0.25% (not SS, 83°C)
350 mA/cm²					0.31% (SS, 77°C)
300 mA/cm²					0.29% (SS, 73°C)
250 mA/cm²				0.32% (SS, 65°C)	0.34% (close to SS, 64°C)
200 mA/cm²			0.27% (SS, 56°C)	0.32% (SS, 56°C)	0.33% (close to SS, 54°C)
150 mA/cm²	0.25% (close to SS, 44°C)	0.27% (SS, 72°C, no cooling) 0.23% (SS, 45°C)	0.27% (SS, 73°C, no cooling) 0.30% (SS, 46°C)	0.27% (not SS, 73°C, no cooling) 0.39% (SS, 46°C)	0.39% (SS, 46°C)
100 mA/cm²	0.23% (SS, 37°C)	0.24% (SS, 58°C, no cooling) 0.24% (SS, 37°C)	0.24% (SS, 59°C, no cooling)	0.33% (not SS, 59°C, no cooling)	0.32% (not SS, 39°C)
Operating pressure:	15 bar	20 bar	30 bar	40 bar	50 bar
50% UEL at 80°C:	2.7%	2.7%	2.65%	2.6%	2.5%

Table 4.3: Obtained values for the hydrogen side O_2 concentration. (SS): value obtained at steady-state

O_2 crossover is **not** the limiting factor in terms of safety for the ZEF AEC system.
Even if the UEL values are taken with a slight safety margin as values have been adopted for a temperature of $80°C$, the steady-state hydrogen side O_2 concentration never exceeds 0.4%. This confirms what is reported in literature [63][61][28].

Due to the nature of the control scheme the hydrogen side gas measurement valve is only actuated when the control pressure is reached. This moment can be observed at ~300 seconds in figure 4.14. The composition of the gas content of the sensor housing before any gas has passed through the gas measurement system is at ambient conditions, containing 20.9% O_2. Cathodic O_2 concentration data only becomes relevant when the housing is flushed with gas sampled from the system. The time it takes to flush the sensor housing is production rate-, and thus current density dependent.

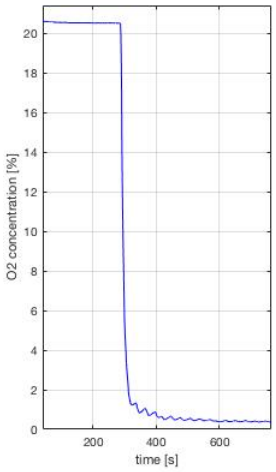

Figure 4.14: O_2 concentration in housing drops from ambient conditions when pressure control actuates hydrogen side gas measurement valve.

Figure 4.15 shows the typical course of cathodic O_2 concentration during an experiment. This data is gathered from the same experiment as the temperature course in figure 4.5. As mentioned before, it can be observed that the O_2 concentration on the hydrogen side of the system continues to rise even after equilibrium temperature is reached after about 10^4 seconds (red dashed line), as it takes some additional time before the the hydrogen side flash tank and buffer tank are flushed with the steady-state gas composition flowing from the stack.
As stated earlier, the relevant values of the graph in figure 4.15 are all the bottom peaks, as these values are closest to the actual concentration flow-

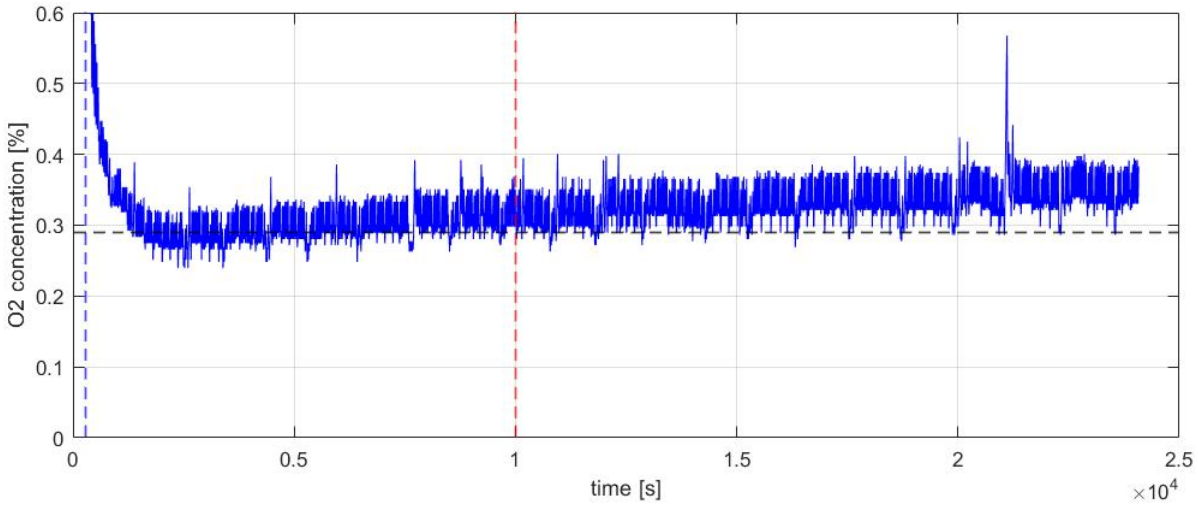

Figure 4.15: O_2 concentration vs time - current density: $300\ mA/cm^2$ operating pressure: 50 bar. Dashed lines indicate: control pressure reached (blue), 95% steady-state temperature reached (red), steady-state hydrogen side O_2 concentration (black)

ing from the system. The measurement "noise" is in the range of ~30% of the measured value, which could be the same order of magnitude as deviations in O_2 crossover due to varying process conditions such as current density, pressure and temperature. The absolute amount of O_2 crossover is however comparable to reports in literature [28].

What can be concluded from this is that although obtained results are perhaps less helpful for science, they are helpful in terms of safety. Due to aforementioned gas measurement system traits measured values obtained through experiments are either very close to or slightly over actual hydrogen side O_2 concentration, and still comfortably distant from the 50% UEL safety limit.

Current density:					
400 mA/cm²					2.5% (not SS, 83°C)
350 mA/cm²					3.04% (SS, 77°C)
300 mA/cm²					2.96% (SS, 73°C)
250 mA/cm²				2.72% (SS, 65°C)	3.00% (close to SS, 64°C)
200 mA/cm²			2.3% (SS, 56°C)	2.70% (SS, 56°C)	2.54% (close to SS, 54°C)
150 mA/cm²	1.4% (close to SS, 44°C)	2.5% (SS, 72°C, no cooling) 1.65% (SS, 45°C)	2.9% (SS, 73°C, no cooling) 2.38% (SS, 46°C)	3.0% (not SS, 73°C, no cooling) 2.65% (SS, 46°C)	3.47% (SS, 48°C)
100 mA/cm²	1.8% (SS, 37°C)	2.7% (SS, 58°C, no cooling) 2.21% (SS, 37°C)	2.8% (SS, 59°C, no cooling)	3.3% (not SS, 59°C, no cooling)	3.1% (not SS, 39°C)
Operating pressure:	15 bar	20 bar	30 bar	40 bar	50 bar
50% LEL at 50°C:	2.55%	2.65%	2.65%	2.70%	2.70%
50% LEL at 80°C:	2.5%	2.6%	2.6%	2.65%	2.65%

Table 4.4: Obtained values for the oxygen side H_2 concentration. (SS): value obtained at steady-state

4.2.2. H_2 crossover - oxygen side gas measurement

The acquired data for the steady-state (unless stated otherwise) oxygen side H_2 concentration is presented in table 4.4. The explosion limit is again operating temperature and pressure dependent, thus relevant LEL values are reported in the table as well. All steady-state values are acquired from system with cooling installed, unless stated otherwise.

Effect of operating pressure - H_2 crossover

As can be observed in table 4.4, once again there is a very clear dependency of foreign gas concentration on operating pressure. According to Henry's law, equation 2.48, the amount of H_2 dissolved in the electrolyte solution is proportional to the cathode side H_2 partial pressure, which is again proportional to the absolute pressure assuming the mole fraction of H_2 in the hydrogen side gas phase is independent on operating pressure. When looking at table 4.3 this assumption seems reasonable, as fraction is always over 99.5%. Increased operating pressure increases H_2 crossover due to the same principle as the increase in O_2 crossover, but as the solubility and diffusion coefficient of H_2 in $30\ wt\%$ KOH solution are significantly larger than for O_2 for temperatures above $25°C$, the effect is magnified [58]. As a consequence, at 50 bar all steady-state H_2 concentration values are above 50% LEL for the entire range of current densities that have been tested.

Effect of operating temperature - H_2 crossover

The data on temperature dependency of H_2 crossover presented in table 4.4 is, unlike O_2 crossover data, very conclusive. Higher operating temperature has led to higher crossover at constant current density and pressure, in all four current density/pressure combinations which have been tested pre and after cooling installment. The following could serve as an explanation for the observed dependency.
As mentioned in section 2.3.2, H_2 solubility increases significantly when temperature is increased.

Schalenbach et al. calculated values for H_2 solubility to increase by a factor of 2 when temperature increases from $30°C$ to $80°C$ [58]. However, the effects of temperature increase don't stop here. Kuznetsov et al. reported a drop in KOH solution dynamic viscosity by a factor of 2 when temperature is increased from $20°C$ to $69°C$ (at 1 atm), and less viscous electrolyte means crossover by convection could increase [38].
At the same time, diffusion is another phenomena dependent on temperature, which means both mechanisms for crossover, convection and now also diffusion, are affected by this rise in temperature. As explained in section 2.3.4, the H_2 diffusion coefficient in $30\ wt\%$ KOH solution increases roughly logarithmic with temperature. An increase by a factor of over 3 is reported when temperature is increased from $25°C$ to $80°C$ [69]. This increase in diffusion coefficient results in an increase in H_2 crossover flux by diffusion. It must be noted that O_2 diffusion coefficient is equally dependent on temperature. Yet, as mentioned previously the H_2 diffusion coefficient is significantly higher in absolute terms; $D_{H_2} \approx 3D_{O_2}$. Combine this with the fact that for $30\ wt\%$ KOH electrolyte solution O_2 solubility actually decreases when temperature is increased, the effect of temperature on H_2 crossover could be much more substantial. To sum up the effects of an increase in temperature: we now have a liquid with a larger quantity of stuff dissolved, with stuff that is able to move quicker through the liquid, in a liquid which itself flows with less resistance. The net result of this could be the reason why the effect of operating temperature on crossover is clearly visible in the case of H_2 [58][63]. The logarithmic dependency of diffusion coefficient on temperature could also explain why in the 20 bar experiments, an increase from $45°C$ to $72°C$ resulted in a fractionally larger increase in H_2 crossover than when temperature was increased from $37°C$ to $58°C$, despite the latter being performed at a lower current density, at which the lower gas production rate would magnify the effect of an increase in flux of H_2 towards the oxygen side.
It must be noted that at elevated pressure the effect of increased temperature on H_2 crossover seems to become smaller.

Effect of current density - H_2 crossover
The effect of current density is once again obscured by the fact that temperature is an uncontrollable variable in the ZEF AEC system. This means that even though lower oxygen side H_2 concentration is expected at higher current density due to larger gas production, higher temperatures as a result of these higher current densities prohibit this concentration from dropping significantly. At 20 bar this effect is however still observable, as increasing the current density from $100\ mA/cm^2$ to $200\ mA/cm^2$ decreases the oxygen side H_2 concentration despite an increase in temperature.

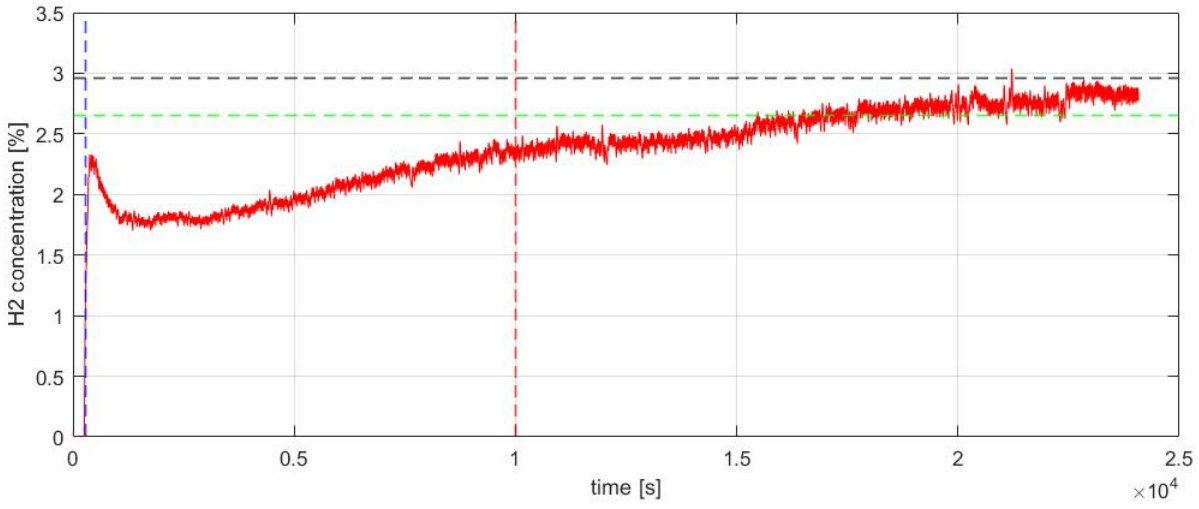

Figure 4.16: H_2 concentration vs time - current density: $300\ mA/cm^2$ operating pressure: 50 bar. Dashed lines indicate: control pressure reached (blue), 95% steady-state temperature reached (red), steady-state hydrogen side O_2 concentration (black), 50% LEL safety limit (green).

Figure 4.16 shows a typical course for oxygen side H_2 concentration. Just like its counterpart, H_2 concentration continues to rise after equilibrium temperature is reached at approximately 10^4 seconds

(red dashed line). Interestingly the ”noise” in measurement grows larger as the experiment runs. In order to try and explain this, it's convenient to recall what causes this noise. The drop in H_2 concentration of the contents of the sensor housing is likely to be mostly due to the outward H_2 diffusion, lowering the concentration when the gas measurement valve is shut. Larger noise could therefor be a result of: a- longer duration between actuation of the measurement valve giving it more time to diffuse, b- increase in diffusion rate due to temperature effects or c- increase in diffusion rate due to larger concentration gradient between sensor housing gas content and ambient. In order to identify the main cause, we look at factors involved. If indeed time between valve actuation would be longer, there should either be a significant change in production, operating pressure or temperature. The latter of which reaches it's steady-state value the latest, at around 10^4 seconds in this case (red dashed line), after which we still see an increase in measurement ”noise”. Explanation ”a” therefor seems unlikely to be the main contributor to this phenomena. Explanation ”b” falls victim to the same reasoning as explanation ”a”, as temperature effect would stabilize after equilibrium temperature is reached. Explanation ”c” however seems plausible, as roughly doubling the H_2 concentration of the sensor housing content increases measurement ”noise” by the same order of magnitude. For this reason the concentration gradient of H_2 between sensor housing content and ambient is believed to be the main reason for this phenomena.

Spike after start-up

As explained in section 4.1.2, the oxygen side H_2 content was consistently first to be measured. Level control actuates the oxygen side gas measurement system every time the level sensor runs dry, which takes between 35 and 120 seconds depending on the current density. As a result, the composition of the oxygen side gas phase is monitored almost instantly when the system is turned on. Right after start-up a spike in H_2 concentration is observed consistently in all experiments (apart from primary experiment upon filling the system with fresh electrolyte). This phenomena has previously been predicted by Schwarze et al, as he modelled crossover during system off-time [63]. The spike is a direct result of H_2 diffusion, which doesn't stop when the system is turned off. As a result anodic H_2 concentration rises during off-time, until both sides off the diaphragm are at equal concentration. After start-up of the system, electrolyte with elevated H_2 concentration flows from the anodic half-cell into the oxygen side flash tank, causing the spike in measured H_2 concentration. The spike can be observed as a peak in figures 4.16, 4.17a and 4.17b.

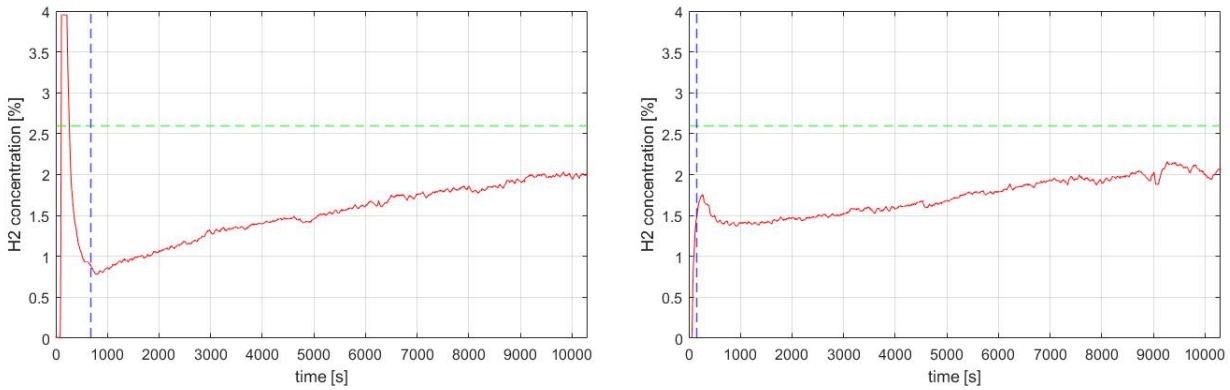

(a) Start-up after system was left at ambient pressure

(b) Start-up after system was left under pressure

Figure 4.17: Oxygen side H_2 concentration upon start-up of system - current density: $150\ mA/cm^2$ operating pressure: 20 bar. Dashed lines indicate: control pressure reached (blue), 50% LEL safety limit (green).

The magnitude of the spikes in oxygen side H_2 concentration have been documented and presented in table 4.5. What can be observed is that there is a clear distinction in magnitude of spike between when the system remained under pressure during the night, and when the system was brought back to atmospheric pressure. In all experiments which were conducted after the system was left at atmospheric pressure the magnitude of the spike exceeded the measurement range of the H_2 detection sensor on the oxygen side of the system, which is 3.95%. An example of such a spike can be observed in figure 4.17a. Figure 4.17b on the other hand shows the spike after the system was left under pressure for the night, for the same current density. The magnitude of the spike is lower in this case as there is more

Current density:					
400 mA/cm²					2.65% (r.u.p.)
350 mA/cm²					>3.95% (r.u.p.)
300 mA/cm²					2.33% (r.u.p.) 1.85% (r.u.p. conf B)
250 mA/cm²				3.38% (r.u.p.)	3.24% (r.u.p.)
200 mA/cm²			3.16% (r.u.p.)	3.53% (r.u.p.)	2.31% (r.u.p.)
150 mA/cm²	>3.95% (atm)	>3.95% (atm) 1.75% (r.u.p.)	2.53% (r.u.p.) >3.95% (r.u.p.)	>3.95% (atm) >3.95 (r.u.p. 3 days)	>3.95% (atm) 2.86% (r.u.p.)
100 mA/cm²	1.47% (r.u.p.)	>3.95% (atm) 1.95% (r.u.p.)	>3.95% (atm)	3.03% (r.u.p.)	>3.95% (r.u.p.)
Operating pressure:	15 bar	20 bar	30 bar	40 bar	50 bar
50% LEL at 20°C:	2.4%	2.45%	2.55%	2.65%	2.8%

Table 4.5: Peak value for oxygen side H2 content after start-up. (r.u.p.: remained under pressure during the night before) (atm: remained at atmospheric pressure during the night before)

gas present inside flash and buffer tank, resulting in a fractionally lower amount of H_2 compared to O_2, and thus lower oxygen side H_2 concentration. As a result the oxygen side H_2 concentration remains below the 50% LEL safety limit (green dashed line) in this case. Another interesting observation is that although the spike is lower in this case, the drop after the spike is significantly smaller. This shows that although the spike is lower H_2 crossover in absolute terms is actually higher when the system is left under pressure, as more H_2 remains solved in the electrolyte solution.
Even though the operating pressure of 20 bar in the experiment from figure 4.17a was reached in about 700 seconds compared to 150 seconds (blue dashed lines) in the experiment from figure 4.17b, it takes about 10^4 seconds for the oxygen side H_2 concentration to be at equal height in both experiments. This is interesting, as it is assumed that the electrolyte in the cathodic half-cell is saturated with H_2 from the moment the power is turned on. Should this assumption be true, we would expect that after 700 seconds, when conditions are equal in both experiments, the oxygen side H_2 concentration to be about equal in both experiments, if and only if crossover would occur solely through the diaphragm. As this is not the case, this acts as proof that there are indeed other routes for crossover, for example through the pressure equalization tube. This could also explain why the experiment from figure 4.17b remained at higher oxygen side H_2 concentration, as during that time in that experiment the electrolyte present on the hydrogen side of the system which has not yet been in the cathodic half-cell has a higher H_2 content, as in this case the system had been left under pressure during the night. It also shows that it takes time for all hydrogen side electrolyte to become saturated with H_2. It must be noted the temperature profile in both experiments is the same, as apart from starting pressure all other parameters were kept equal.

What can be deduced from this is that in terms of safety it is advisable to keep the system in operation all of the time, as this prohibits electrolyte from remaining in the cell for increased duration compared to during steady-state operation, at which point no spike in oxygen side H_2 concentration would be caused. If it's unavoidable to turn the electrolyser off from time to time, the advice is to keep off-time duration as short as possible, and to keep the system under pressure the entire time, in order to keep the effect that comes from increased anodic H_2 concentration at a minimal.

4.2.3. Safety window

What can be concluded thus far is that in terms of safety H_2 crossover is the limiting factor. The safety window is therefor determined by the level of H_2 concentration on the oxygen side of the system. Figure 4.18 shows the safety window for the current ZEF AEC system with cooling installed, and under the assumption the system is in operation 100% of the time. The latter condition is in place in order to be able to establish the safety window from the steady-state values, as this prevents the spike in oxygen

side H_2 concentration after start-up.
The shape of the window is quite different from what was expected, figure 3.1. This is primarily due to the fact that although cooling was installed, temperature is still not controllable in the current ZEF AEC system. The rise in temperature as a result of increasing the current density means oxygen side H_2 concentration goes up as well, introducing a top limit to the current density in terms of safety.

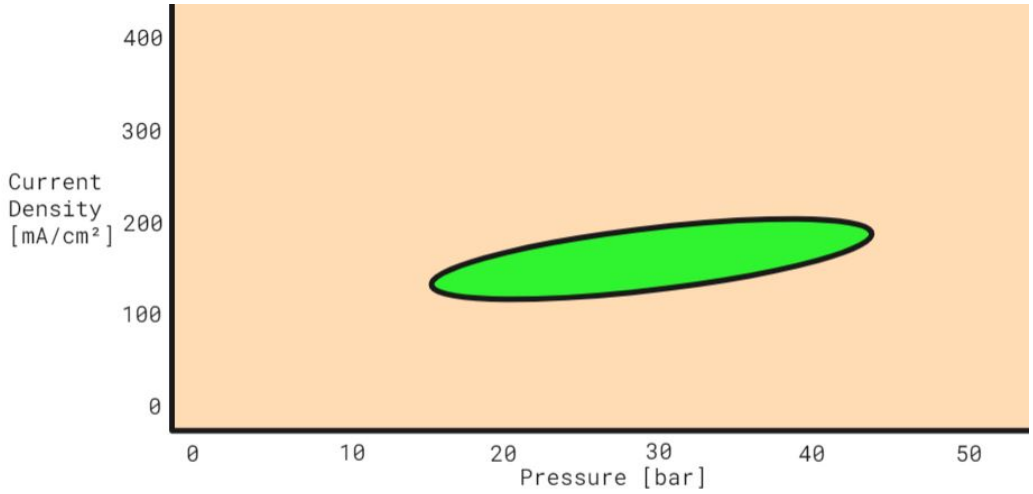

Figure 4.18: Window for safe operation considering steady-state. (safe zone is in green)

It can also be observed that for the current ZEF AEC system, at an operating pressure of 50 bar all tested current densities resulted in over 50% LEL levels of oxygen side H_2 concentration.

4.2.4. Effect pressure equalization tube on crossover

Up until this point, all data presented has been gathered during operation with pressure equalization tube configuration A. With an inner volume of $2.5\ cm^3$ this yields the smallest inner volume out of the three configurations. When comparing volumetric production of O_2 and analyses of the data on oxygen side gas measurement at 50 bar, the volume of gas released from the system at operating conditions was found to be in the 15 to $20\ cm^3$ order of magnitude, each time the valve is actuated (this results in a rise in oxygen side electrolyte level of ~$2\,cm$). The volume of the gas extracted is therefor 6 to 8 times larger than the volume content of pressure equalization tube in configuration A, which indicates that electrolyte saturated with H_2 is very likely able to reach the oxygen side of the system. For comparison sake, the extracted gas volume would fit at least three times in PET configuration B, and at least 11 times in PET configuration C.

Figures 4.19a and 4.19b show oxygen side H_2 concentration for configuration B and C.
It must be noted that the night before the experiment with PET configuration B the system was left under pressure, while the experiment with PET configuration C was conducted right after the system was filled with electrolyte solution, explaining the difference in shape upon start-up of the system as elaborated in section 4.2.2. But just like in the experiments from figures 4.17 when no parameters where changed except for the pressure at which system was kept during the night before the experiment, after 10^4 seconds oxygen side H_2 concentration for configuration B and C is in the same order of magnitude. Interestingly, at that time oxygen side H_2 concentration in the configuration B experiment is about 14% lower relative to the configuration C experiment, despite the smaller inner volume. After $1.6 \cdot 10^4$ seconds the difference between them is less, then at about 4%. This could be an indication that a lengthier PET is favorable over primarily a thicker PET. It must also be noted that as steady-state oxygen side H_2 concentrations are right about at the 50% LEL value (green dashed line), any improvement, however small, is welcome and should be considered in future system design choices.
If we now compare configuration B to configuration A, figure 4.16, we see that after 10^4 seconds oxygen side H_2 concentration has dropped by only 2% relative to each other, despite the inner volume of the PET being 25 times larger. The observed differences are minor considering the difference in PET/purge volume fraction, which could mean two things:

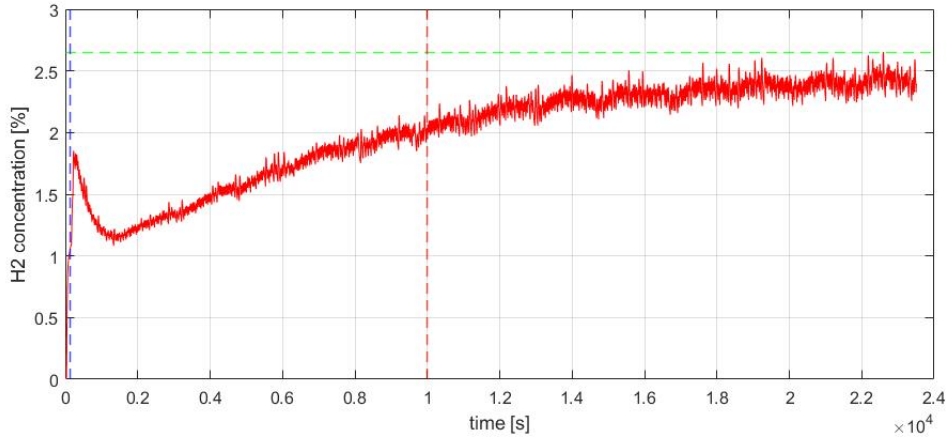

(a) PET configuration B - inner volume: $62.8\ cm^3$

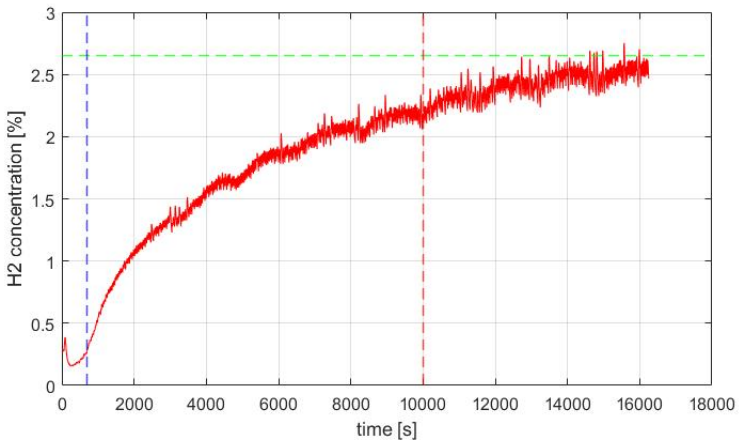

(b) PET configuration C - inner volume: $230.9\ cm^3$

Figure 4.19: Oxygen side H_2 concentration - current density: $300\ mA/cm^2$ operating pressure: 50 bar. Dashed lines indicate: control pressure reached (blue), 95% steady-state temperature reached (red), 50% LEL safety limit (green).

1. Electrolyte mixing does not play a substantial role in H_2 crossover, even in configuration A.

2. Electrolyte mixing contribution to H_2 crossover is roughly equal for all 3 tested configurations, despite the fact that volume of gas extracted per valve actuation is much smaller than inner volume of P.E.T in configurations B and C.

The first seems highly unlikely, as we've shown that volume of gas purged per opening of the oxygen side gas measurement valve is approximately an order of magnitude larger than the inner volume of the pressure equalizing tube configuration A, which means saturated electrolyte is quite certainly able to reach from the hydrogen side to the oxygen side. For this reason, point 2 is considered to be the case.
If point 2 is the case, than H_2 crossover would increase primarily as a result of flow through the pressure equalization tube towards the oxygen side of the system. As this is only the case when the oxygen side gas measurement system is actuated, the amount of mixing of electrolyte is related to the amount of actuations of this valve. The frequency of actuation of this valve is dependent on temperature and pressure, but primarily on gas production, which is a result of the level of current density. This means that increased production as a result of increased current density causes an increase in electrolyte mixing, which causes an increase in H_2 crossover. This could possibly explain why increasing current density does not have the expected effect of proportionally lowering the oxygen side H_2 concentration.

4.3. Modelling

4.3.1. CSTR model: oxygen side

As crossover through both diffusion and convection is influenced by operating temperature, it's difficult to identify which route is dominant based on the data presented thus far. In order to get an idea on the order of magnitude of H_2 crossover by diffusion through the diaphragm, the gaseous phase on the oxygen side of the system has been modeled as a continuously stirred tank reactor (CSTR). This gives insight not only in the fraction of H_2 crossover through the diaphragm compared to the pressure equalization tube of the ZEF AEC system, but also on the influence of temperature on H_2 diffusional crossover.

In order to simplify the model, the following assumptions have been made:

- The ingoing flows to the gas phase on the oxygen side are assumed to be only the produced O_2 and the H_2 which enters this side of the system by diffusion through the diaphragm.
- Diffusion of H_2 through the diaphragm is assumed to be caused entirely by diffusion through the liquid phase, and not through the solid phase of the diaphragm.
- All H_2 that enters the oxygen side through diffusion reaches the gas phase.
- The gas phase on the oxygen side is assumed to be perfectly mixed.
- The density of oxygen and hydrogen is assumed to be linearly dependent on temperature for the temperature range of the ZEF AEC system.
- The pressure remains constant during the experiment.
- The heat going into the system remains constant, and is assumed to be generated by all overpotential above the thermal-neutral voltage, which causes Joule-heating inside the system.
- The temperature of the feed of the CSTR model is assumed to be equal to the temperature of the system itself, as the product gases are produced inside the system.
- As $c_{H_2}^{an} \ll c_{H_2}^{cat}$, the H_2 concentration difference over the diaphragm Δc_{H_2} is assumed to be equal to $c_{H_2}^{cat}$, equation 2.66.
- Electrolyte on cathode side is assumed to be fully saturated with H_2.
- Supersaturation is assumed to be zero, as electrode is placed $4\ mm$ from the diaphragm, and literature states the supersaturated layer generally doesn't extend much further than the bubble layer adjacent to the electrode.
- As the O_2 side level sensor is utilized in level control, the volume of the gas phase V_{gas}^{an} is assumed to be the volume of the segment of the flash tank above the level sensor plus the volume of the O_2 buffer tank, which equals to $0.5 \cdot 99.3 + 99.3 = 148.95\ cm^3$.
- The values for the temperature dependence of the hydrogen solubility $S_{H_2,S}$ as well as the diffusion coefficient D_{H_2} have been obtained from graphs in literature [69][58]. This introduces the possibility for reading errors. The slight errors introduced are however assumed to be acceptable, as the objective is to obtain an order of magnitude, and not an exact value.

The temperature dependence of the hydrogen solubility $S_{H_2,S}$ as well as the diffusion coefficient D_{H_2} are linear in a log-linear plot. The datapoints used to put this data in equational form are presented in tabel 4.6.
The heat capacity of the system has been estimated by matching of temperature response of the model to experimental data, and mounted to a value of $6500\ J/K$.

The model is based on the following two-state CSTR model, which uses basic accounting and energy conservation principles, equations 4.2 and 4.3.

Datapoint	Temperature [K]	Hydrogen solubility $[mol/m^3/bar]$
$S_{H_2,1}$	273+46	0.1
$S_{H_2,2}$	273+80	0.15

Datapoint	Temperature [K]	Hydrogen diffusion coefficient $[m^2/s]$
$D_{H_2,1}$	273+67	$5 \cdot 10^{-9}$
$D_{H_2,2}$	273+80	$6 \cdot 10^{-9}$

Datapoint	Temperature [K]	Hydrogen density at 50 bar $[g/m^3]$
$\rho_{H_2,1}$	273+18	4160
$\rho_{H_2,2}$	273+48	3770

Datapoint	Temperature [K]	Oxygen density at 50 bar $[g/m^3]$
$\rho_{O_2,1}$	273+18	6870
$\rho_{O_2,2}$	273+48	6080

Table 4.6: Datapoints used to model temperature dependence, obtained from Tham et al., Schalenbach et al. and engineering toolbox [69][58][1]

$$\frac{dc_{H_2}^{an}}{dt} = \frac{F^{an}}{V_{gas}^{an}}(c_{H_2}^{feed} - c_{H_2}^{an}) \tag{4.2}$$

$$\frac{dT}{dt} = \frac{Q_{Joule} - Q_{cool}}{C_{system}} \tag{4.3}$$

The CSTR was modelled in simulink for a 16 cell stack, and can be observed in figure 4.20.

Results
The following results have all been generated by the model.

If we compare the temperature course produced by the model, figure 4.21, to the temperature course of the actual experiment with the same operating conditions, figure 4.5, we see that the profile matches quite well. This means that temperature develops roughly equal in the modelled and real case.

Figures 4.22a and 4.22b show the course of the H_2 diffusion coefficient and solubility as a result of the rising temperature. The results matches reported values in literature quite well.

The result of the increase in H_2 diffusion coefficient and solubility is presented in figure 4.23. As both D_{H_2} and S_{H_2} dependency on temperature is logarithmic, this can be seen in the development of the oxygen side H_2 concentration as well. What is significant is that the model shows that diffusion of H_2 through solely the diaphragms, as would be the case in a system with separated electrolyte cycles and ideal pressure control, oxygen side H_2 concentration only rises to 0.24% at steady state. This value is at least an order magnitude smaller than measured in the actual experiment, figure 4.16. This is in line with reports in literature: Trinke et al. found that H_2 crossover due to diffusion is responsible for ~8% of the total flux of H_2 towards the oxygen side [70].

Another interesting observation is that the oxygen side H_2 concentration profile obtained from the model is not to dissimilar from the profile obtained in from the actual experiment figure 4.16, with the exception of the spike after start-up. After $0.5 \cdot 10^4$ seconds they both reach approximately 70% of their final value, and both resemble an upward exponential decay. As was just deduced, over 90% of the H_2 crossover measured in experiments is believed to be the result of convective crossover, and yet the shape of the profile for purely diffusion shows significant similarity. For this reason it is believed that the parameter which influences both crossover by diffusion and convection is the main contributor to this shape, which is H_2 solubility in KOH solution.

This could mean one or a combination of the following things:

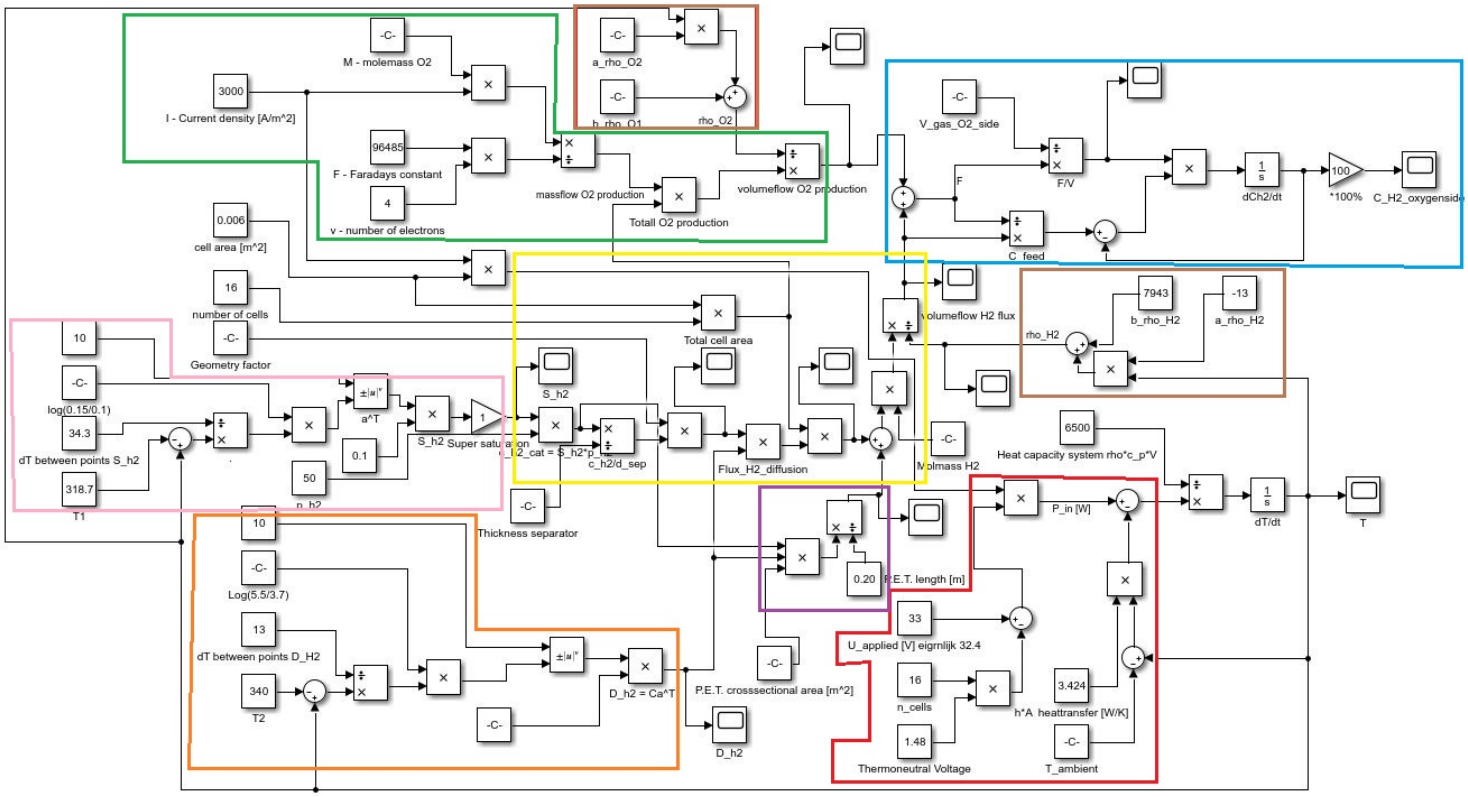

Figure 4.20: CSTR model of oxygen side gas phase, made with simulink. Section overview: orange; H_2 diffusion coefficient calculations, pink; H_2 solubility calculations, red: heat calculations, brown; density calculations, green; freed calculations, yellow; H_2 volumetric flux calculations, purple; pressure equalization tube contribution, blue; oxygen side H_2 concentration calculations.

- Diffusion through the pressure equalization tube plays a substantial role
- Supersaturated layer thickness is larger than expected, meaning levels of H_2 in dissolved state at cathode half-cell diaphragm boundary exceeds saturated conditions
- The remainder of crossover is caused by a combination of electrolyte mixing/permeation due to a difference in pressure

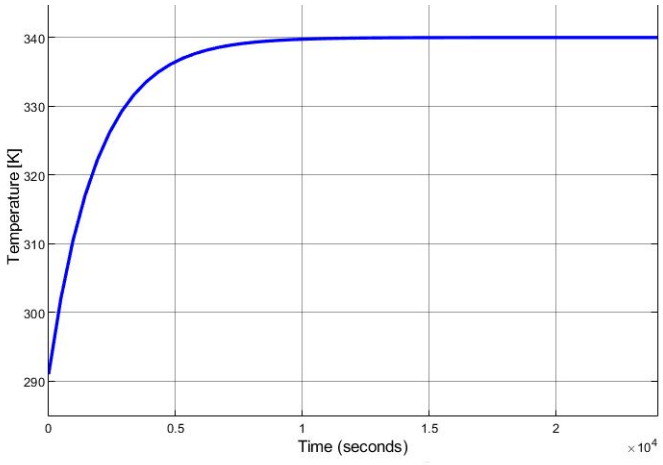

Figure 4.21: Temperature vs time modeled with CSTR - current density $300\ mA/cm^2$ operating pressure 50 bar. Modelled temperature course matches real temperature course in figure 4.5 quite well.

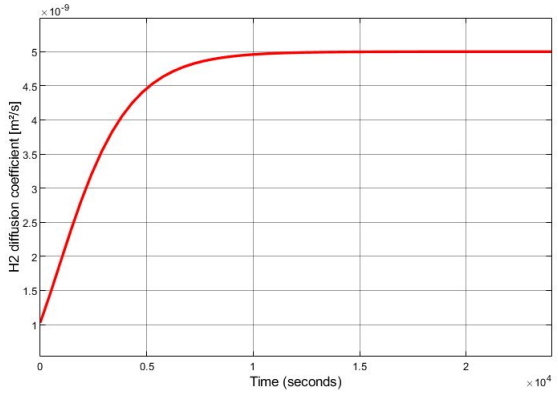

(a) Development of D_{H_2} as a result of temperature increase

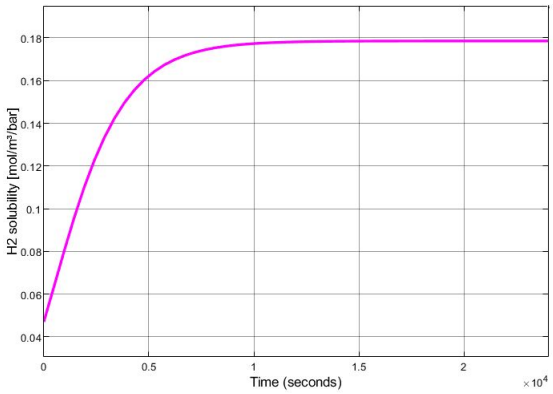

(b) Development of S_{H_2} as a result of temperature increase

Figure 4.22: Modeled process parameters - current density $300\ mA/cm^2$ operating pressure 50 bar

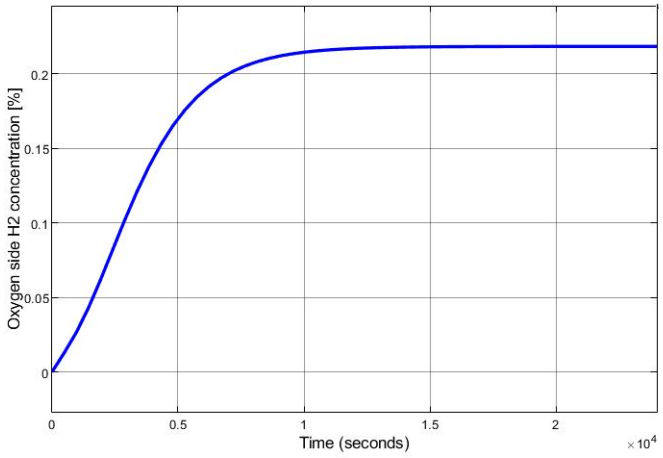

Figure 4.23: Oxygen side H_2 concentration vs time modeled with CSTR - current density $300\ mA/cm^2$ operating pressure 50 bar. Shape is not dissimilar from actual concentration course in figure 4.16, although absolute value is an order of magnitude smaller.

Pressure equalization tube configuration:	$\frac{\Phi_{H_2}^{diff,diaphragms}}{\Phi_{H_2}^{diff,PET}}$
A	$5.9 \cdot 10^5$
B	$3.8 \cdot 10^5$
C	$9.2 \cdot 10^3$

Table 4.7: Fraction of diffusional crossover through diaphragms compared to through the PET: diffusion through PET is negligible compared to through diaphragms.

Diffusion through pressure equalization tube
It would be wise to investigate the contribution of diffusion through the various tested pressure equalization tubes to H_2 crossover. This is done by comparing diffusional flux over the diaphragms to diffusional flux through the various PET.
In order to quantify this effect Fick's law for diffusion has again been utilized, under the following assumptions:

- All assumptions made to produce the CSTR model hold here as well.
- The concentration of dissolved H_2 is assumed to be at saturation level at the point where the pressure equalization tube is connected to the hydrogen side of the system.
- For simplicity sake it is modelled that this saturation concentration is presented to the full cross sectional surface area of the pressure equalization tube. As the tube to which the pressure equalization tube connects is a $6\ mm$ Swagelok tube, this is not representative of the real situation. But as in real life the saturation concentration is presented to a smaller surface area this would only decrease the calculated fraction of diffusional crossover through PET compared to through the diaphragms.

Simulation for a 16 cell stack, the results presented in table 4.7 were obtained for the three pressure equalization tube configurations.
It is observed that even in this overestimated case, crossover by solely diffusion through the PET is negligible compared to diffusion through the diaphragm. This is due to the diaphragms presenting a much larger surface area, while micro pores through the diaphragm present a much shorter pathway than any of the PET do. For this reason diffusion through the diaphragm is much more substantial than pure diffusion through the pressure equalization tube, for all three configurations.
This is of course assuming there is no flow through the pressure equalization tubes, which would be the case during off-time. As deduced earlier during operation there is indeed substantial flow through the PET. Crossover as a result of this flow through the pressure equalization tube is believed to be responsible for a large portion of the crossed-over gas, but through electrolyte mixing, and not through diffusion.

S^{sup}:	Oxygen side H_2 concentration at steady state:
1	0.24%
1.2	0.26%
1.5	0.33%
2	0.44%
4	0.87%

Table 4.8: Effect of supersaturation factor on steady-state H_2 concentration, should there only be gas crossover by diffusion.

Effect of supersaturation on crossover by diffusion
It is conceivable that supersaturation extends beyond the bubble layer, at which point the concentration of dissolved H_2 at the electrolyte diaphragm boundary exceeds saturated levels. Simulation at various levels of supersaturation has been done, to investigate its influence on crossover by diffusion. The results are presented in table 4.8. In this simulation the effect of the pressure equalization tube to crossover by diffusion is assumed to be negligible, which is a reasonable assumption as we've just demonstrated. Besides this, it is highly unlikely supersaturated levels of H_2 are presented at the connection of the pressure equalization tube and the hydrogen of the system in the first place.

What can be seen that is even for a supersaturation factor S^{sup} of 4, as defined in equation 2.55, oxygen side H_2 concentration by solely diffusion would still only provide 30% of the value for H_2 crossover obtained in experiments.
This is yet another clue that gas crossover in the ZEF AEC system is not primarily diffusion driven, but more likely to be for the larger part the result of crossover by either electrolyte mixing/permeation, or another conceivable method for foreign gas presence.

5

Conclusion & Recommendations

In this chapter, conclusions based on the obtained data are presented. The conclusions are characterized by their origin, which means they are subdivided into conclusions drawn from system character traits and from crossover traits. After that a concluding verdict on the hypothesis set ZEF CEO Jan van Kranendonk will be explicated, and recommendations will be given focused on future research in pursuit of a reduction in crossover and enlargement of the window of safe operation.

5.1. Conclusions

5.1.1. System character traits

Analysis of the data yields the following conclusions with respect to system character traits:

- Cell temperature, and with that temperature control, play an important role in maximizing efficiency. It must however be noted that for low current densities ($< 150\ mA/cm^2$) increasing the operating temperature did not directly lead to an increase in thermal efficiency, as can be observed in section 4.1.1. It is therefor believed that in order for efficiency to increase due to an increase in operating temperature, product gas production should be above a certain level.
- Increasing cell efficiency by increasing operating pressure is also only measured when production is of sufficient magnitude, as the accompanied decrease in void fraction lowers electrolyte resistance. For the ZEF AEC system this phenomena was observed at a current density of $200\ mA/cm^2$, as can be observed in section 4.1.1.
- Roughening up surface finish of nickel electrodes by sandblasting improved cell efficiency, as can be observed in section 4.1.1. An increase in thermal efficiency of 2% was measured at equal current density, operating pressure and temperature.
- Flow stagnation occurs more on the oxygen side of the system, presumably due to lower oxygen molar production compared to hydrogen, as explicated in section 4.1.1. For the same reason, flow stagnation seems to occur less at higher current densities.
- ”Noise” in gas measurement very likely to be a result of outward hydrogen diffusion, as explained in section 4.1.2.
- Pressure difference over the diaphragm never exceeds 0.4 bar when gas measurement system is utilized for pressure and level control, as shown in section 4.1.2.
- Tuning of throttling devices has been overcompensated, as system pressure drops 0.588 bar during $5000\,ms$ of hydrogen side gas measurement valve opening, compared to 1.059 bar during $1300\ ms$ of oxygen side gas measurement opening (at 50 bar and $45°C$ operating temperature).
- Upon actuation of the gas measurement valve electrolyte flow velocity, as well as pressure difference over both sides of the systems behaves as underdamped oscillation, as illustrated in section 4.1.2.

- Spike in oxygen side H_2 concentration after start-up is much less severe if pressure is maintained in the system compared to when pressure is brought back to atmospheric pressure before leaving it for the night. Argumentation for this is presented in section 4.2.2.
- Due to spike in crossover as a result of off-time, partial system operation mentioned in chapter 2.3.4 is very likely to produce unacceptable levels of crossover when system in entirety is put in use.

5.1.2. Crossover

- In terms of gas crossover for AEC systems it is concluded that indeed H_2 crossover is superior to O_2 crossover, as presented in section 4.2.
- Values for hydrogen side O_2 concentration are comparable with literature.
- For the current system, measurement "noise" in hydrogen side O_2 concentration is of same order of magnitude as possible effects on O_2 crossover, which means results are primarily conclusive in terms of safety, as deduced in section 4.2.1.
- O_2 crossover as well as H_2 crossover increases significantly with increasing operating pressure, as can be observed in the presented data in section 4.2.
- H_2 crossover through the pressure equalization tube as a result of purely diffusion is negligible compared to diffusion through the diaphragms, based on modelling results in section 4.3.1.
- Increased throttling of the outflows of the system reduce the magnitude of the peak of the differential pressure, which could possibly reduce electrolyte permeation and electrolyte mixing, and with that their contribution to gas crossover. This is deduced from findings presented in section 4.1.2.

Dominant route for crossover

- The data on pressure difference presented in section 4.1.2 shows that it's safe to assume no hydrogen in gaseous state is able to permeate through the diaphragm, as we are still far away from the 5.5 bar limit in pressure difference mentioned in literature [74]. The data presented is however not conclusive, as uncertainty in pressure sensor offset could prohibit revealing true pressure difference, which could have a substantial effect on crossover by electrolyte permeation. This uncertainty in offset is of < 0.05 bar order of magnitude, which means that the assumption of no gaseous hydrogen being able to permeate through the diaphragm is still valid.
- Modeling of H_2 crossover by diffusion showed diffusion is likely to be responsible for ~8% of the total flux of H_2 towards the oxygen side in the ZEF AEC system. Crossover is therefor assumed not to be dominated by diffusion, but by other routes of crossover in the system. The results of the model are presented in section 4.3.1.
- It is very likely that this route of crossover is indeed electrolyte mixing, as the ratio of crossover through diffusion versus electrolyte mixing is similar to reports in literature for a mixed electrolyte cycle scheme, as mentioned in section 2.3.4 [70].
- It is very likely that this mixing occurs through the pressure equalization tube, as this is the interconnect between both sides of the system. It has been demonstrated that geometry of the PET affects the oxygen side H_2 concentration, although values were of same order of magnitude for all 3 tested configurations. This is the case despite the fact that calculated volume of gas extracted per valve actuation is much smaller than inner volume of PET in configurations B and C. Electrolyte mixing contribution to H_2 crossover is therefor assumed substantial, even if mixing takes place inside the PET itself. The comparison between the three tested configurations is presented in section 4.2.4.
- The insignificant drop in crossover as a result of increased current density could indicate that contribution of electrolyte mixing to H_2 crossover is indeed significant. Increased gas production as a result of increased current density results in more frequent valve actuation, which in turn means increased electrolyte mixing as deduced in section 4.2.4.

Safety

- H_2 crossover is the main point of concern in terms of safety.
- O_2 crossover is not a point of concern in terms of safety.
- Spike in oxygen side H_2 concentration after start-up posses a threat in terms of safety.

5.1.3. Hypothesis

The hypothesis of ZEF CEO Jan van Kranendonk:
If the ZEF electrolyte cycling scheme with pressure equalization tube works as expected, then steady state experiments at an operating pressure of 20 bar will show that for a current density of $150 mA/cm^2$ the oxygen side H_2 concentration remains below 1.75% [70].

This is not true for the system without cooling installed, as at an operating pressure of 20 bar for a current density of $150\ mA/cm^2$ the oxygen side H_2 concentration mounted to 2.5% at steady-state, at a steady-state temperature of $72^{\circ}C$.

Yet, this hypothesis does hold up for the system with cooling installed, as at an operating pressure of 20 bar for a current density of $150\ mA/cm^2$ the oxygen side H_2 concentration mounted to 1.65% at steady-state, at a steady-state temperature of $45^{\circ}C$.

5.2. Recommendations

This section presents recommendations based on the knowledge and findings acquired during this research. Although the overarching goal of all recommendations is to improve safety by reducing gas crossover, the intent of the recommendations will be mentioned as they apply to different subcategories.

- A recommendation for future research is aimed at looking into the effect pressure equalization tube a bit more. The results in this study show that PET geometry does affect crossover, and interestingly a lengthier PET seems to yield greater improvement rather than a ticker PET. It is therefor suggested to test an order of magnitude longer PET to quantify its effect, and to see if the observed trend continues.
- It is recommended to investigate the possibility of keeping the system in operation all of the time. This would prohibit electrolyte from remaining in the cell for increased duration compared to during steady-state operation, at which point no spike in oxygen side H_2 concentration would be caused.
- If it's unavoidable to turn the electrolyser off from time to time, the advice is to keep off-time duration as short as possible, as well as to maintain pressure during off time, so that fraction of crossed-over gas in the buffer tanks remains lower upon start up of the system, as shown in section 4.2.2.
- As demonstrated in section 3.2.1 increased throttling decreases the pressure difference over both sides of the system. In order to minimize this dynamic term ΔP over the diaphragm it is recommended to install capillary tubes as throttling devices in the gas measurement setup. This will make the system "breathe" even smoother, as well as increase precision in throttling the outflows compared to the current needle valves. The idea behind this recommendation is that crossover by diffusion will always happen, but crossover by convection can be minimized by smart design and control.
- In order to improve the current gas measurement setup it is recommended to reduce sensor housing volume. This could improve measurements, as time to flush the housings would be reduced, which means measured values resemble composition flowing from the stack quicker than currently the case.
- In name of safety temperature control is very important. Although high temperature is beneficial in terms of efficiency as cell resistance lowers (should current density be above certain level), it is also accompanied with greater H_2 crossover as demonstrated in section 4.2.2. It is therefor

conceivable that there is a sweet spot in operation. In this sweet spot the current density is set to the specified required production rate, and temperature is set to the highest possible value which would keep the oxygen side H_2 concentration just below the 50% LEL safety limit. At this point, efficiency is maximized while meeting design requirements in terms of safety and production rate, but it can only be obtained if temperature control is implemented in the ZEF AEC system. Further research is then required to find this optimal operating temperature at certain current densities.

Special note:

- In the very final stages of this research an additional source for foreign gas species production was hypothesized. It takes into account that in the current ZEF AEC system the total potential difference is applied at either stack end-plates. This could in theory polarize the electrolyte present in the inlet and exhaust manifolds as these are in direct contact with the stack end-plates, which could lead to stray gas production at all interfaces where a potential difference is observed. This is not gas crossover in the literal sense, but could still contribute to the foreign gas species concentration and affect product gas purity. The timeframe of this research unfortunately prohibited further investigation into this hypotheses. Yet, stack configurations which could influence this channel electrolyte polarization are conceivable. Further research is therefor recommended to investigate the contribution of stray gas production to the foreign gas species concentrations.

Bibliography

[1] 2001. URL https://www.engineeringtoolbox.com/.

[2] Psu, May 2016. URL https://www.promolding.nl/psu/.

[3] MA Al-Saleh, S Gultekin, AS Al-Zakri, and H Celiker. Performance of porous nickel electrode for alkaline h2/o2 fuel cell. *International journal of hydrogen energy*, 19(8):713–718, 1994.

[4] AJ Appleby, G Crepy, and J Jacquelin. High efficiency water electrolysis in alkaline solution. *International Journal of Hydrogen Energy*, 3(1):21–37, 1978.

[5] Samuel Simon Araya, Vincenzo Liso, Xiaoti Cui, Na Li, Jimin Zhu, Simon Lennart Sahlin, Søren Højgaard Jensen, Mads Pagh Nielsen, and Søren Knudsen Kær. A review of the methanol economy: the fuel cell route. *Energies*, 13(3):596, 2020.

[6] J Balej. Water vapour partial pressures and water activities in potassium and sodium hydroxide solutions over wide concentration and temperature ranges. *International journal of hydrogen energy*, 10(4):233–243, 1985.

[7] Allen J Bard, Larry R Faulkner, et al. Fundamentals and applications. *Electrochemical Methods*, 2(482):580–632, 2001.

[8] Pratik Basarkar. Experimental characterization of a novel small-scale natural circulation loop methanol synthesis reactor. 2018.

[9] Martin Johan Bos and Derk Willem Frederik Brilman. A novel condensation reactor for efficient co2 to methanol conversion for storage of renewable electric energy. *Chemical Engineering Journal*, 278:527–532, 10 2015. ISSN 1385-8947. doi: 10.1016/j.cej.2014.10.059.

[10] Jörn Brauns and Thomas Turek. Alkaline water electrolysis powered by renewable energy: A review. *Processes*, 8(2):248, 2020.

[11] Alejandro N Colli, Hubert H Girault, and Alberto Battistel. Non-precious electrodes for practical alkaline water electrolysis. *Materials*, 12(8):1336, 2019.

[12] Christophe Coutanceau, Stève Baranton, and Thomas Audichon. *Hydrogen electrochemical production*. Academic Press, 2017.

[13] Ilias Daniil. Transient modeling and control of a small-scale and self-pressurized electrolysis system. 2021.

[14] RE Davis, GL Horvath, and CW Tobias. The solubility and diffusion coefficient of oxygen in potassium hydroxide solutions. *Electrochimica Acta*, 12(3):287–297, 1967.

[15] HJ De Wane and WJ Hamer. Electrochemical data. part 10-electrolytic conductivity of aqueous solutions of the alkali metal hydroxides. 1968.

[16] A Djafour, M Matoug, H Bouras, B Bouchekima, MS Aida, and B Azoui. Photovoltaic-assisted alkaline water electrolysis: Basic principles. *international journal of hydrogen energy*, 36(6):4117–4124, 2011.

[17] Zsolt Dobó and Árpád Bence Palotás. Impact of the current fluctuation on the efficiency of alkaline water electrolysis. *International Journal of Hydrogen Energy*, 42(9):5649–5656, 2017.

[18] Deszoe Dobos. *A handbook for electrochemists in industry and universities*. Elsevier, 1975.

[19] John Eigeldinger and Helmut Vogt. The bubble coverage of gas-evolving electrodes in a flowing electrolyte. *Electrochimica Acta*, 45(27):4449–4456, 2000.

[20] RB Evans III, GM Watson, and EA Mason. Gaseous diffusion in porous media at uniform pressure. *The journal of chemical physics*, 35(6):2076–2083, 1961.

[21] Moira Fagan and Christine Huang. A look at how people around the world view climate change, Apr 2019. URL `https://www.pewresearch.org/fact-tank/2019/04/18/a-look-at-how-people-around-the-world-view-climate-change/`.

[22] RJ Gilliam, JW Graydon, DW Kirk, and SJ Thorpe. A review of specific conductivities of potassium hydroxide solutions for various concentrations and temperatures. *International Journal of Hydrogen Energy*, 32(3):359–364, 2007.

[23] SD Hamann and Max Linton. Electrical conductivities of aqueous solutions of kcl, koh and hcl, and the ionization of water at high shock pressures. *Transactions of the Faraday Society*, 65: 2186–2196, 1969.

[24] Philipp Haug, Matthias Koj, and Thomas Turek. Influence of process conditions on gas purity in alkaline water electrolysis. *International Journal of Hydrogen Energy*, 42(15):9406–9418, 2017.

[25] Isaac Herraiz-Cardona, E Ortega, J García Antón, and Valentín Pérez-Herranz. Assessment of the roughness factor effect and the intrinsic catalytic activity for hydrogen evolution reaction on ni-based electrodeposits. *International journal of hydrogen energy*, 36(16):9428–9438, 2011.

[26] W Hug, J Divisek, J Mergel, W Seeger, and H Steeb. Highly efficient advanced alkaline electrolyzer for solar operation. *International journal of hydrogen energy*, 17(9):699–705, 1992.

[27] LJJ Janssen. Effective solution resistivity in beds containing one monolayer or multilayers of uniform spherical glass beads. *Journal of Applied Electrochemistry*, 30(4):507–509, 2000.

[28] Wenbo Ju, Meike VF Heinz, Lorenzo Pusterla, Matthias Hofer, Benjamin Fumey, Roberto Castiglioni, Marco Pagani, Corsin Battaglia, and Ulrich F Vogt. Lab-scale alkaline water electrolyzer for bridging material fundamentals with realistic operation. *ACS Sustainable Chemistry & Engineering*, 6(4):4829–4837, 2018.

[29] Mahdi Kiaee, Andrew Cruden, David Infield, and Petr Chladek. Utilisation of alkaline electrolysers to improve power system frequency stability with a high penetration of wind power. *IET Renewable Power Generation*, 8(5):529–536, 2013.

[30] Kenji Kikuchi, Hiroko Takeda, Beatrice Rabolt, Takuji Okaya, Zempachi Ogumi, Yasuhiro Saihara, and Hiroyuki Noguchi. Hydrogen particles and supersaturation in alkaline water from an alkali–ion–water electrolyzer. *Journal of Electroanalytical Chemistry*, 506(1):22–27, 2001.

[31] Tom Kleist. Characterisation of flow and bubble phenomena in a high pressure alkaline water electrolyser. 2021.

[32] MA Klochko and MM Godneva. Electrical conductivity and viscosity of aqueous solutions of naoh and koh. *Russ. J. Inorg. Chem*, 4:964–967, 1959.

[33] F Körösy. Two rules concerning solubility of gases and crude data on solubility of krypton. *Transactions of the Faraday Society*, 33:416–425, 1937.

[34] Mikkel Rykær Kraglund, Marcelo Carmo, Günter Schiller, Syed Asif Ansar, David Aili, Erik Christensen, and Jens Oluf Jensen. Ion-solvating membranes as a new approach towards high rate alkaline electrolyzers. *Energy & Environmental Science*, 12(11):3313–3318, 2019.

[35] Michael Krenz. *Untersuchung des elektrodennahen Raumes gasentwickelnder Elektroden*. PhD thesis, Verlag nicht ermittelbar, 1984.

[36] NV Kuleshov, VN Kuleshov, SA Dovbysh, E Ya Udris, SA Grigor'ev, Yu A Slavnov, and LA Korneeva. Polymeric composite diaphragms for water electrolysis with alkaline electrolyte. *Russian Journal of Applied Chemistry*, 89(4):618–621, 2016.

[37] Parveen Kumar and S Yashonath. Ionic conductivity in aqueous electrolyte solutions: Insights from computer simulations. *Journal of Molecular Liquids*, 277:506–515, 2019.

[38] Kirill Igorevich Kuznetsov, Sergei Vladimirovich Skorodumov, and Pavel Pavlovich Granchenko. Measurements of the dynamic viscosity and density of koh solutions at atmospheric pressure. *High Temperature*, 58(6):806–811, 2020.

[39] B Laoun. Thermodynamics aspect of high pressure hydrogen production by water electrolysis. *Revue des energies renouvelables*, 10(3):435–444, 2007.

[40] Damien Le Bideau, Philippe Mandin, Mohamed Benbouzid, Myeongsub Kim, and Mathieu Sellier. Review of necessary thermophysical properties and their sensivities with temperature and electrolyte mass fractions for alkaline water electrolysis multiphysics modelling. *International Journal of Hydrogen Energy*, 44(10):4553–4569, 2019.

[41] YS Li, TS Zhao, and Rong Chen. Cathode flooding behaviour in alkaline direct ethanol fuel cells. *Journal of power sources*, 196(1):133–139, 2011.

[42] Akiyoshi Manabe, M Kashiwase, T Hashimoto, T Hayashida, A Kato, Kazuhiro Hirao, Ikuo Shimomura, and Ikuo Nagashima. Basic study of alkaline water electrolysis. *Electrochimica Acta*, 100: 249–256, 2013.

[43] E. Marrasso, C. Roselli, and M. Sasso. Electric efficiency indicators and carbon dioxide emission factors for power generation by fossil and renewable energy sources on hourly basis. *Energy Conversion and Management*, 196:1369 – 1384, 2019. ISSN 0196-8904. doi: https://doi.org/10.1016/j.enconman.2019.06.079. URL http://www.sciencedirect.com/science/article/pii/S0196890419307496.

[44] Hisayoshi Matsushima, Daisuke Kiuchi, and Yasuhiro Fukunaka. Measurement of dissolved hydrogen supersaturation during water electrolysis in a magnetic field. *Electrochimica Acta*, 54(24): 5858–5862, 2009.

[45] Hisayoshi Matsushima, Takami Iida, and Yasuhiro Fukunaka. Observation of bubble layer formed on hydrogen and oxygen gas-evolving electrode in a magnetic field. *Journal of Solid State Electrochemistry*, 16(2):617–623, 2012.

[46] Keith Oldham and Jan Myland. *Fundamentals of electrochemical science*. Elsevier, 2012.

[47] Bhupender Pal, Shengyuan Yang, Subramaniam Ramesh, Venkataraman Thangadurai, and Rajan Jose. Electrolyte selection for supercapacitive devices: a critical review. *Nanoscale Advances*, 1(10):3807–3835, 2019.

[48] Robert Phillips and Charles W Dunnill. Zero gap alkaline electrolysis cell design for renewable energy storage as hydrogen gas. *RSC advances*, 6(102):100643–100651, 2016.

[49] Derek Pletcher and Xiaohong Li. Prospects for alkaline zero gap water electrolysers for hydrogen production. *International Journal of Hydrogen Energy*, 36(23):15089–15104, 2011.

[50] John M Prausnitz, Rudiger N Lichtenthaler, and Edmundo Gomes De Azevedo. *Molecular thermodynamics of fluid-phase equilibria*. Pearson Education, 1998.

[51] Paola Quaino, Fernanda Juarez, Elizabeth Santos, and Wolfgang Schmickler. Volcano plots in hydrogen electrocatalysis–uses and abuses. *Beilstein journal of nanotechnology*, 5(1):846–854, 2014.

[52] Sona Raeissi and Cor J Peters. Understanding temperature dependency of hydrogen solubility in ionic liquids, including experimental data in [bmim][tf2n]. *AIChE journal*, 58(11):3553–3559, 2012.

[53] Md Mamoon Rashid, Mohammed K Al Mesfer, Hamid Naseem, Mohd Danish, et al. Hydrogen production by water electrolysis: a review of alkaline water electrolysis, pem water electrolysis and high temperature water electrolysis. *Int. J. Eng. Adv. Technol*, 4(3):2249–8958, 2015.

[54] Christian Redl, Fabian Hein, Matthias Buck, Patrick Graichen, and Dave Jones. Agora energiewende and sandbag (2020): The european power sector in 2019: Up-to-date analysis on the electricity transition. *www.agora-energiewende.de*, Mar 2020. URL https://www.agora-energiewende.de/fileadmin2/Projekte/2019/Jahresauswertung_EU_2019/172_A-EW_EU-Annual-Report-2019_Web.pdf.

[55] Amitava Roy, Simon Watson, and David Infield. Comparison of electrical energy efficiency of atmospheric and high-pressure electrolysers. *International Journal of Hydrogen Energy*, 31(14): 1964–1979, 2006.

[56] P Ruetschi and RF Amlie. Solubility of hydrogen in potassium hydroxide and sulfuric acid. salting-out and hydration. *The Journal of Physical Chemistry*, 70(3):718–723, 1966.

[57] Hiroyuki Sato and Xing L. Yan. Study of an htgr and renewable energy hybrid system for grid stability. *Nuclear Engineering and Design*, 343:178–186, 2019. doi: 10.1016/j.nucengdes.2019.01.010.

[58] Maximilian Schalenbach, Wiebke Lueke, and Detlef Stolten. Hydrogen diffusivity and electrolyte permeability of the zirfon perl separator for alkaline water electrolysis. *Journal of the Electrochemical Society*, 163(14):F1480, 2016.

[59] Maximilian Schalenbach, Olga Kasian, and Karl JJ Mayrhofer. An alkaline water electrolyzer with nickel electrodes enables efficient high current density operation. *International Journal of Hydrogen Energy*, 43(27):11932–11938, 2018.

[60] Volkmar Schröder and Kai Holtappels. Explosion characteristics of hydrogen-air and hydrogen-oxygen mixtures at elevated pressures. In *International Conference on hydrogen safety, Congress Palace, Pisa, Italy*, 2005.

[61] CA Schug. Operational characteristics of high-pressure, high-efficiency water-hydrogen-electrolysis. *International journal of hydrogen energy*, 23(12):1113–1120, 1998.

[62] Adrian Schumpe. The estimation of gas solubilities in salt solutions. *Chemical engineering science*, 48(1):153–158, 1993.

[63] Marc-Alexander Schwarze. Controlled removal of trace o2 in an h2 environment of a small-scale electrolyser. 2020.

[64] Dawn M See and Ralph E White. Temperature and concentration dependence of the specific conductivity of concentrated solutions of potassium hydroxide. *Journal of Chemical & Engineering Data*, 42(6):1266–1268, 1997.

[65] Tatsuya Shinagawa, Angel T Garcia-Esparza, and Kazuhiro Takanabe. Insight on tafel slopes from a microkinetic analysis of aqueous electrocatalysis for energy conversion. *Scientific reports*, 5:13801, 2015.

[66] SK Shoor, Robert Dixon Walker Jr, and KE Gubbins. Salting out of nonpolar gases in aqueous potassium hydroxide solutions. *The Journal of Physical Chemistry*, 73(2):312–317, 1969.

[67] Pal M Sipos, Glenn Hefter, and Peter M May. Viscosities and densities of highly concentrated aqueous moh solutions (m+= na+, k+, li+, cs+,(ch3) 4n+) at 25.0° c. *Journal of Chemical & Engineering Data*, 45(4):613–617, 2000.

[68] Friedrich-W Speckmann, Steffen Bintz, and Kai Peter Birke. Influence of rectifiers on the energy demand and gas quality of alkaline electrolysis systems in dynamic operation. *Applied Energy*, 250:855–863, 2019.

[69] Min J Tham, Robert Dixon Walker Jr, and Keith E Gubbins. Diffusion of oxygen and hydrogen in aqueous potassium hydroxide solutions. *The Journal of Physical Chemistry*, 74(8):1747–1751, 1970.

[70] P Trinke, P Haug, J Brauns, B Bensmann, R Hanke-Rauschenbach, and T Turek. Hydrogen crossover in pem and alkaline water electrolysis: mechanisms, direct comparison and mitigation strategies. *Journal of The Electrochemical Society*, 165(7):F502, 2018.

[71] Daniel van Laake. Development and characterization of a small scale methanol synthesis reactor based on natural convection. 2019.

[72] Ph Vermeiren, W Adriansens, and R Leysen. Zirfon®: A new separator for ni□ h2 batteries and alkaline fuel cells. *International journal of hydrogen energy*, 21(8):679–684, 1996.

[73] Ph Vermeiren, W Adriansens, JP Moreels, and R Leysen. The composite zirfon® separator for alkaline water electrolysis. In *Hydrogen power: theoretical and engineering solutions*, pages 179–184. Springer, 1998.

[74] Ph Vermeiren, W Adriansens, JP Moreels, and R Leysen. Evaluation of the zirfon® separator for use in alkaline water electrolysis and ni-h2 batteries. *International Journal of Hydrogen Energy*, 23(5):321–324, 1998.

[75] Mingyong Wang, Zhi Wang, Xuzhong Gong, and Zhancheng Guo. The intensification technologies to water electrolysis for hydrogen production–a review. *Renewable and Sustainable Energy Reviews*, 29:573–588, 2014.

[76] Wei Xing, Min Yin, Qing Lv, Yang Hu, Changpeng Liu, and Jiujun Zhang. Oxygen solubility, diffusion coefficient, and solution viscosity. In *Rotating electrode methods and oxygen reduction electrocatalysts*, pages 1–31. Elsevier, 2014.

[77] Kai Zeng and Dongke Zhang. Recent progress in alkaline water electrolysis for hydrogen production and applications. *Progress in energy and combustion science*, 36(3):307–326, 2010.

[78] Houcheng Zhang, Guoxing Lin, and Jincan Chen. Evaluation and calculation on the efficiency of a water electrolysis system for hydrogen production. *international journal of hydrogen energy*, 35 (20):10851–10858, 2010.

A

Appendix

A.1. Cathode: rate determining step electric current derivation

Cathode - HER

At the cathode, water is being reduced according to three steps, with M as electrode surface empty site [65]:

$$\text{(Volmer step)} \qquad H_2O + e^- + M \rightleftharpoons \mathrm{M}\text{——}\mathrm{H} + OH^- \tag{A.1}$$

$$\text{(Tafel step)} \qquad 2\,\mathrm{M}\text{——}\mathrm{H} \rightleftharpoons H_2 + 2M \tag{A.2}$$

$$\text{(Heyrovsky step)} \qquad \mathrm{M}\text{——}\mathrm{H} + H_2O + e^- \rightleftharpoons H_2 + OH^- + M \tag{A.3}$$

For each of the steps the forward reaction rates can be determined. If then the overall reaction rate is considered, the rate determining step can be identified. The forward reaction rates of each step can be determined with [65]:

$$\text{(Volmer step forward reaction rate)} \qquad r_{A.1} = k_{A.1} a_{H_2O}(1 - \theta_{H_2}) \tag{A.4}$$

$$\text{(Tafel step foward reaction rate)} \qquad r_{A.2} = k^0_{A.2} \theta^2_{H_2} \tag{A.5}$$

$$\text{(Heyrovsky step foward reaction rate)} \qquad r_{A.3} = k_{A.3} a_{H_2O} \theta_{H_2} \tag{A.6}$$

In these equations, r_j is the reaction rate and k_j is the kinetic rate constant for equation j, while a_{H_2O} is the water ion activity and θ_{H_2} the surface coverage ratio by hydrogen.

If the **Volmer step** is rate determining, equation A.4 determines the HER rates. Because the Volmer step is an electron transfer step the kinetic rate constant k_j depends on the applied potential and resulting overpotential η_j according to equation A.7 [65], with k_0 as standard rate constant:

$$k_j = k^0_j e^{\frac{-\alpha_j \eta_j F}{RT}} \tag{A.7}$$

When the Volmer step is the rate determining step, the adsorbed hydrogen consumption rates, equations A.5 and A.6, will be higher, which makes it reasonable to assume that the hydrogen coverage ratio θ_{H_2} goes to zero [65]. Equation A.4 becomes equation A.8.

$$\text{(Volmer step forward reaction rate)} \qquad r_{A.1} = k^0_{A.1} a_{H_2O} e^{\frac{-\alpha_{A.1} \eta_{A.1} F}{RT}} \tag{A.8}$$

As the electric current I is proportional to the reaction rate r, equation A.9 can be observed, with number of electrons involved n, Faradays constant F(charge per electron) and electrode surface area A.

$$I = nFAr \tag{A.9}$$

Inserting equation A.8 into A.9 yields equation A.10 as expression for the electric current when the Volmer step is rate determining.

$$I = nFAk^0_{A.1} a_{H_2O} e^{\frac{-\alpha_{A.1}\eta_{A.1}F}{RT}} \tag{A.10}$$

In the case that the **Tafel step** is rate determining, the Volmer step will reach equilibrium before this rate limit is reached [65]. This means forward reaction and reverse reaction rates of reaction A.1 are equal.

$$\text{(Volmer step reverse reaction rate)} \qquad r_{-A.1} = k_{-A.1} a_{OH^-} \theta_{H_2} \tag{A.11}$$

$$r_{A.1} = r_{-A.1} \tag{A.12}$$

If now A.12 is rewritten, using the relations A.13 and A.7 for the reverse kinetic rate constant $k_{-A.1}$ and forward kinetic rate constant $k_{A.1}$ respectively, the following expression for the coverage ratio θ_{H_2} can be found.

$$k_{-j} = k^0_{-j} e^{\frac{(1-\alpha_j)\eta_j F}{RT}} \tag{A.13}$$

$$\theta_{H_2} = \frac{k^0_{A.1} a_{H_2O}}{k^0_{-A.1} a_{OH^-} e^{\frac{\eta_{A.1}F}{RT}} + k^0_{A.1} a_{H_2O}} \tag{A.14}$$

Implementation of the Tafel step forward reaction rate equation A.5 and coverage ratio equation A.14 into equation A.9 yields the following expression for the electric current when the Tafel step is rate determining:

$$I = nFAk^0_{A.2} \left(\frac{k^0_{A.1} a_{H_2O}}{k^0_{-A.1} a_{OH^-} e^{\frac{\eta_{A.1}F}{RT}} + k^0_{A.1} a_{H_2O}} \right)^2 \tag{A.15}$$

Should the **Heyrovsky step** be rate determining, again pre-equilibration of the Volmer step occurs before rate limit is reached by Heyrovski step. If now equations A.6 and A.14 are inserted into equation A.9, the following expression for the electric current for when the Heyrovsky step is rate determining is obtained:

$$I = nFA \frac{k^0_{A.3} k^0_{A.1} a^2_{H_2O} e^{\frac{-\alpha_{A.3}\eta_{A.3}F}{RT}}}{k^0_{-A.1} a_{OH^-} e^{\frac{\eta_{A.1}F}{RT}} + k^0_{A.1} a_{H_2O}} \tag{A.16}$$

A.2. Anode: rate determining step electric current derivation

Anode - OER

On the anode surface, oxygen evolution reaction OER happens according to a 5 step process, assuming a single-site reaction mechanism [65]:

$$\text{(Step 1)} \qquad M + OH^- \rightleftharpoons MOH + e^- \tag{A.17}$$

$$\text{(Step 2)} \qquad MOH + OH^- \rightleftharpoons MO + H_2O + e^- \tag{A.18}$$

$$\text{(Step 3)} \qquad MO + OH^- \rightleftharpoons MOOH + e^- \tag{A.19}$$

$$\text{(Step 4)} \qquad MOOH + OH^- \rightleftharpoons MOO^- + H_2O \tag{A.20}$$

$$\text{(Step 5)} \qquad MOO^- \rightleftharpoons M + O_2 + e^- \tag{A.21}$$

If **step 1** is the rate limiting step, the reaction can be described as follows:

$$r_{A.17} = k_{A.17} a_{OH^-} \theta_M \tag{A.22}$$

As M are again empty electrode surface sites, θ_M is in this case the ratio of empty site surface coverage. If step 1 is indeed rate limiting, it is reasonable to assume that consumption of adsorbed species is larger than adsorption rate itself. This means the empty site coverage is high, i.e. $\theta_M \approx 1$ [65]. As this oxidation reaction is again an electron transfer step, kinetic rate constant equations A.7 and A.13 apply here as well, the only difference being that now an electron is passed on instead of taken up. This means signs are switched, yielding equations A.23 and A.24. Implementing A.23 and A.22 into A.9 yields equation A.25 for the electric current.

$$k_j = k_j^0 e^{\frac{(1-\alpha_j)\eta_j F}{RT}} \tag{A.23}$$

$$k_{-j} = k_{-j}^0 e^{\frac{-\alpha_j \eta_j F}{RT}} \tag{A.24}$$

$$I = nFAk_{A.17}^0 a_{OH^-} \theta_M e^{\frac{(1-\alpha_{A.17})\eta_{A.17} F}{RT}} = nFAk_{A.17}^0 a_{OH^-} e^{\frac{(1-\alpha_{A.17})\eta_{A.17} F}{RT}} \tag{A.25}$$

If **step 2** is the rate limiting step, step 1 will pre-equilibrate before the limit is reached. This means forward and reverse reaction rates are equal [65].

$$r_{A.17} = r_{-A.17} \tag{A.26}$$

$$r_{-A.17} = k_{-A.17} \theta_{MOH} \tag{A.27}$$

If now equations A.22 and A.27 are inserted into equation A.26 taking equation A.7 into consideration, equation A.28 can be obtained.

$$\theta_M = \frac{k_{-A.17}^0 \theta_{MOH}}{k_{A.17}^0 a_{OH^-} e^{\frac{\eta_{A.17} F}{RT}}} \tag{A.28}$$

If step 2 is indeed rate limiting, the surface of the anode will predominantly be covered by either empty sites, or by MOH sites [65]. Therefor, the following assumption is made:

$$\theta_M + \theta_{MOH} = 1 \tag{A.29}$$

Rewriting of equation A.29 and insertion of A.28 yields the following:

$$\theta_{MOH} = \frac{k^0_{A.17} a_{OH^-} e^{\frac{\eta_{A.17} F}{RT}}}{k^0_{A.17} a_{OH^-} e^{\frac{\eta_{A.17} F}{RT}} + k^0_{-A.17}} \tag{A.30}$$

We can now insert A.30 into the step 2 reaction rate equation A.31, and with that obtain the electric current relation equation A.32.

$$r_{A.18} = k_{A.18} a_{OH^-} \theta_{MOH} \tag{A.31}$$

$$I = nFA \frac{k^0_{A.17} k^0_{A.18} e^{\frac{\eta_{A.17} F}{RT}} e^{\frac{(1-\alpha_{A.18})\eta_{A.18} F}{RT}} a^2_{OH^-}}{k^0_{A.17} e^{\frac{\eta_{A.17} F}{RT}} a_{OH^-} + k^0_{-A.17}} \tag{A.32}$$

If **step 3** is the rate limiting step, not only step 1 but also step 2 will be pre-equilibrated. This means equations A.26 and A.30 are still valid, and are supplemented with the equations A.33 and A.34 [65].

$$r_{A.18} = r_{-A.18} \tag{A.33}$$

$$r_{-A.18} = k_{-A.18} a_{H_2O} \theta_{MO} \tag{A.34}$$

Insertion of A.31 and A.34 into A.33 taking A.7 into consideration will yield equation A.35.

$$\theta_{MOH} = \frac{k^0_{-A.18} a_{H_2O}}{k^0_{A.18} a_{OH^-} e^{\frac{\eta_{A.18} F}{RT}}} \theta_{MO} \tag{A.35}$$

If step 3 is rate limiting, the surface of the electrode will mostly be covered by either empty sites, MOH or MO sites. This means the following assumption can be made:

$$\theta_M + \theta_{MOH} + \theta_{MO} = 1 \tag{A.36}$$

Rewriting equation A.36 and insertion of A.28 and A.35 yields:

$$\theta_{MO} = \frac{k^0_{A.17} k^0_{A.18} a^2_{OH^-} e^{\frac{(\eta_{A.17}+\eta_{A.18})F}{RT}}}{k^0_{-A.18} a_{H_2O} (k^0_{-A.17} + k^0_{A.17} a_{OH^-} e^{\frac{\eta_{A.17} F}{RT}}) + k^0_{A.17} k^0_{A.18} a^2_{OH^-} e^{\frac{(\eta_{A.17}+\eta_{A.18})F}{RT}}} \tag{A.37}$$

Inserting step 3 forward reaction rate equation A.38 and MO coverage ratio equation A.37 into equation A.9, the following current relationship is obtained.

$$r_{A.19} = k_{A.19} a_{OH^-} \theta_{MO} \tag{A.38}$$

$$I = nFA \frac{k^0_{A.17} k^0_{A.18} k^0_{A.19} e^{\frac{(\eta_{A.17}+\eta_{A.18})F}{RT}} e^{\frac{(1-\alpha_{A.19})\eta_{A.19} F}{RT}} a^3_{OH^-}}{k^0_{-A.18} a_{H_2O} (k^0_{-A.17} + k^0_{A.17} a_{OH^-} e^{\frac{\eta_{A.17} F}{RT}}) + k^0_{A.17} k^0_{A.18} a^2_{OH^-} e^{\frac{(\eta_{A.17}+\eta_{A.18})F}{RT}}} \tag{A.39}$$

If **step 4** is the rate limiting step, the same method applies as before. Now not only step 1 and 2 but also step 3 will be pre-equilibrated. This means equations A.26, A.28, A.33 and A.35 are still valid, and are supplemented with the equations A.40 and A.41 [65].

$$r_{A.19} = r_{-A.19} \tag{A.40}$$

$$r_{-A.19} = k_{-A.19} \theta_{MOOH} \tag{A.41}$$

Substituting A.38 and A.41 in A.40 and rewriting gives:

$$\theta_{MO} = \frac{k^0_{-A.19}\theta_{MOOH}}{a_{OH^-}k^0_{A.19}e^{\frac{\eta_{A.19}F}{RT}}} \tag{A.42}$$

And just like before, the summation of the coverage ratios is assumed to be equal to 1.

$$\theta_M + \theta_{MOH} + \theta_{MO} + \theta_{MOOH} = 1 \tag{A.43}$$

Rewriting of equation A.43 and insertion of A.28, A.35 and A.42 yields:

$$\theta_{MOOH} = \frac{k^0_{A.17}k^0_{A.18}k^0_{A.19}e^{\frac{(\eta_{A.17}+\eta_{A.18}+\eta_{A.19})F}{RT}}a^3_{OH^-}}{k^0_{A.17}k^0_{A.18}k^0_{A.19}e^{\frac{(\eta_{A.17}+\eta_{A.18}+\eta_{A.19})F}{RT}}a^3_{OH^-} + k^0_{-A.17}k^0_{-A.18}k^0_{-A.19}a_{H_2O} + k^0_{A.17}k^0_{-A.18}k^0_{-A.19}e^{\frac{\eta_{A.17}F}{RT}}a_{OH^-}a_{H_2O} + k^0_{A.17}k^0_{A.18}k^0_{-A.19}e^{\frac{(\eta_{A.17}+\eta_{A.18})F}{RT}}a^2_{OH^-}} \tag{A.44}$$

Because this is not an electron transfer step, the kinetic rate constant does not depend on the applied potential. This means the kinetic rate constant in reaction rate equation A.45 is the standard rate constant $k^0_{A.20}$ for this reaction. Considering the step 4 forward reaction rate A.45, this leads to the following relationship for the electric current:

$$r_{A.20} = k^0_{A.20}a_{OH^-}\theta_{MOOH} \tag{A.45}$$

$$I = nFA\frac{k^0_{A.17}k^0_{A.18}k^0_{A.19}k^0_{A.20}e^{\frac{(\eta_{A.17}+\eta_{A.18}+\eta_{A.19})F}{RT}}a^4_{OH^-}}{k^0_{A.17}k^0_{A.18}k^0_{A.19}a^3_{OH^-}e^{\frac{(\eta_{A.17}+\eta_{A.18}+\eta_{A.19})F}{RT}} + k^0_{-A.17}k^0_{-A.18}k^0_{-A.19}a_{H_2O} + k^0_{A.17}k^0_{-A.18}k^0_{-A.19}e^{\frac{\eta_{A.17}F}{RT}}a_{OH^-}a_{H_2O} + k^0_{A.17}k^0_{A.18}k^0_{-A.19}e^{\frac{(\eta_{A.17}+\eta_{A.18})F}{RT}}a^2_{OH^-}} \tag{A.46}$$

If **step 5** is the rate limiting step, once again the same method applies. Now not only step 1, 2 and 3 but also step 4 will be pre-equilibrated. This means equations A.26, A.28, A.33, A.35, A.40 and A.42 are still valid, and are supplemented with the equations A.47 and A.47 [65].

$$r_{A.20} = r_{-A.20} \tag{A.47}$$

$$r_{-A.20} = k^0_{-A.20}a_{H_2O}\theta_{MOO^-} \tag{A.48}$$

Substitution of A.45 and A.48 in A.47 and rewriting yields equation A.49.

$$\theta_{MOOH} = \frac{k^0_{-A.20}a_{H_2O}}{k^0_{A.20}a_{OH^-}}\theta_{MOO^-} \tag{A.49}$$

The sum of the coverage ratios is once again equal to 1:

$$\theta_M + \theta_{MOH} + \theta_{MO} + \theta_{MOOH} + \theta_{MOO^-} = 1 \tag{A.50}$$

Implementing A.28, A.35, A.42 and A.49 into equation A.50 and rewriting results in the following:

$$\theta_{MOO^-} = \frac{k^0_{A.17}k^0_{A.18}k^0_{A.19}k^0_{A.20}e^{\frac{(\eta_{A.17}+\eta_{A.18}+\eta_{A.19})F}{RT}}a^4_{OH^-}}{k^0_{A.17}k^0_{A.18}k^0_{A.19}k^0_{A.20}e^{\frac{(\eta_{A.17}+\eta_{A.18}+\eta_{A.19})F}{RT}}a^4_{OH^-} + k^0_{-A.17}k^0_{-A.18}k^0_{-A.19}k^0_{-A.20}a^2_{H_2O} + k^0_{A.17}k^0_{-A.18}k^0_{-A.19}k^0_{-A.20}e^{\frac{\eta_{A.17}F}{RT}}a^2_{H_2O}a_{OH^-} + k^0_{A.17}k^0_{A.18}k^0_{-A.19}k^0_{-A.20}e^{\frac{(\eta_{A.17}+\eta_{A.18})F}{RT}}a_{H_2O}a^2_{OH^-} + k^0_{A.17}k^0_{A.18}k^0_{A.19}k^0_{-A.20}e^{\frac{(\eta_{A.17}+\eta_{A.18}+\eta_{A.19})F}{RT}}a_{H_2O}a^3_{OH^-}} \tag{A.51}$$

If now the step 5 forward reaction rate A.52 is considered, the following relationship for the electric current can be found:

$$r_{A.21} = k_{A.21}\theta_{MOO^-} \tag{A.52}$$

$$I = nFA\frac{k^0_{A.17}k^0_{A.18}k^0_{A.19}k^0_{A.20}k^0_{A.21}e^{\frac{(\eta_{A.17}+\eta_{A.18}+\eta_{A.19})F}{RT}}e^{\frac{(1-\alpha_{A.21})\eta_{A.21}F}{RT}}a^4_{OH^-}}{k^0_{A.17}k^0_{A.18}k^0_{A.19}k^0_{A.20}e^{\frac{(\eta_{A.17}+\eta_{A.18}+\eta_{A.19})F}{RT}}a^4_{OH^-} + k^0_{-A.17}k^0_{-A.18}k^0_{-A.19}k^0_{-A.20}a^2_{H_2O} + k^0_{A.17}k^0_{-A.18}k^0_{-A.19}k^0_{-A.20}e^{\frac{\eta_{A.17}F}{RT}}a^2_{H_2O}a_{OH^-} + k^0_{A.17}k^0_{A.18}k^0_{-A.19}k^0_{-A.20}e^{\frac{(\eta_{A.17}+\eta_{A.18})F}{RT}}a_{H_2O}a^2_{OH^-} + k^0_{A.17}k^0_{A.18}k^0_{A.19}k^0_{-A.20}e^{\frac{(\eta_{A.17}+\eta_{A.18}+\eta_{A.19})F}{RT}}a_{H_2O}a^3_{OH^-}} \tag{A.53}$$

A.3. Evikon O_2 sensor specification sheet

Evikon Sensor Technologies
Measurement & Control Instrumentation

Updated 09.03.2020

IP65 | 4-20 mA 0-10 V | RS485 Modbus

Oxygen Transmitter
E2618-O2

Features

- Wall-mount or duct-mount version
- Industrial IP65 housing
- Two analog outputs settable to 4-20 mA or 0-10 V
- RS485 Modbus RTU digital interface
- Attached or remote sensor
- LCD indicator option

Specifications

Calibration	oxygen O_2
Sensor type	electrochemical or optical (fluorescence quenching based; ordering code -L)
Sampling method	diffusion
Detection range	0...25% vol.
Resolution	0,01% vol.
Response time T90	<30 s
Signal update	every 1 second
Sensor lifetime	> 2 years for electrochemical sensor > 5 years for optical sensor
Maintenance interval	6 months for electrochemical sensor optical sensor is maintenance free (if no thermal fluctuations occur)
Self-diagnostics	full functionality check at start-up
Warm-up time	≤ 1 min
Power supply	11...30 VDC or 24 VAC
Power consumption	< 2 VA
Digital interface	RS485, Modbus RTU protocol
Analog outputs	2 × 4-20 mA / 0-10 V, user settable
Output scale width	recommended: 20-100% of the range; > 10 × resolution in any case
Enclosure	light grey ABS plastic, wall mount, protection class IP65
Dimensions	H82 × W80 × D55 mm
Remote sensor probe	protection IP65, shielded cable default cable length 3.0 m
Operating environment	industrial indoor and outdoor locations
Operating conditions	15...90% RH non-condensing; 0,9...1,1 atm; explosion safe areas non-aggressive atmosphere -30...+50 °C for electrochemical sensor -30...+60 °C for optical sensor

NOTE We offer technical solutions for extreme humidity, please ask for more information

LCD indicator option

Operating temperature	0...+50 °C
Display dimensions	72 × 36 mm
Number of digits	3.5 7-segment
Character height	14 mm
Other features	backlight

NOTE Only one analog output is available for a version with LCD

Wall mount version

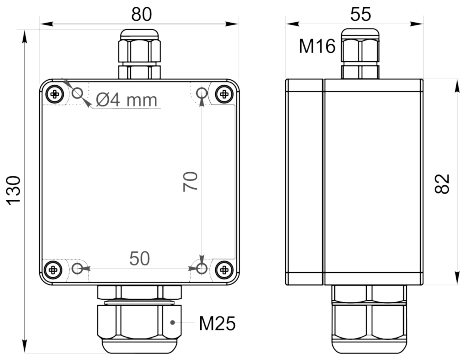

Duct mount version

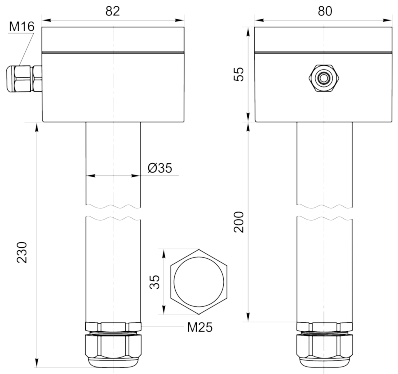

Ask for other versions or custom designed products

Updated 09.03.2020

Connection diagram

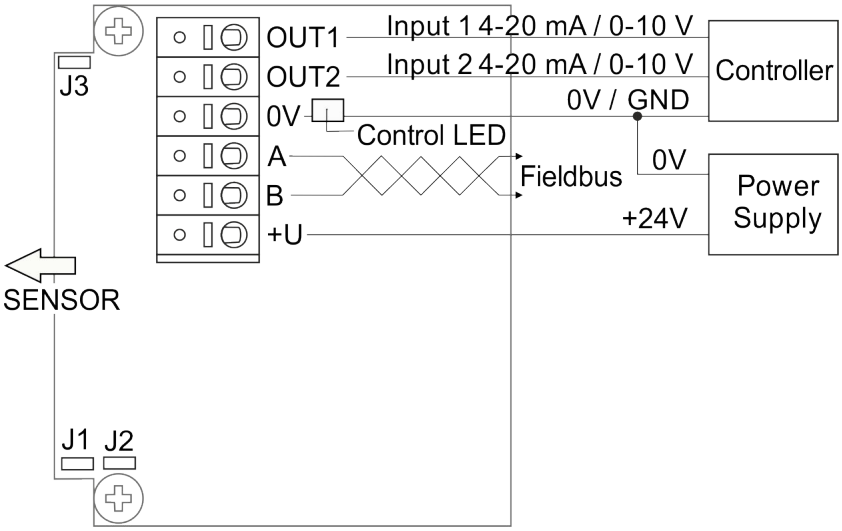

Remote probe

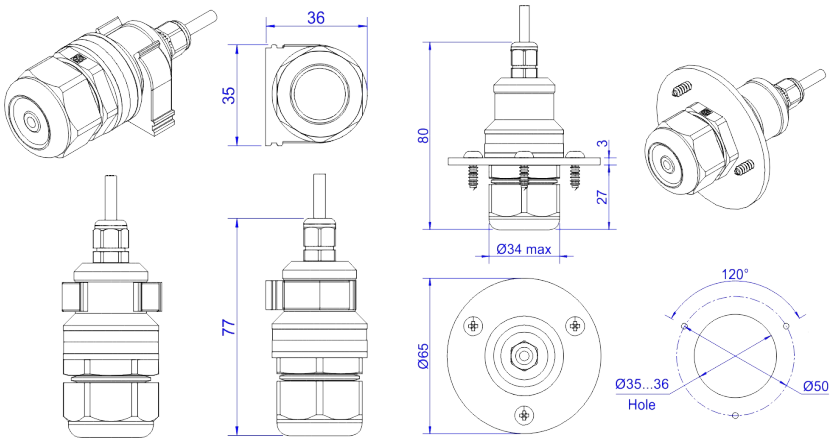

A.4. Umbrella valve technical drawing

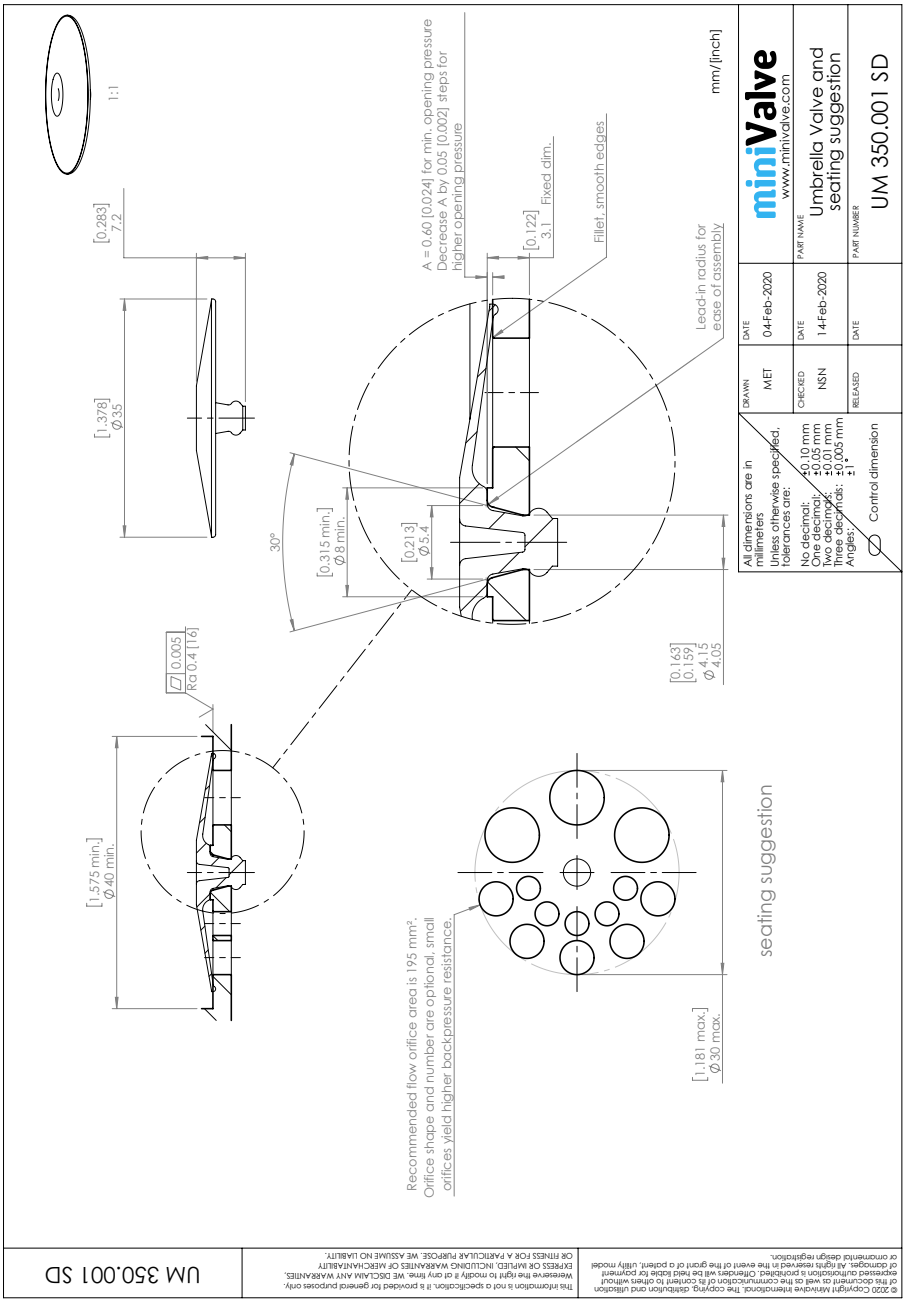

Figure A.1: Umbrella valve technical drawing including valve seat details, by Minivalve International B.V.